DEVELOPMENT OF A ROBUST FRAMEWORK FOR REAL-TIME HYBRID SIMULATION: FROM DYNAMICAL SYSTEM, MOTION CONTROL TO EXPERIMENTAL ERROR VERIFICATION

A Dissertation
Submitted to the Faculty
of
Purdue University
by
Xiuyu Gao

In Partial Fulfillment of the
Requirements for the Degree
of
Doctor of Philosophy

December 2012
Purdue University
West Lafayette, Indiana

To my family!

ACKNOWLEDGEMENTS

I would like first to acknowledge my advisor, Professor Shirley Dyke, for her guidance and support during all this time when I am in the pursuit of my Ph.D. degree. Her enthusiasm and commitment have influenced me beyond the academic research work. I would also like to express my appreciation to the members of my committee, Professor Julio Ramirez, Professor Arun Prakash, Professor Judy Liu and Professor Rudolf Eigenmann, for their time and effort in reviewing this dissertation.

I would like to thank all my fellow graduate students both in the IISL lab and WUSCEEL lab. I’ve benefited greatly from the countless hours we worked and learnt together. Their collaboration, friendship and encouragement have been most valuable to me, without which this work would not be finished.

Finally, I acknowledge the financial support for this research work, which is provided partially by National Science Foundation under grants CNS-1028668, CMMI-1011534 and DUE-0618605.

TABLE OF CONTENTS

LIST OF TABLES

LIST OF FIGURES

Figure Page

ABSTRACT

Gao, Xiuyu. Ph.D., Purdue University, December 2012. Development of a Robust Framework for Real-time Hybrid Simulation: from Dynamical System, Motion Control to Experimental Error Verification. Major Professor: Shirley Dyke.

Real time hybrid simulation (RTHS) has increasingly been recognized as a powerful methodology to evaluate structural components and systems under realistic operating conditions. The idea is to explore and combine the advantages of numerical analysis with physical lab testing. Furthermore, the enforced real-time condition allows testing on rate-dependent components. Although the concept is very attractive, challenges do exist that require an improved understanding of the methodology. One of the most important challenges in RTHS is to achieve synchronized boundary conditions between the computational and physical substructures. Test stability and accuracy are largely governed by the level of synchronization. The sensitivity of the RTHS system error to the de-synchronization error is analyzed, from which a worst-case substructure scheme is identified and verified experimentally. This de-synchronization error, which is largely associated with the actuator dynamics, is further analyzed, by studying the sensitivity of the actuator dynamics with respect to the actuator parameter variation.

The objective of this study is to develop and validate a robust RTHS framework. The framework hardware development include a reaction system, a servo-hydraulic actuation and control system, a digital signal processing system, and a steel moment resisting frame specimen. An H_∞ loop shaping design strategy is proposed to control the motion of actuator(s). Controller performance is evaluated using the worst-case substructure proportioning scheme. Both system analysis and experimental results show that the proposed H_∞ strategy can significantly improve the stability limit and test accuracy. Another key feature of the proposed strategy is its robust performance in terms of both parametric and non-parametric plant uncertainties, which inevitably exist in any physical system. Extensive validation experiments are performed successfully, including the challenges of multiple actuators dynamically coupled through a continuum frame specimen. These features assure the effectiveness of the proposed framework for more complex RTHS implementations.

CHAPTER 1
INTRODUCTION

Historically there are two main methodologies to evaluate structural responses under dynamic loading. Although a shake table test is the most realistic tool, physical and economical limitations restrict its use for the study of structures that are too large, massive or strong. Alternatively, numerical simulation has established its importance because of the improved mathematical modeling techniques, as well as the rapidly growing computational hardware capacity. However, in many cases models are still not available that can accurately reproduce inelastic structural (or advanced energy dissipation devices) behavior. Simulation of structural responses under extreme dynamic loading is to date a challenging topic that may need to be verified experimentally.

Pseudo-dynamic (PsD) testing technique, also referred as hybrid testing, is an innovative way of analyzing an integrated large-scale structural system. Pseudo-dynamic testing is unique in the sense that it combines the experimental and numerical analysis to explore the benefits of both methodologies. The basic idea is to represent part of the substructure computationally using a well-established mathematical model, while physically testing rest of the other substructures that may have complicated mechanical characteristics.

During each time step of a displacement controlled test procedure, the responses of the numerical substructure, under the input dynamic loading, are calculated by solving the associated equations-of-motion (EOM). Obtained displacements at the interface nodes are then imposed on the physical substructure using actuators at discrete spatial locations. The physical forces acting on the loading interfaces are sequentially measured and fed back to the numerical substructure, to calculate the time evolution of next step displacement responses.

Conventional hybrid testing normally leads to an expanded time scale as compared to the actual duration of the dynamic input record. Therefore real-time hybrid simulation (RTHS), which enables experiment to be performed in a common time scale, is necessary to test specimen with rate dependent characteristics. The potential advantages of RTHS methodology are: 1) it is a cost effective approach to analyze the entire structure as an integrated system that balances the demands for the lab space and loading capacity; 2) physical testing of critical components can circumvent convergence and stability issues that commonly arise in a numerical simulation, especially when highly nonlinear elements need to be analyzed; 3) the enforced hard real-time test condition captures the rate-dependent dynamics of various structural systems, so that effective structural analysis and structural vibration mitigation strategies can be evaluated in a most realistic condition; 4) RTHS allows sub-structuring testing of a large scale structural system, which can avoid the geometric and kinematic similitude issues for scaled models.

1.1 Scopes and Objectives

One of the major challenges in conducing hybrid testing is to synchronize the boundary conditions between the numerical and experimental substructure interfaces. The stability and accuracy of a hybrid testing depend largely on the quality of the actuator motion control strategy, i.e. the level of accuracy to apply physical boundary conditions. A slow rate hybrid testing poses much less challenge in this aspect because it requires only the steady state target variables (displacements and/or forces etc.) to be applied on the test specimen. Transient behaviors can therefore be neglected and the actuators are slowly ramped and held at the final target positions constantly for most of the time, until the numerical evolution of the next step responses are available. In a RTHS, however, the necessity to impose accurate dynamic loads and displacements are difficult, especially when large deformation and/or high forces are needed over a wide frequency range. The discrepancies between the desired and measured states can simply be approximated as a time domain shift in a conventional testing, when the structure is tested in an open-loop manner. However, the closed-loop RTHS system is implemented through various feedback paths that demand multiple channels of instantaneous physical measurements. A slight de-synchronization error (the stability limit may be less than 1ms as shown in Chapter 7) can therefore enable significantly enlarged test error, or very possible the test instability. To characterize such complex nonlinear dynamics is challenging since it is not only a function of the input signal amplitude and frequency, but also depends on the properly of experimental subsystem itself e.g. the type and dynamic behavior of the test specimen and the loading actuator. Moreover the physical coupling and interactions are complicated between multiple actuators for the proposed multi-axis test platform, which require a good understanding of the composing electro-mechanical (electro-hydraulical) actuation and control system, along with the structural and/or damper specimen. Therefore the development of advanced actuator modeling techniques and robust motion control algorithms become a vital component of a high fidelity RTHS framework.

The focus of this dissertation is to develop and validate a robust framework that is suitable for generalized RTHS testing purposes. The framework is designed to accommodate multiple actuators that are dynamically coupled and strongly interacted through the test specimen. A loop shaping algorithm based on the advanced H_∞ control theory is proposed for the actuator motion control. The control strategy is validated extensively to demonstrate its effectiveness to achieve significantly improved test stability and accuracy. The very basic idea that makes RTHS attractive is its potential ability to test physical substructures with unknown properties, otherwise it should simply be replaced with numerical models to avoid challenges posed by physical testing. The proposed H_∞ controller is very robust to plant uncertainty, which stands clear advantage to make the framework a plug-and-play system. The controller requires minimal plant (including both test specimen and actuators) information, and is robust to accommodate system nonlinearities and uncertainties that can arise in the middle of an online testing.

It is demonstrated in this study that the RTHS error depends heavily on the experimental plan, i.e. the decomposition of numerical and experimental substructures. A worst-case substructure scheme is identified and used to design the tests in the experimental sections. A systematic approach is used in this dissertation to view each component from a control system perspective, so that the overall RTHS system dynamical properties can be evaluated accordingly. A modeling technique is also proposed in this dissertation to simulate uncertainties that can occur in any dynamical system component, which can facilitate to perform offline analysis and prototyping of a RTHS system. The advantages of an offline sensitivity study not only benefit to leverage the experimental cost and risk management, but also to characterize the system properties and maximize the controller performance.

1.2 Literature Review

Real-time hybrid simulation is an innovative technology to analyze structural responses in a common time scale, which essentially allows testing of systems with rate dependent components. High force, low friction servo-hydraulic actuators are commonly used to load test structures, in which a servo control mechanism is applied for displacement and/or force motion control. The proprietary actuator and control system normally introduces a frequency dependent phase lag, in addition to the computational and communication delays posed by the computer and data acquisition systems. The mechanical system phase lag is nonlinear in nature that is challenging to characterize accurately, compared to the electronic system induced delay that is relatively small and constant (Carrion & Spencer, 2007). Both the phase lag and the time delay cause de-synchronization error between the numerical and the experimental substructure states. The effect of this de-synchronization error is devastating in that it may even cause the RTHS experiment to go unstable, so that it should be carefully studied and properly compensated when planning a hybrid experiment.

The inevitable influence of the de-synchronization error was initially interpreted as a response delay in (Horiuchi, Inoue, Konno, & Namita, 1999). This response delay had been demonstrated to cause the increase of the total system energy, which was interpreted as an equivalent of adding negative damping into the hybrid system. If the negative damping exceeds the inherent structural damping, the response goes unstable. A compensation method was thus proposed in the same paper to predict the displacement after the assumed time delay δ_t. An n^{th} order polynomial function is proposed to extrapolate the predicted value, based on the current and n previous displacement values.

$$x_c = \sum_{i=0}^{n} a_i x_{d,i} \qquad (1.1)$$

The predicted displacement x_c was thus inputted as the control signal to the actuator and the resulting measured displacement x_m is expected to synchronize better with the desired displacement. Here $x_{d,0}$ is the numerical substructure displacement at the current integration time step and $x_{d,i}$ is at $\delta_t \times i$ steps ago. Depends on the selected order of polynomial n, the non-dimensional variable $\omega\delta_t$ cannot exceed certain upper bound value to guarantee stability, where ω is the highest natural frequency of the total structure. Such limitations made this technique hard to be applied for experiments where either the actuator has a large delay δ_t, or a multiple-degrees-of-freedom (MDOF) structure that has a large ω. An important yet less accurate assumption made in this compensation technique is that the actuator is a pure time delay device that neglects the amplitude distortion. Another assumption is that δ_t is constant i.e. independent of the system properties and input characteristics.

(Horiuchi & Konno, 2001) later proposed a new compensation scheme for actuator control. The new compensated control signal was generated by using not only the displacement but also the velocity $\dot{x}_{d,0}$ and the acceleration $\ddot{x}_{d,0}$.

$$x_c = x_{d,0} + \delta_t \dot{x}_{d,0} + \frac{1}{3}\delta_t^2 \ddot{x}_{d,0} + \frac{1}{6}\delta_t^2 \ddot{x}_c \qquad (1.2)$$

The predicted acceleration herein was assumed to vary linearly according to $\ddot{x}_c = 2\ddot{x}_{d,0} - \ddot{x}_{d,1}$, the displacement can therefore be calculated by numerical integration. The acceleration, velocity and displacement values at the current step are all required in equation (1.2) to conduct the extrapolation. However, most of the explicit time integration methods do not provide all these information. The reference time was thus selected at one previous time-step before the current step to perform the prediction. The prediction period then became $\Delta_t+\delta_t$ instead of the normally assumed δ_t, where Δ_t is the integration time step. It was demonstrated theoretically this new compensation scheme can improve the stability limit compared with the original polynomial prediction formulation in equation (1.1).

Noticed the importance for accurately compensation of actuator delay, (Darby, Williams, & Blakeborough, 2002) proposed a method to online estimate the time delay during testing. An intrinsic improvement on this assumption is that the delay is assumed more realistically to be time variant. It was observed that both overestimating or underestimating the delay can cause instabilities, and the delay error tolerance was different for each individual actuator, even within the same experiment. Experimental results showed trend of increased delay as the stiffness of the test specimen increased. The error in the delay estimate was then proposed as

$$\Delta\delta = \delta_t - \delta_{t,1} = C_p \tanh\left(C_v \frac{\left(x_{d,0} - x_{d,1}\right)}{\Delta t} \right)\left(x_{d,1} - x_{m,1}\right) \tag{1.3}$$

Here $\Delta\delta$ was assumed to be proportional to the relative position error between desired and measured displacements. Experimental observation revealed that the actuator could not normally achieve the desired amplitude at the peak displacement (zero velocity), which was attributed as the intrinsic actuator physical behavior. Therefore a relatively large estimation error appeared even when desired and measured displacements were completely in phase. The hyperbolic tangent term of the actuator velocity was thus assumed in equation (1.3) to produce less compensation near zero velocity regions. The proposed delay estimation scheme can be combined with most of the prediction and compensation strategies to generate the actuator control signal. Twin actuator tests indicated improved stability using the proposed delay estimation algorithm, compared to the fixed delay compensation scheme.

Another delay estimation formulation was proposed in (Ahmadizadeh, Mosqueda, & Reinhorn, 2008), based on a similar philosophy. The delay estimate between the desired and measured displacement signals was calculated as

$$\delta_t = \delta_{t,1} + 2G\Delta t \frac{\overline{x}_d - \overline{x}_m}{x_{m,0} - x_{m,2}} \tag{1.4}$$

where $\overline{x}_d$ and $\overline{x}_m$ are the average of last three data points for each corresponding signal. The proposed formulation claimed to be more effective to estimate the delay, which converged faster and produced less oscillation compared to equation (1.3). Given the estimated delay for each step, the control signal was calculated using a prediction formulation that assumed constant acceleration variation.

$$x_c = x_{d,0} + \delta_t \dot{x}_{d,0} + \frac{1}{2}\delta_t^{\,2} \ddot{x}_{d,0} \tag{1.5}$$

The proposed formulation claimed to reduce the high frequency noise in the force measurements compared to the polynomial extrapolation in equation (1.1).

(Jung & Shing, 2006) proposed a discrete feed-forward compensation scheme. The method was based on the assumption that the displacement control errors within a time step was more or less the same as those in the previous step. Once the updated displacement was available through integration of the numerical substructure, the control signal in the current time step was predicted as

$$x_c = x_{d,0} + k_{DFC}\left(x_{c,1} - x_{m,1}\right) \tag{1.6}$$

where k_{DFC} is a gain factor, $x_{c,1}$ and $x_{m,1}$ are the control signal and measured displacement at the previous step.

(Chen, 2007) proposed a simple delay model by idealizing the actuator displacement response to be linear, with the assumption that the servo-controller was normally operated at a small time interval. The inverse of this simplified model was thus used for actuator delay compensation, which can be interpreted as time domain extrapolation of the desired displacements from two immediate preceding time steps. The transfer function of the inverse control strategy was expressed in the discrete-time domain as

$$G_{inv}(z) = \frac{X_c(z)}{X_d(z)} = \frac{\alpha_{inv} \cdot z - (\alpha_{inv} - 1)}{z} \tag{1.7}$$

where α_{inv} is the delay constant that is defined as the ratio between the actuator delay and the controller execution time step. A tracking error based adaptive inverse compensation strategy (Chen & Ricles, 2010) was further developed where the control law was modified to include an adaptive parameter $\Delta\alpha$.

$$G_{inv}(z) = \frac{X_c(z)}{X_d(z)} = \frac{\left(\alpha_{inv} + \Delta\alpha\right) \cdot z - (\alpha_{inv} + \Delta\alpha - 1)}{z} \tag{1.8}$$

The parameter $\Delta\alpha$ was calculated based on the enclosed area of the hysteresis in the synchronized subspace of x_c and x_m. This adaptive algorithm was demonstrated through experiment to be robust in accommodating initial estimation inaccuracy and time variant nature of the actuator delay. The adaptive scheme claimed stand clear advantage over the basic inverse compensation scheme.

The above mentioned time delay extrapolation (prediction) and interpolation methods constitute a major category of the actuator control strategy. The concept of time delay model has been widely accepted in the RTHS community. The compensation methods are generally straightforward to understand that can be implemented using only several of the most recent command and/or measured data points. However, the physical principals of the complicated actuator system are not considered in these methods. Instead the simplified empirical representations are assumed. It is therefore necessary to understand the assumption and limitation of each method, before conduct an experiment.

(Zhao, 2003) performed a comprehensive study of servo-hydraulic systems in the implementation of both effective force testing (EFT) and real time pseudo-dynamic testing (RPsD). The natural velocity feedback (Dyke, Spencer, Quast, & Sain, 1995) compensation was experimentally demonstrated to be essential for actuators to apply forces, especially near the structural natural frequencies. Because velocity feedback compensation incorporated the inverse of the servo-system dynamics, accurate knowledge of system nonlinearities was shown to be critical for EFT test. Since a delay in the time domain can be loosely interpreted as a phase lag in the frequency domain, a phase lead compensation scheme was proposed to minimize the response delay where the delay constant was identified experimentally. In case of a RpsD test, a first order phase lead compensator was used for both the amplitude adjustment and the phase lag reduction.

A model based feed-forward compensation scheme (Carrion & Spencer, 2007) was proposed based upon a higher order servo-hydraulic control system model. Without loss of generality, the transfer function between the command displacement x_c and the feedback measurement x_m can be expressed as a linear system

$$G(s) = \frac{X_m(s)}{X_c(s)} = \frac{K}{\prod_{i=1}^{np}(s - p_{,i})} \tag{1.9}$$

where *np* is the number of system poles and $p_{,i}$ are the individual pole locations on the complex plane. Since the direct inverse of *G(s)* is non-causal, a unity-gain low-pass filter was added in series to form a compensator with the expression

$$G_{mb}(s)=\frac{X_c(s)}{X_d(s)}=\alpha_{mb}^{np}\frac{\prod_{i=1}^{np}(s-p_{,i})}{\prod_{i=1}^{np}(s-\alpha_{mb}\cdot p_{,i})} \tag{1.10}$$

where the control parameter $\alpha_{mb}>1$ needed to be tuned experimentally to reach an optimal value for each specific experimental setup. A large α_{mb} normally represents better performance with a tradeoff that it also magnifies the modeling error. For a successful digital implementation, α_{mb} needs to be kept reasonably small to avoid the frequency warping introduced by the controller digitalization procedure, limited by the upper bound of chosen sampling frequency.

A model reference adaptive control (MRAC) strategy (Landau, 1979) is one of the main approaches to construct adaptive controllers. Generally, a MRAC controller is composed of four parts: a plant that contains unknown parameters; a reference model that specifies the desired performance of the control system; a feedback control law that contains adjustable control parameters; and an adaptive law to update the control parameters. The minimal control synthesis (MCS) family (Stoten & Benchoubane, 1993) of outer-loop control strategy was one of the MRAC formulations, and had been a subject of a large group of research work. The plant was approximated by a first-order transfer function system. The controller signal was constructed based on both the command and the measured displacements.

$$x_c(t)=K_m(t)x_m(t)+K_d(t)x_d(t) \tag{1.11}$$

where K_m and K_d are adaptive gains determined from the following adaptive laws

$$\begin{aligned} K_m(t) &= \alpha \int_0^t C_e x_e(\tau) x_m(\tau) d\tau + \beta C_e x_e(t) x_m(t) + K_m(0) \\ K_d(t) &= \alpha \int_0^t C_e x_e(\tau) x_d(\tau) d\tau + \beta C_e x_e(t) x_d(t) + K_d(0) \end{aligned} \quad (1.12)$$

Here x_e is the difference between the reference model output and plant output, C_e is an error gain constant, $K_m(0)$ and $K_d(0)$ are initial adaptive gains, and α and β are adaptive weights. Recent development based on the MCS family controller was called the minimal control synthesis algorithm with modified demand controller in (Lim, Neild, Stoten, Drury, & Taylor, 2007). Two modifications were proposed to make the controller more suitable for RTHS applications: a modified controller demand that integrated the numerical substructure dynamics with the reference model; and a force feedback link from the plant to the numerical substructure. Local high frequency resonances occurred without a proper selection of initial adaptive gains, which were Erzberger values that need to be identified for each specific experimental setup. The proposed controller was demonstrated to be able to cope when system mis-modeling was present, compared to the results obtained in a linear controller test.

(Phillips & Spencer, 2011) proposed a new model-based actuator compensation scheme. To cope with the inverse of a non-causal dynamical system, the low-pass filter design in equation (1.10) was modified to be calculated from the time domain derivatives. Some lower order time derivative quantities e.g. displacement, velocity and acceleration were obtained directly from the numerical substructure integration step, while higher order derivatives can be evaluated separately e.g. the jerk can be calculated as the slope of acceleration etc. Excessive noise introduced by this numerical differentiation procedure was considered acceptable, because these signals contributed less on the control input signal synthesis. When higher order derivatives are not available, low-pass filtering techniques can be added to reduce the degree to which the inverse is improper. However these filters normally introduce unwanted dynamics into the closed-loop system.

Other actuator control strategies proposed in the RTHS community range widely from the classical control design methods e.g. (Reinhorn, Sivaselvan, Liang, & Shao, 2004), to the modern control design e.g. model predictive control design in (Li, Stoten, & Tu, 2010).

Various experiments and RTHS frameworks have also been developed to explore the potential benefits of the innovative methodology. For instance, a continuous pseudo-dynamic testing hardware (Magonette, 2001) was developed in the European Laboratory for Structural Assessment (ELSA). This system consisted of one master and multiple slave cards interconnected by ISA passive bus. The master card was equipped with a Pentium processor with large memory which executes the kernel of pseudo-dynamic algorithms. Each slave card consisted of one PC104 CPU card, one controller I/O card and one analog I/O card. Software developed for this system allowed the foreground process to be executed with absolute priority at fixed sample rate, triggered by an interrupt generated by specific board. Other background processes ran with lower priority those asynchronous data exchange tasks as well as user interface interacting.

A RTHT platform was developed at Harbin Institute of Technology (Wang, 2007) that utilized the programmable feature of MTS FlexTest GT digital servo-controller to perform onboard computation. Numerical algorithms were developed on a host PC equipped with MTS 793.10 software using its own programming language, and executable codes were downloaded and executed on FlexTest system. To ensure real time property, a square wave signal with specific period was generated onto the FlexTest system which managed the initial interrupt as well as time triggering of the code execution.

Other development efforts [(Nakashima & Masaoka, 1999), (Blakeborough, Williams, Darby, & Williams, 2001), (Bonnet, 2006), (Carrion & Spencer, 2007)] utilized dedicated digital signal processor (DSP) boards to solve the EOM and form the outer-loop real-time control system. The DSP board has access to external A/D and D/A channels, normally equipped with compatible I/O terminal boards, which can send command signals to the servo-controller and measure feedback signals from the test specimen.

Several facilities were made available under the support of George E. Brown, Jr. Network of Earthquake Engineering Simulation (www.nees.org). The University of California at Berkeley and the University of Illinois each individually developed middleware frameworks, OpenFresco (Takahashi & Fenves, 2006) and UI-SIMCOR (Kwon, Elnashai, Spencer, & Park, 2007), respectively. These developments were mainly intended to facilitate pseudo-dynamic or multi-site geographically distributed hybrid testing applications, with a potential to be expanded to real-time applications in the future. The real-time multi-directional earthquake simulation facility in Lehigh University [(Chen, 2007), (Mercan, 2007)] was integrated with xPC target, digital servo-controller and DAQ system through SCRAMNet. SCRAMNet is a fiber optic communication device that enables shared memory and time synchronization of all components that are within the network. Data synchronization can be achieved within microseconds. Complex algorithms can be developed on a host PC and downloaded onto target PC using Mathworks SIMULINK and xPC Target software. SCRAMNet was also adopted at the University of Colorado (Wei, 2005) as part of the fast hybrid testing facility. One approach that implemented the computational part was a heavily customized version of OpenSees running on Phar-Lap ETS (a real-time OS which provides a subset of Win32 APIs to minimize the effort for porting desktop application to embedded systems). Development effort was also made towards a separate real-time finite element tool.

1.3 Overview

The organization of this dissertation is about the development and experimental validation of a new RTHS framework. Chapter 2 presents the multi-axis RTHS hardware developed at the IISL lab in Purdue University. A reinforced concrete reaction is designed and constructed to support the testing facility. A highly reconfigurable steel moment resisting frame (MRF) structure is designed and erected to perform validation experiments. A six channel inner-loop analog servo-hydraulic control system is assembled to drive the motion of actuators. A high performance outer-loop DSP system is configured to implement and execute the key digital components, including structural analysis and control algorithms.

Chapter 3 reveals the importance of a RTHS experimental plan and its implications to the test stability and accuracy. The sensitivity of a RTHS system is evaluated to the substructure de-synchronization error, using a SDOF test design. A worst case substructure scheme is identified and used to design the later validation experiments.

Chapter 4 proposes a generalized methodology to model dynamical system uncertainties. A linear servo-hydraulic actuator model is appended with this uncertainty model to evaluate the system frequency, or step, responses, as well as the system sensitivity to both parametric and non-parametric variations.

Chapter 5 presents the theory and implementation of a generalized model reference adaptive control (MRAC) algorithm. The plant model is not limited to a first-order transfer function system. The effectiveness of the MRAC in the actuator control application is examined experimentally.

Chapter 6 proposes an H_∞ loop shaping control algorithm. Both the controller tracking accuracy and its robustness properties are evaluated through simulation and experiments. Comparisons are also made with several existing algorithms to demonstrate the proposed controller's performance.

Chapter 7-9 presents three validation experiments with gradually increased complexity. The proposed H_∞ controller is considered within the overall RTHS context to evaluate its performance. Chapter 7 tests a single floor MRF specimen and Chapter 8 a more generalized multiple-floor configuration. Both the frequency domain system error and the time domain experimental error are assessed, to understand implications of the actuator tracking error to the RTHS stability and accuracy. Superior performances are observed on the proposed H_∞ controller, even with the existence of strong dynamic coupling between multiple actuators.

Chapter 9 presents the RTHS results of the MRF specimen when it is equipped with a rate dependent magneto-rheological (MR) damper device. Three phase comparisons are made, with more physical components assumed in each latter phase. All test results compare well and demonstrate again the excellent performance of the proposed framework. It is also seen that the MR damper is very effective to mitigate structural vibrations.

Finally, Chapter 10 summarizes the important research findings throughout this dissertation. Observed issues are also discussed that can lead to future research.

CHAPTER 2
RTHS FRAMEWORK HARDWARE DEVELOPMENT

The Intelligent Infrastructure Systems Lab (IISL) at Purdue University houses a novel Cyberphysical Instrument for Real-time Structural hybrid Testing (CIRST). The instrument consists of the following major components:

1) Reaction Mounting System (RMS). This system is designed to support the physical components of the simulation in a suitably stiff arrangement to perform the variety of tests needed.
2) Steel Moment Resisting Frame (MRF). This highly reconfigurable specimen is designed and fabricated to experimentally validate the developed framework.
3) Real-time Control System (RCS). This component coordinates all physical and computational actions and meets the timing constraints of a real-time hybrid test. The design strives for interoperability to facilitate implementation of any number of configurations.
4) Sensing and Actuation System (SAS). This component is used to measure physical responses and apply forces and/or displacements during the tests.

5) RT-Frame2D. This open source structural analysis tool is developed to simulate the complex, nonlinear behaviors of the numerical component of the hybrid simulation in real-time.

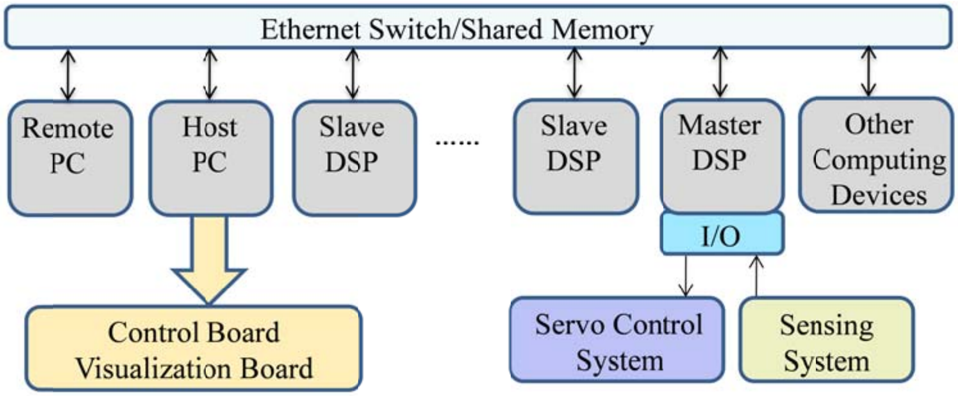

Figure 2.1 RTHS Framework System Architecture

A vision of the framework system architecture is schematically shown in Figure 2.1. The master digital signal processor (DSP) executes major real-time objects (e.g. computational substructure and control algorithms) and subsequently communicates with the analog sensing and servo-control system through the I/O modulus. Applications are developed on the host PC under the MATLAB/SIMULINK environment. Target code is then generated using the real-time workshop and downloaded from the host onto the target DSP that executed directly atop the target machine hardware. Data on target machine can also be sent back to the host PC as a background process (not necessarily in hard real-time), which facilitate the run time user interaction and data visualization capabilities. Currently the host and target system communication are performed through Ethernet connection approach that can potentially be expanded to shared memory technology for more bandwidth and efficiency. Slave DSPs are also planned to be integrated into the framework to share the computational load, when the numerical substructure becomes more complicated. However, the efficiency of this type of distributed real-time computing has to be carefully planned to overcome the additional communication latency. Furthermore, remote access to the host PC (e.g. through data turbine) can be considered so that tele-operation and tele-participation of experiments through Internet are enabled. Safety procedures need to be established beforehand to circumvent the system instability before remote operation is allowed.

The developed framework components and data flow are shown in Figure 2.3. The analog servo hydraulic control system can be configured to use either a displacement or a force feedback control mode, to apply the motion boundary conditions on the physical specimen. The pressure to power the actuator on each hydraulic service manifold channel can be turned on/off (individually) by a proprietary servo-hydraulic analog control system. The actuator servo-valve command is generated through the analog controller too. The target DSP system executes user programmed digital components that communicates with the analog system to enable more advanced dynamic testing. The proposed RTHS control system block diagram is schematically shown in Figure 2.2, which is composed of a control formulation of three hierarchical feedback closed-loops. The physical substructure displacement boundary conditions are applied through the analog controller (PID control for most of the proprietary systems), which is referred as the inner-loop. A digital controller is implemented to further enhance the displacement synchronization between the computational (x_d) and physical substructures (x_m), which forms the outer-loop. The measured physical substructure forces (f_m) are fed back into the computational substructure to evolve the equation of motion to the next integration step, which forms the RTHS system. The purpose of this study is to use the proposed RTHS system to reproduce the reference structure, which is a passive inherent stable system. The dynamics of each component and their interactions through multiple feedback paths need to be analyzed and validated thoroughly, before the framework can be trusted to evaluate unknown structures. Individual components are discussed in the following chapters and the performance of the overall RTHS system is compared with the reference structural system both analytically and experimentally. A snap-shot of the final developed hardware components are shown in Figure 2.4.

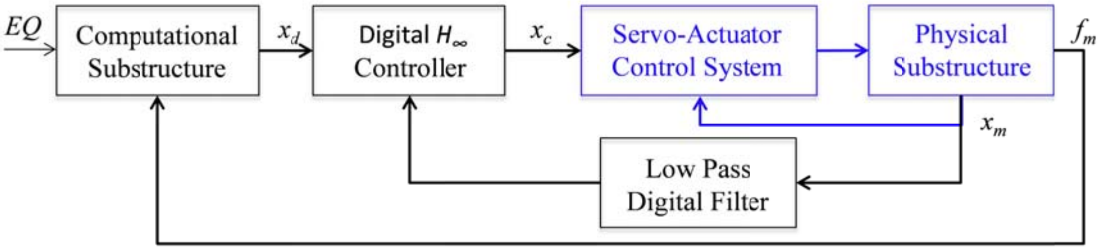

Figure 2.2 Framework Control System Diagram

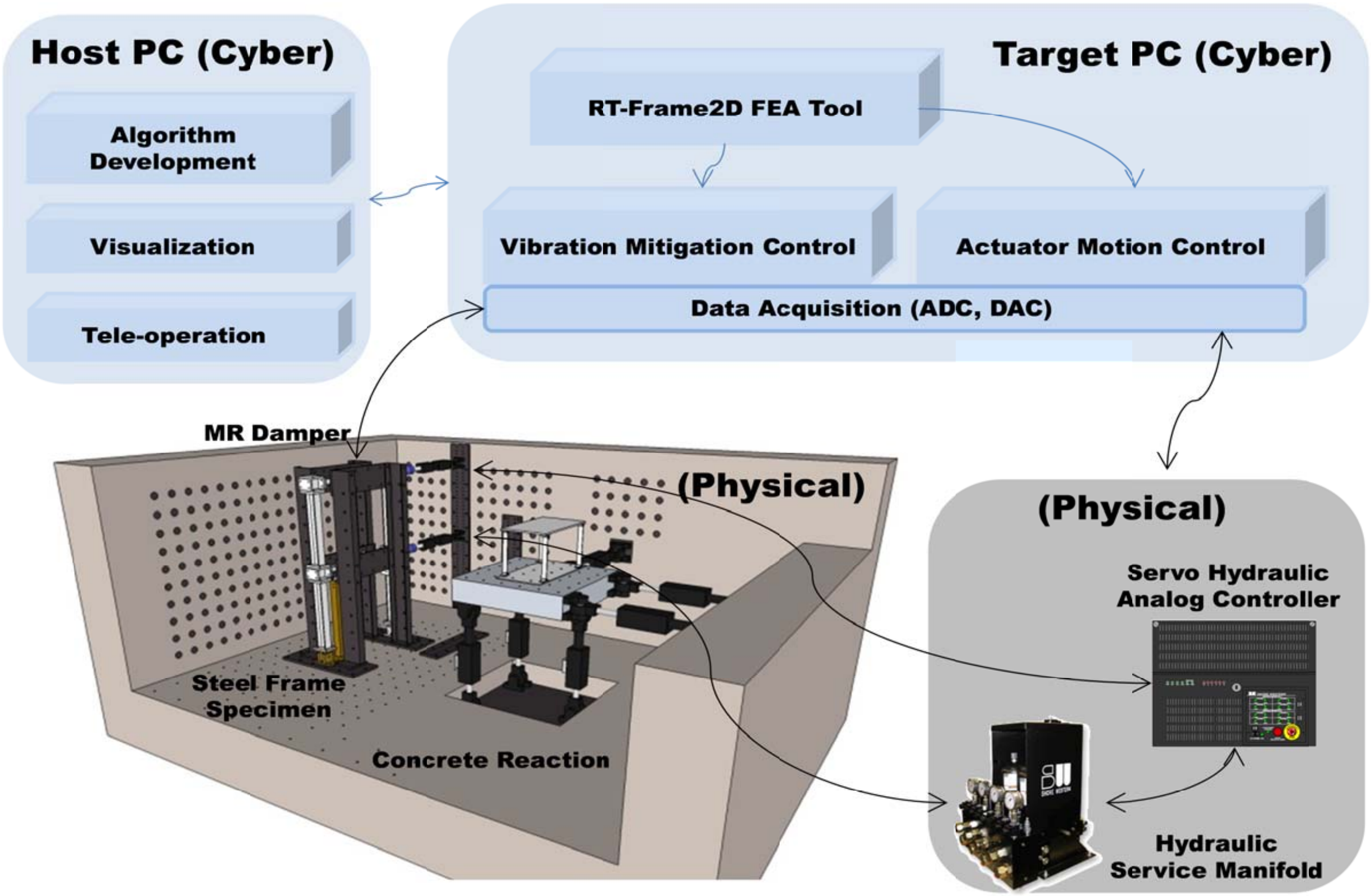

Figure 2.3 Framework Components and Data Flow

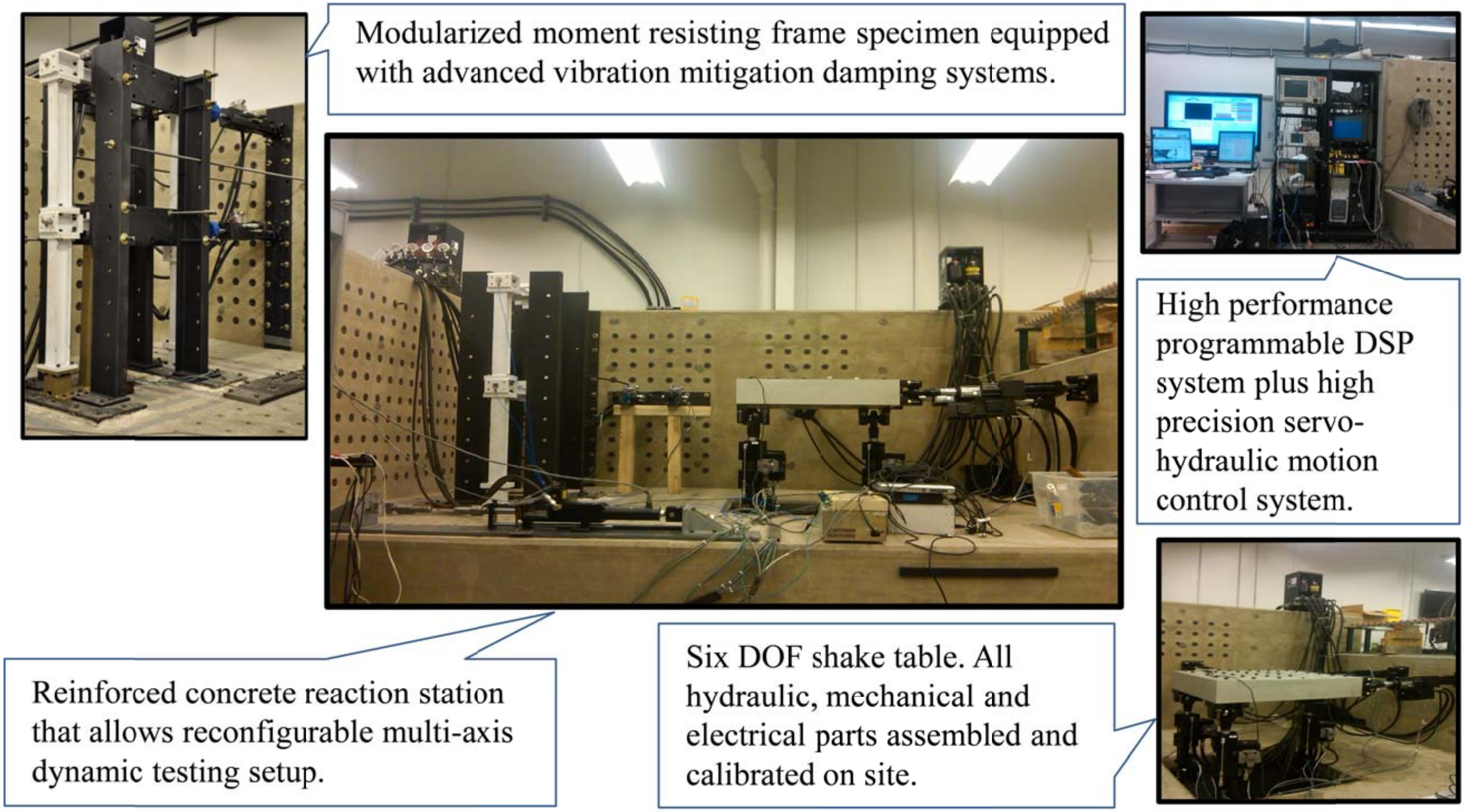

Modularized moment resisting frame specimen equipped with advanced vibration mitigation damping systems.

High performance programmable DSP system plus high precision servo-hydraulic motion control system.

Reinforced concrete reaction station that allows reconfigurable multi-axis dynamic testing setup.

Six DOF shake table. All hydraulic, mechanical and electrical parts assembled and calibrated on site.

Figure 2.4 Framework Hardware Development

2.1 Reaction Mounting System

This reaction supports the physical components of the simulation in a suitably stiff arrangement to perform the variety of tests needed. A reinforced concrete reaction wall is designed and constructed that has a strong floor measures 14’x10.5’ (4.27m x 3.2m). The thickness of the floor slab is 18” (46.7cm). The strong wall measuring 5’x16” (1.52m x 40.6cm) surround both a longitudinal and a lateral side, a third shorter wall of 3’x16” (0.91m x 40.6cm) covers the opposite lateral side. Inserts and steel sleeves on a 5”x5” (12.7cm x 12.7cm) grid are embedded into the testing area floor and walls. Additional steel interface plates are fabricated that are tap threaded at a minimum spacing of 1.25” (3.2cm) apart, to accommodate the hydraulic actuator swivel mounting pattern. These features enable multiple actuators to be flexibly placed in a three dimensional spatial configuration, therefore make the reaction system an ideal re-configurable testbed for most types of structural testing. The design and layout of the reaction is shown in Figure 2.5 and the reinforcement design in Figure 2.6. A customized six DOF shake table is placed on the right side of the reaction. Three vertical actuators are configured, another two in the longitudinal and one in the lateral direction.

The design of the reaction wall considers both the bending and the shear effects of two actuators acting in parallel at the top of the reaction wall. A wall strip is assumed as a cantilever from the bottom with a concentrated point force of F=4.6 kip (20.47 kN) applied at the top with a maximum cantilever length of L=51” (1.3m). A unit width of the wall b=12” (30.5cm) with a half thickness d=16/2=8” (20.32cm) is assumed to support this load. This design is conservative since the reinforcing effects of the surrounding members are neglected. The design concrete compressive strength is f_c'=4 ksi (27.58 MPa) and the steel rebar yield strength is f_y=60 ksi (413.7 MPa). The maximum applied bending moment at the cantilever end section is thus $M_u=F \times L$=234.6 kip-in (less bending is caused by the six DOF shake table actuators that is 6.8 x 32=217.6 kip-in < M_u). The concrete modulus of elasticity is designed to be E_c=57,000 x $(f_c')^{1/2}$=3605 ksi. The section moment of inertia is $I=12 \times 16^3/12$=4096 in^4.

Table 2.1 The 28-Day Concrete Strength Tests (psi)

	Floor (mix 1)	Floor (mix 2)	Wall
Test 1	9483	9881	8448
Test 2	9222	9872	8220
Test 3	9520	9566	8924

The 28-day cylinder test data in Table 2.1 indicate that the compressive strength of the used self-consolidating concrete mix averages about 9,500 psi for the floor and 8,500 psi for the wall, well above the designed value (4,000 psi) which makes the reaction system a conservative design. The required flexural reinforcement ratio ρ (Hassoun & Al-Manaseer, 2005) is determined as

$$\rho = \frac{f_c^{'}}{fy}\left[0.85 - \sqrt{0.85^2 - Q}\right] = 0.0053 \tag{2.1}$$

where

$$Q = \frac{1.7}{f_c^{'}}\frac{M_u}{bd^2} = 0.13 \tag{2.2}$$

The required reinforcement is $A_s = \rho bd = 0.513\ in^2$ and the design includes #5 rebar with yield strength of 60ksi placed at a 6” spacing that provides $A = 0.62\ in^2 > A_s$. The reaction design is therefore adequate to resist the bending moment induced by this maximum loading combination of 2 x 2.3 kip actuators, acting side by side at the very top of the reaction wall height. The shear capacity of the reaction provided by the concrete is $V_c = 2\sqrt{f_c^{'}}bd = 12.14$ kip that is larger than the total applied actuator forces. The design includes #4 shear rebars at a 7.5” spacing for the wall and a 6” spacing for the floor in a bidirectional configuration, both controlled by the minimum shear reinforcement requirement. The maximum deflection of the reaction was designed to be less than 0.01” under the maximum actuator loading conditions. The self-weight of the reaction system is more than 30 tons. Inserts and sleeves on a 5” grid are embedded into the floor and walls, in combination with additional steel interface plates that enables multiple actuators to be flexibly placed in a three dimensional configuration at a minimum spacing of 1.25” apart. These features essentially make the reaction system an ideal re-configurable testbed for most types of structural testing.

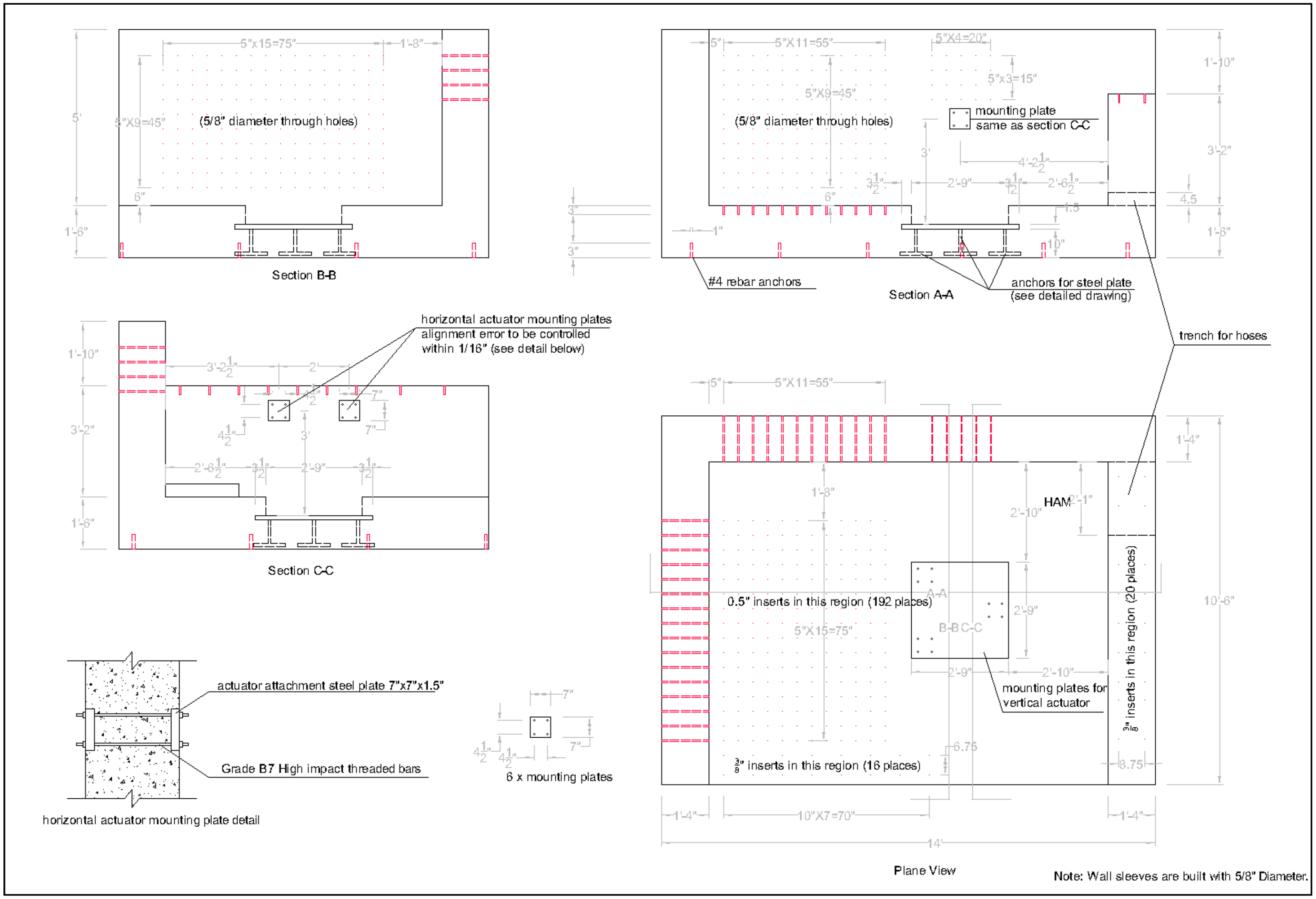

Figure 2.5 Reaction Design and Layout

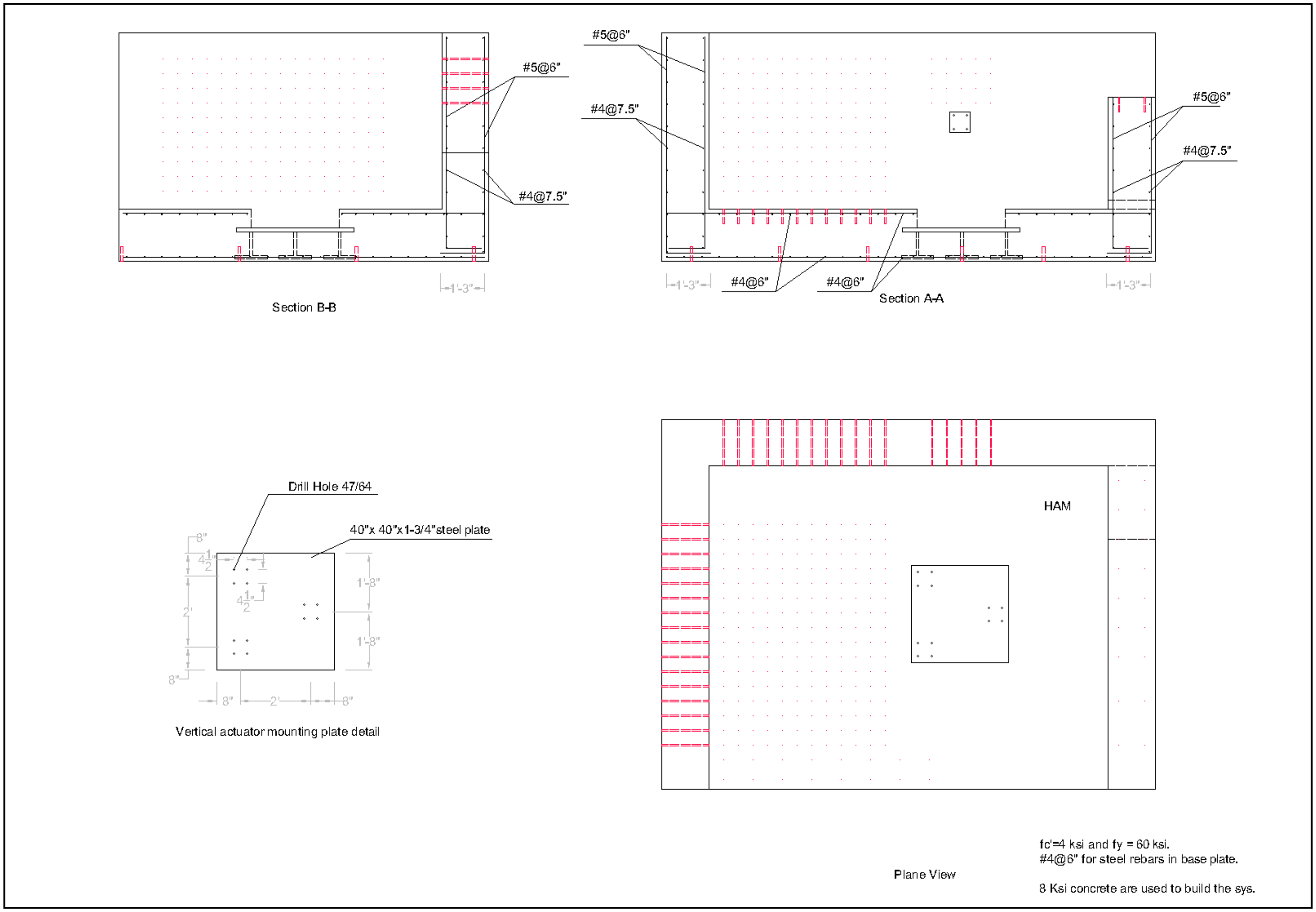

Figure 2.6 Reaction Reinforcement Design

2.2 Steel Moment Resisting Frame Specimen

A steel MRF specimen is designed and erected in the IISL lab. The specimen was designed to perform acceptance testing and will be available for future testing needs. The specimen is modular, consisting of sets of horizontal beams, vertical columns and joint block panel zone elements. Each member is replaceable and can be easily re-assembled if any structural damage or plasticity occurs. Base supports are designed as pin-connections to reduce the moment gradient and avoid the formation of plastic hinges at column bases during experimentation. Multiple sets of specimen components are fabricated that can be later expanded into a three dimensional test configuration, if necessary. All parts are connected through the use of anti-lock high-strength steel bolts to avoid the formation of flexibility at connection interfaces, after repetitive dynamic testing. Steel S flange S3x5.7 commercial section is used for columns while beams are welded from 2x1/8" (5.08cm x 0.32cm) web and 1-1/2x1/4" (3.81cm x 0.64cm) flanges steel bars, thus assuring strong-column weak-beam configuration. Core regions of panel zones are designed with steel plates of 4x3" (10.16cm x 7.62cm) with a thickness of 0.75" (1.91cm). Columns are designed to be 21" (53.35cm) height for each story and beams span are 25" (63.5cm). The final assembly defines a height to width aspect ratio of H/W=1.75 which preserves realistic dynamic properties of similar large scale building frame structures, and allows structural yielding in a controlled manner within the force and stroke range of the hydraulic loading actuators. A set of peripheral bracing frame is designed to confine the buckling and out-of-plane deformation when the MRF is subjected to extreme actuator forces. Steel channel C6x13 commercial section is used with the strong axis oriented in the MRF out-of-plane direction. Figure 2.7 shows a picture of the completed MRF test specimen (white frame in the center) as well as the support bracing frame (black frames on both sides). High strength threaded bars are available to tie the peripheral frame with the concrete reaction system in both directions. Detailed design and assembly of the steel specimen on the concrete reaction are shown in Figure 2.8 through Figure 2.10.

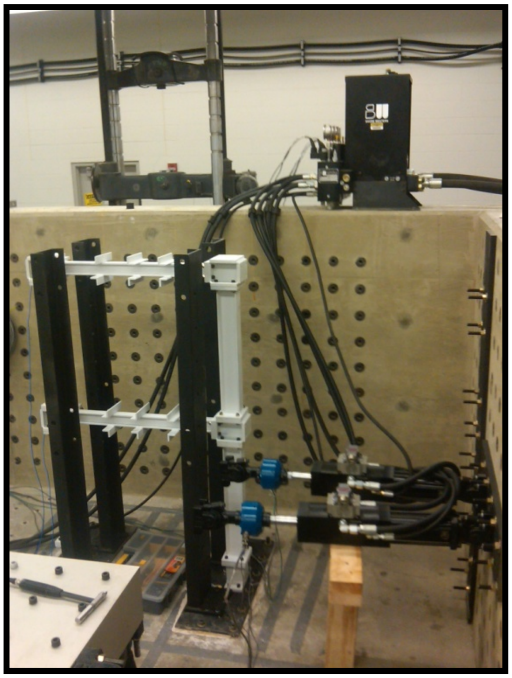

Figure 2.7 Steel Moment Resisting Frame Specimen

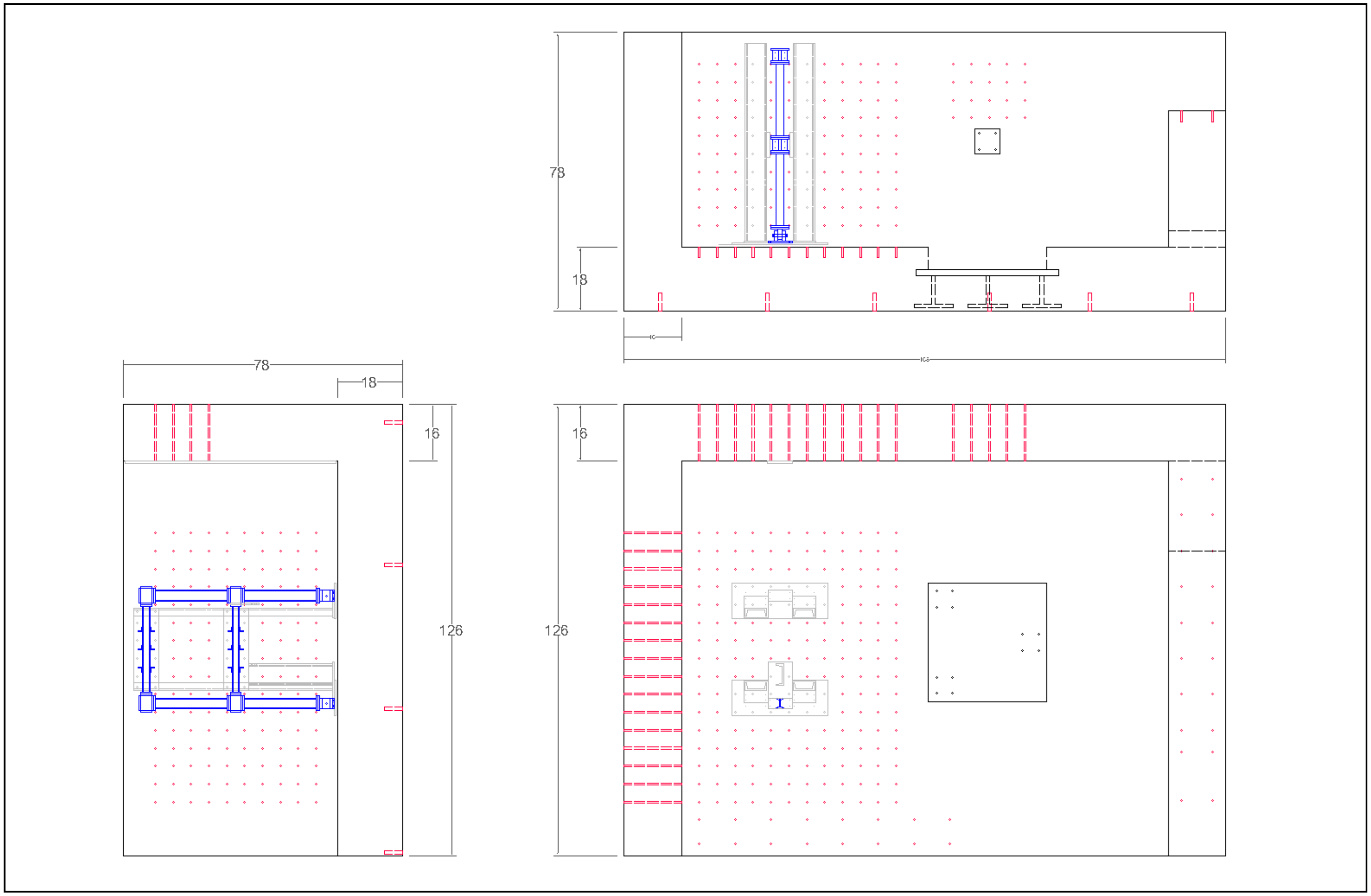

Figure 2.8 Assembly of the MRF Specimen

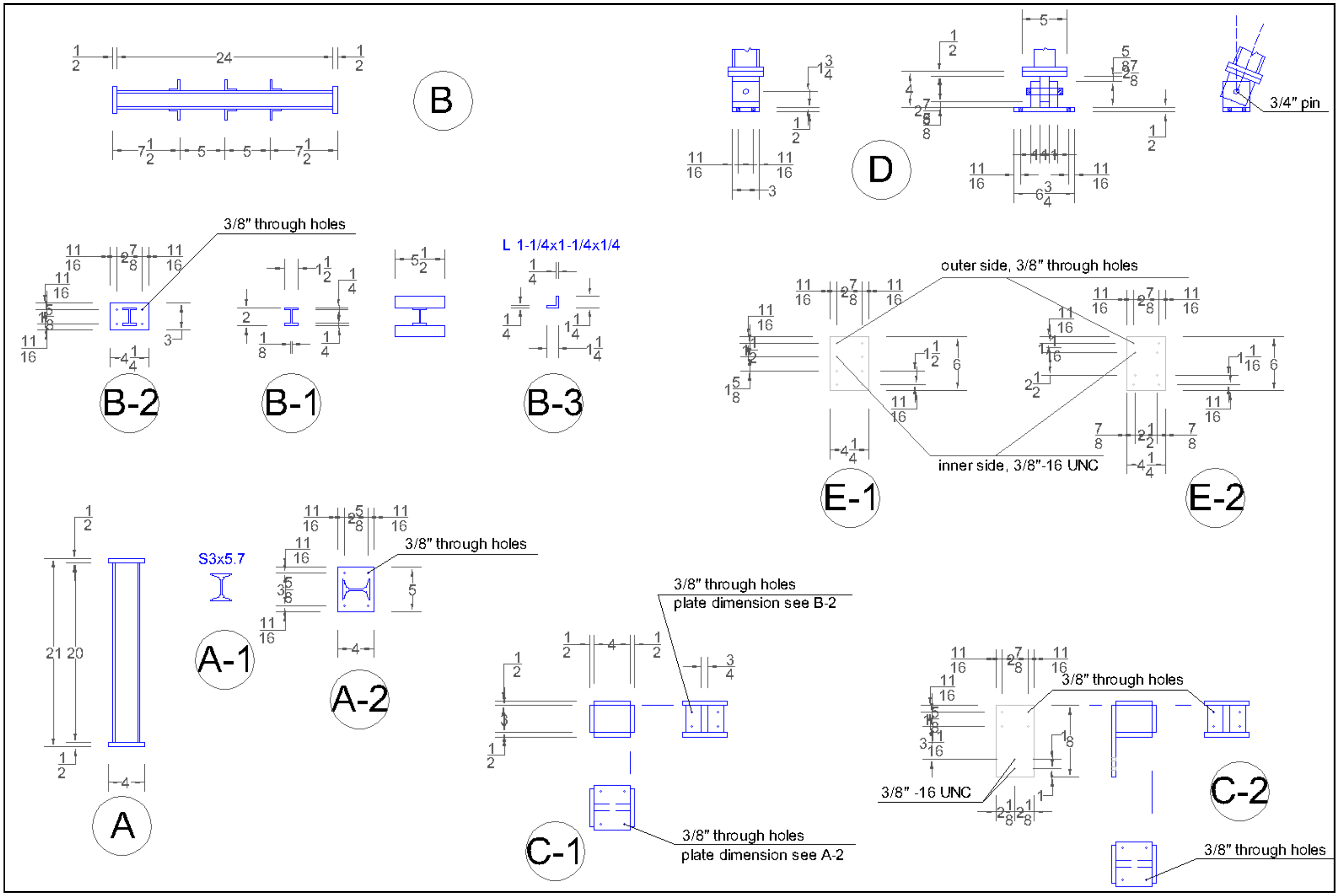

Figure 2.9 MRF Specimen Design

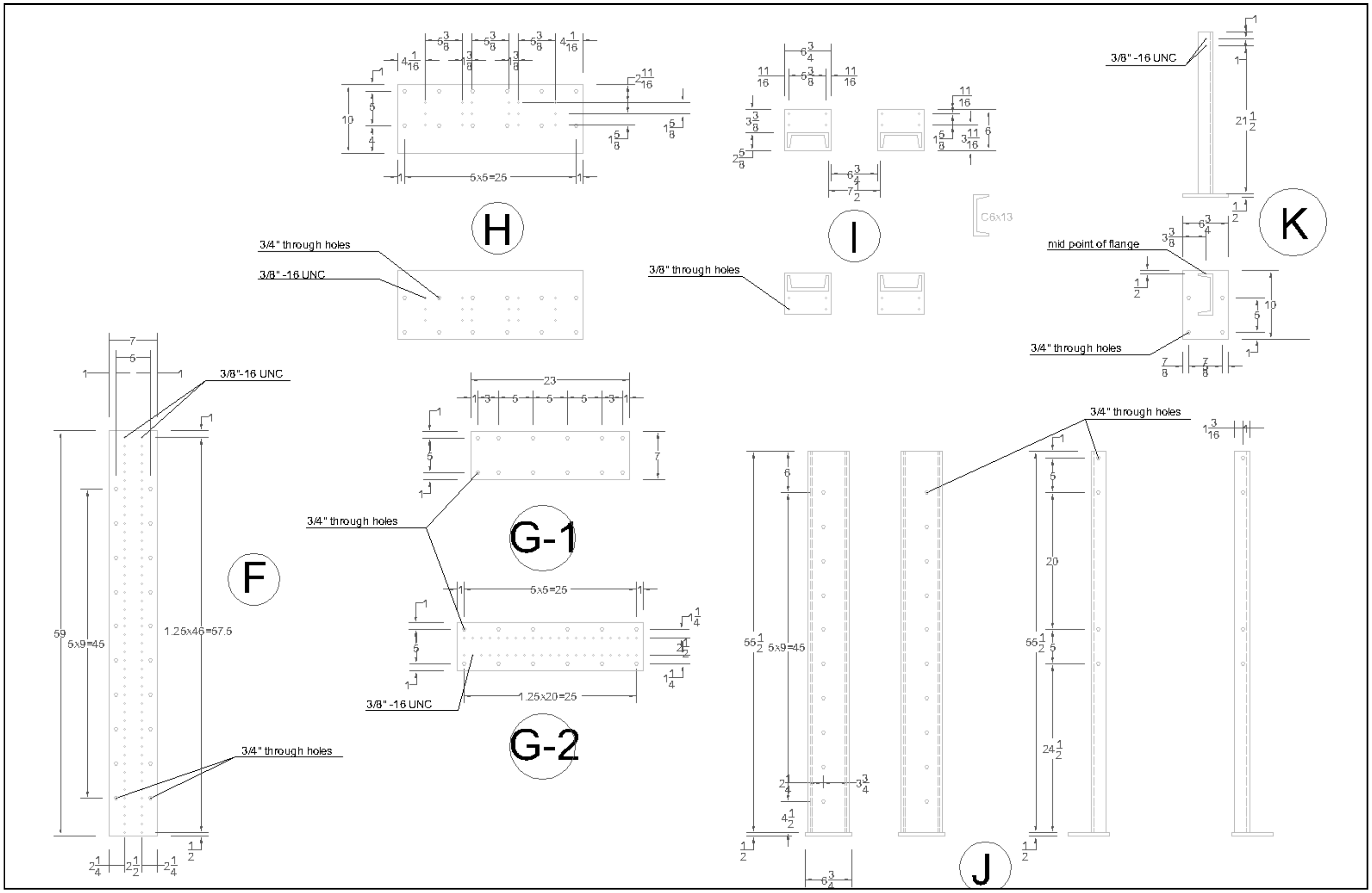

Figure 2.10 Peripheral Bracing Frame Design

2.3 Real-time Control System

This component coordinates all physical and computational actions to meet the timing constraints of a real-time hybrid simulation. A reconfigurable design facilitates interoperability in the computing and networking hardware. An initial prototype system is developed (Huang, et al., 2010) using a common-off-the-shelf Linux platform, with a lightweight C++ implementation to achieve functional correctness and temporal predictability. The prototype system is designed to encapsulate each cyber and physical element as a distinct component since RTHS is largely a data-flow instead of object oriented system; flow ports are defined to enforce type safety for communication between components. The system also allows timing constraints to be associated with each component and appropriate handlers to be dispatched if a constraint is violated at run-time. This open source environment provides optimized data flow management feature and allows maximum flexibility in system configuration, e.g. it supports both a time and event driven architecture that can be triggered by either hardware clock or software based mechanism. A timing instrumentation points can also be inserted to measure the actual execution time of each component for performance analysis. Experimental measurements indicate that the I/O (NI PCI-6251) reading and writing normally takes a fraction of one millisecond and the timing variation increases as the computational load increasing. Latency is added between components to reduce this sampling jitter, but experimental results do not show significant improvement.

Despite all the features and capabilities discussed above, the downsides of the prototype system are: a lack of language level support for sophisticated mathematical operations to implement advanced applications; the OS needs to be configured for hardware compatibility which significantly extends the development period and increases maintenance cost; and software development also requires the end user to have system level expertise for basic use and sustainability. Considering the design objective, to develop a sustainable system that supports rapid turn-around from experiment design to deployment, the RTHS framework development to date at IISL is based in MATLAB (The Mathworks Inc., 2011a). This commonly used software has rich libraries to perform dynamical system modeling and simulation and is familiar to most domain users. SIMULINK is an interactive graphical environment integrated within MATLAB that allows block diagram control system design. More complicated algorithms can be programmed as Embedded functions or S-functions in SIMULINK, and stand-alone C code can then be generated using the Real-Time Workshop. Object code generated from host computer is linked with a light-weight, real-time kernel which provides basic interrupts and I/O services to generate executables directly atop the target machine hardware.

A high performance Speedgoat/xPC (Speedgoat GmbH, 2011) real-time kernel (Figure 2.11) is configured as the performance target PC for the proposed framework. It is equipped with state-of-the-art Core i5 3.6 GHz processor optimized for complex and processing intensive models to execute in real-time. Performance 4096 MB DDR2 RAM memory is configured for the system. An industrial mainboard with 4 PCI and 2 PCIe slots are available for later I/O expansion purposes. High-resolution, high accuracy 18-bit analog I/O boards are integrated into this digital control system that supports up to 32 differential simultaneous A/D channels and 8 D/A channels, with a minimum I/O latency of less than 5 μs for all channels. PCI Intel PRO/100 S Ethernet card for using xPC Target's Raw Ethernet driver blockset is also configured to facilitate the distributed task execution among multiple targets. The system is intended to be reconfigurable and will allow any researcher to implement a control system, so long as it can be executed in real-time.

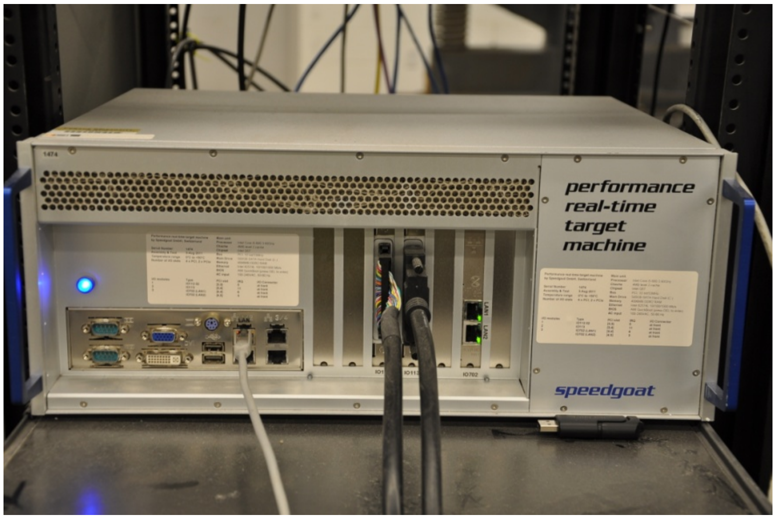

Figure 2.11 Speedgoat/xPC Target System

The xPC Target is a flexible real-time testing solution that combines target machine and I/O modules that can both be chosen from a large variety of hardware options, at significant less cost than a proprietary DSP system. Another xPC target machine used within this study is a standard desktop PC with a Pentium 4 2.6 GHz processor and 512 MB memory. The I/O device used is a NI PCI-6251 multifunction DAQ board (National Instruments, 2011) with a resolution of 16 bits that supports a maximum sample rate of 1.25 MS/sec. 8 differential A/D channels and 2 D/A channels are available that supports sequential sampling only, i.e. multiplexed sampling with multiple channels share one

A/D converter (Figure 2.12). Using a multiplexer that switches among multiple input channels can substantially reduce the cost of a DAQ system, but the tradeoff is that more system latency is introduced. Channel-to-channel crosstalk also tends to occur in a multiplexing system when the voltage applied to any one channel affects the accurate reading of adjacent channels. Short high quality cables can minimize crosstalk and noise issues etc. A NI BNC-2120 shielded connector block is configured to be the terminal to connect I/O signals for this 2nd xPC. Settling time is another major factor that affects sampling accuracy. It is advisable to configure channel scanning order to avoid switch from a large to small input range to minimize settling time. Inserting a ground channel between signal channels is another technique used to improve settling time. In practice, the sampling rate must be set more than twice the signal's highest frequency component to avoid aliasing, and preferable between five and ten times to maintain frequency accuracy. A hardware vendor provided chart is shown in Figure 2.13 to compare the target system real-time code execution performance, using different family of CPUs. The purple bar is obtained using a system with Intel Core 2 Duo 3.16 GHz processor. The configured performance Speedgoat hardware is an upgraded system that is expected to exceed the execution efficiency of all listed systems.

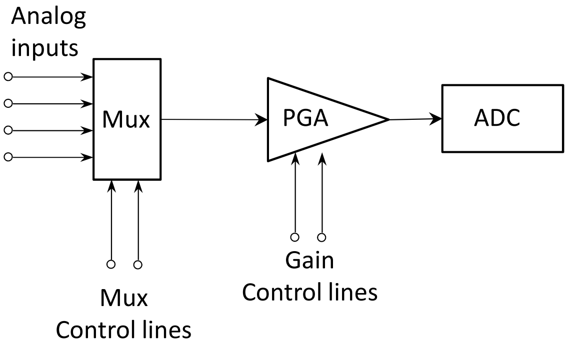

Figure 2.12 Multiplexed Sampling

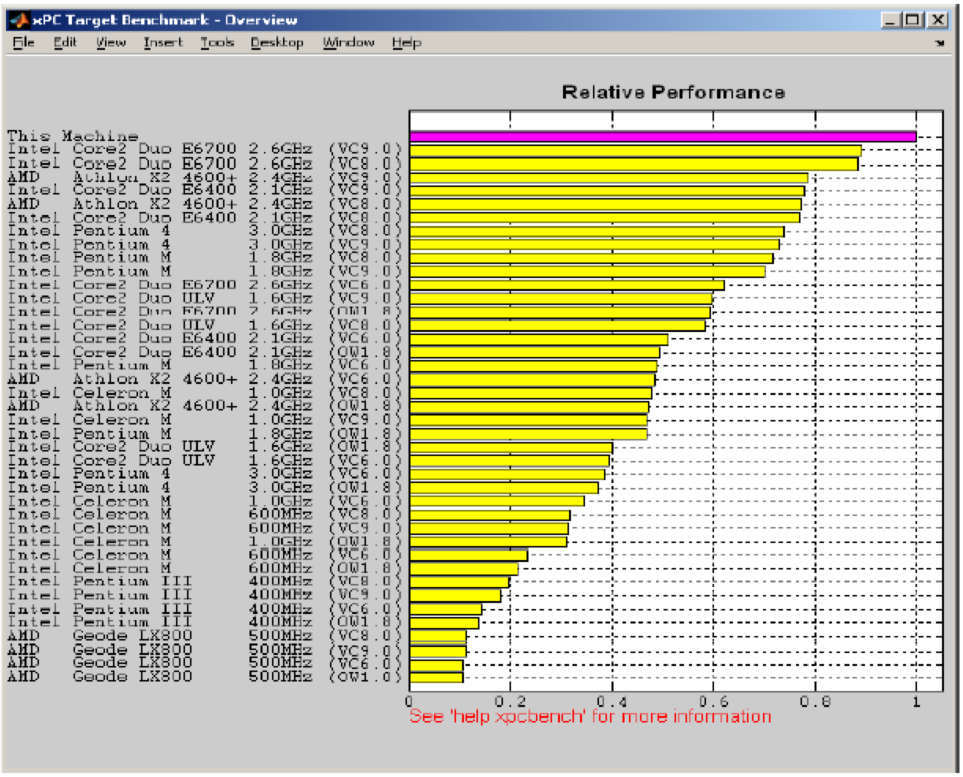

Figure 2.13 Target PC Execution Performance (after Speedgoat GmbH)

A 3rd DSP system utilizes a dSPACE 1006 processor board at 2.6 GHz that has 256 MB local memory for executing real-time applications, and 128 MB global memory for exchanging data with the host PC. A DS2201 Multi I/O board can provide up to 20 simultaneous A/D channels and 8 D/A channels with a conversion time of 32.5 μs for all 20 channels, which is adequate for the intended purposes.

2.4 Sensing and Actuation (SAS) System

The DSP system is combined with a Shore Western SC6000 analog servo-hydraulic control system (Shore Western Manufacturing, 2011) to enable high precision motion control of hydraulic actuators. This controller chassis is shown in Figure 2.14 that houses three servo control boards, each of which has two servo-valve amplifiers and two valve drivers that can be operated either independently or synchronously. Four transducer amplifiers are built into each servo board, which allow the controller to accept both DC and AC signals, and thus enable the controller to be configured either in displacement or force feedback control mode. Two software programmable controlled monitor points are available per control board for monitoring up to two specific locations in the analog circuit. 24 discrete channels of digital I/Os are built into each board for on-off control sequences e.g turn on/off the solenoids of hydraulic service manifold (HSM) channels. Servo-valve dither frequency is selectable for multiple frequencies between 100 and 1000Hz. Valve balance range is 20% of maximum servo valve current level. Servo loop are software configurable for P, PD PID, or PIDF type with selectable inputs for the command. The controller can also accept an external input for operation from an external source e.g. the xPC to form a real-time outer-loop controller.

Figure 2.14 SC6000 Servo-hydraulic Control System

Bowen lab in Purdue University houses a 90 gpm (342 liters/min) MTS hydraulic pump operated at 2,800 psi (19.3 MPa). Span of 85' (26m) hydraulic extension lines are tied into the closest existing hydraulic power supply station. Both pressure and return flexible hoses are selected to be 1.25" (3.18cm) diameter that is rated at 3,500 psi (24 MPa). The extension line can transmit well above 30 gpm (114 liters/min) fluid to power multiple actuators to their full capacity. Lines are split into two HSMs near the end of reaction test station. HSMs are rated at 60 gpm (228 liters/min) and 3,000 psi (20.7 MPa) oil service that is designed to regulate hydraulic fluid power before connecting to each individual actuator. One HSM is dedicated for the six DOF shake table and the other with four independent controllable outlets for CIRST. This hydraulic system meets the high force requirements needed for our testing specimen.

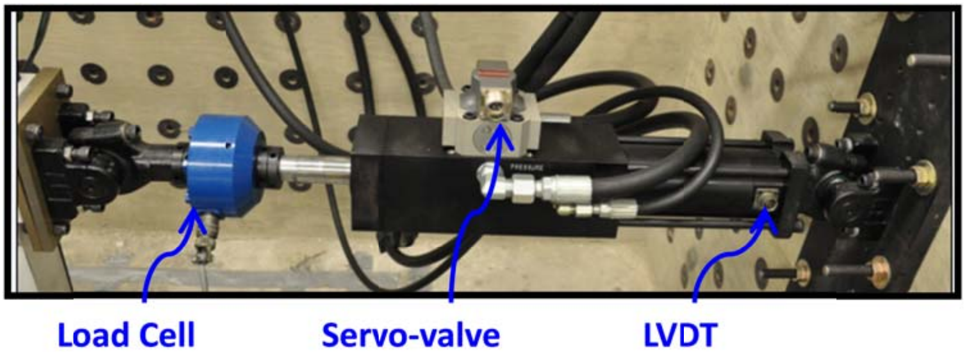

Figure 2.15 Servo-hydraulic Actuator

The SAS measures the responses of the physical components to apply appropriate control actions during each test. Actuation is performed with up to six low-friction, double-ended, dynamically-rated hydraulic linear actuators (Figure 2.15). Four actuators have a nominal force capacity of 2.2 kip (9.8 kN) and are equipped with 10 gpm (37.9 liters/min) servo-valves, the remaining two actuators are 1.1 kip (4.9 kN) with 5 gpm (19 liters/min) servo-valves. All actuators are operated at the nominal pump fluid pressure of 2,800 psi (19.3 MPa). Each actuator is equipped with both an LVDT and a force transducer, allowing the flexibility to be used either in displacement or force feedback control modes (or mixed mode). The maximum stroke for all actuators is 4". Sensing is achieved using various types of sensors that are needed both to measure structural responses from the physical elements of the structure and to control actuation devices (force, displacement, pressure). Accelerometers, displacement sensors, strain gages, and load cells are all available for use within the CIRST for real-time hybrid simulations.

A linear variable differential transformer (LVDT) consists of a coil assembly and a core. The coil assembly consists of three electric coils of wire wound on a stationary hollow form. A moveable core can slide freely through the center of the form and is attached to the object whose position is being measured. The middle coil is the primary coil, which is excited by an AC source. The magnetic flux produced by the primary coil is coupled to the two secondary coils, inducing an AC voltage in each coil. Two secondary coils are wound in the opposite directions so that the two signals out of them are 180 degree out of phase. Therefore phase of the output signal determines direction and the amplitude determines distance. Displacing the core to a positive direction causes its associated secondary to be more strongly coupled to the primary than the other secondary. The resulting voltage difference between two secondary is in phase with the primary voltage (positive displacement), whose amplitude is proportional to the core displacement. Similarly the out of phase voltage indicates negative displacement. Therefore, by measuring the voltage amplitude and phase, the displacement and direction of core motion is determined. The direct output voltage from LVDT is an AC waveform which does not have polarity. SW controller provides LVDT signal conditioner that generates a 10,000 Hz sinusoidal signal as an excitation source for the primary core. The circuitry synchronously demodulates the secondary output signal with the primary excitation source. Demodulator offset and phase constants need to be calibrated using an external oscilloscope to maximize the performance of each individual actuator LVDT. Finally, the resulting DC voltage (proportional to core displacement) can be used for feedback control design purposes.

A load cell converts a force into an electrical signal in two steps. First the force being sensed yields a mechanical deformation using the strain gauge. Strain then causes the effective electrical resistance to be varied in proportion to the applied force. A load cell usually consists of four strain gauges in a wheat-stone bridge configuration. The bridge consists of four arms with an excitation DC voltage (5 Volt for SW actuators used in this study) that is applied across the bridge. Balanced voltage is achieved when the output voltage is zero. The change in the resistance of any arm results in a nonzero output voltage. Depending on the number of active arms, the strain gauge can be categorized into quarter, half and full bridge configurations. The sensitivity of the bridge output voltage to strain increases with the number of active gauges. Lead wire resistance can be a major source of measurement error in practice so that it needs to be corrected for long lead wire. The output of a strain gauge is in general quite small so that amplifiers are normally integrated into the strain gage signal conditioner. Shunt calibration is a procedure that simulates the input of strain by changing the resistance of one bridge arm to a large known quantity. The corresponding pre-calibrated force measure can then be compared to the voltage output measured by the Shore Western controller to calibrate each individual channel signal conditioner gains.

2.5 RT-Frame2D

RT-Frame2D (Castaneda, 2012) is the finite element computational tool developed in the IISL to perform nonlinear dynamic analysis of steel buildings under real-time execution conditions. The mass is modeled with a concentrated-lumped scheme by evenly distributing the mass contribution carried by horizontal/beam elements at corresponding global translational DOFs. Damping effects can be represented with either a mass/stiffness proportional damping or a Rayleigh damping modeling options.

Column elements are modeled as linear-elastic elements with optional linear zero-length rotational springs. Second order effects (P-Delta) are modeled by assuming the accumulated weight at each floor acting as constant compressive-axial forces on the corresponding column elements to calculate the geometric stiffness matrices that can be globally assembled to account for the overall P-Delta effect. Beam elements can be represented by two schemes. A moment-curvature type nonlinear beam element; which implements a hysteresis model to represent yielding locations at element ends that occur at the moment resisting beam-column connections. The hysteresis properties can be predefined depending on the element section. The yielding locations can be represented with either a spread plasticity model (SPM) or a concentrated plasticity model (CPM), where yielding is limited only to the ends of the member while the interior is assumed to be elastic. Additionally, an elastic beam element with a linear/nonlinear zero-length rotational springs, located at the element ends, is also available. Hysteresis properties can also be predefined for each spring element. Two different material models are available for the nonlinear beam model; a bilinear and tri-linear model with kinematic hardening. In the SPM, a simple supported beam model is utilized for derivation of the 2x2 stiffness matrix relating moments and rotations at ends as follows:

$$\begin{bmatrix} M_A \\ M_B \end{bmatrix} = \widetilde{K} \begin{bmatrix} \theta_A \\ \theta_B \end{bmatrix} = \begin{bmatrix} k_{AA} & k_{AB} \\ k_{BA} & k_{BB} \end{bmatrix} \begin{bmatrix} \theta_A \\ \theta_B \end{bmatrix} \tag{2.3}$$

where

$$k_{AA} = \frac{12EI_0 EI_A EI_B}{D_{et} L} \left(f'_{BB} GA_Z L^2 + 12EI_0 EI_A EI_B \right)$$

$$k_{AB} = k_{BA} = -\frac{12EI_0 EI_A EI_B}{D_{et} L}\left(f'_{AB} GA_Z L^2 + 12EI_0 EI_A EI_B\right)$$

$$k_{BB} = \frac{12EI_0 EI_A EI_B}{D_{et} L}\left(f'_{AA} GA_Z L^2 + 12EI_0 EI_A EI_B\right)$$

$$f'_{AA} = 4EI_A EI_B + (EI_0 - EI_A)EI_B(6\alpha_A - 4\alpha_A^2 + \alpha_A^3) + (EI_0 - EI_B)EI_A \alpha_A^3$$

$$f'_{AB} = -2EI_A EI_B - (EI_0 - EI_A)EI_B(2\alpha_A^2 - \alpha_A^3) - (EI_0 - EI_B)EI_A(2\alpha_B^2 - \alpha_B^3)$$

$$f'_{BB} = 4EI_A EI_B + (EI_0 - EI_A)EI_B \alpha_A^3 + (EI_0 - EI_B)EI_A(6\alpha_B - 4\alpha_B^2 - \alpha_B^3)$$

$$D_{et} = GA_Z L^2 (f'_{AA} f'_{BB} - f'^{\,2}_{AB}) + 12EI_0 EI_A EI_B (f'_{AA} + f'_{BB} - 2f'_{AB})$$

GA and L are the shear stiffness and the length of the member, respectively. EI_A and EI_B are the instantaneous flexural stiffness at the member end sections, whose values are progressively updated from the hysteresis model. EI_0 is the flexural stiffness at the center of the member. α_A, α_B are yield penetration parameters that are functions of the moment distribution and previous yield penetration history. Therefore, the 4x4 element stiffness matrix $\widetilde{K}_e$ can be derived by using the equilibrium matrix between shear forces and moments as:

$$[V_A \quad M_A \quad V_B \quad M_B]^T = \widetilde{R}_e \left[M_A \quad M_B\right]^T \tag{2.4}$$

where, $\widetilde{K}_e = \widetilde{R}_e \widetilde{K}_s \widetilde{R}_e^T$

The panel-zone is defined as the core region where forces from adjacent beam and column members are transferred. The panel-zone effect is important to characterize the stiffness influence of structural joints. A new model proposed by (Hjelmstad & Haikal, 2006) is implemented in RT-Frame2D. Two models are offered: a rigid-body version and a linear version with bidirectional tension/compression and shear distortion effect. The model is defined by two translational and one rotational DOF at the center of the panel zone, and three deformation modes for the panel zone itself. The DOF belonging to each beam/column element end that is connected to the panel zone can be associated to those at its center via a transformation matrix that ensures kinematic compatibility as well as enforces the equilibrium equations. This model avoids for the inclusion of many DOF associated with the ends of beam/column elements sharing a panel zone when solving the EOM.

Two integration schemes are available for solving the nonlinear equation of motion and evaluate the nonlinear response; the explicit-unconditional stable CR algorithm (Chen & Ricles, 2008) and the implicit-unconditional stable Newmark-Beta method with constant acceleration (Newmark, 1959). For a structure with the EOM:

$$M\ddot{x}(t) + C\dot{x}(t) + Kx(t) = F(t) \tag{2.5}$$

the CR algorithm calculates the velocity and displacement of *(i+1)*th time step based on known response quantities of i^{th} time step only, so that it is an explicit integration scheme.

$$\begin{aligned} \dot{x}_{i+1} &= \dot{x}_i + \alpha_1 \cdot \Delta t \cdot \ddot{x}_i \\ x_{i+1} &= x_i + \Delta t \cdot \dot{x}_i + \alpha_2 \cdot \Delta t^2 \cdot \ddot{x}_i \end{aligned} \tag{2.6}$$

It can be demonstrated that by assigning proper integration constants in equation (2.7), the poles can be enforced to be within the unit circle in the discrete “z” domain.

Therefore the discrete transfer function corresponding to the difference equation of the integration scheme is unconditionally stable.

$$\alpha_1 = \alpha_2 = 4 \cdot (4M + 2\Delta tC + \Delta t^2 K)^{-1} \cdot M \qquad (2.7)$$

The acceleration at the *(i+1)th* time step can therefore be calculated by enforcing the equilibrium and evolving to the next integration time step.

$$\ddot{x}_{i+1} = M^{-1}(F_{i+1} - C\dot{x}_{i+1} - Kx_{i+1}) \qquad (2.8)$$

RT-Frame2D has been implemented as a MATLAB Embedded function format. The Embedded function (Embedded MATLAB toolbox) supports efficient code generation to accelerate fixed-point algorithm execution for embedded systems. Additionally, MATLAB/SIMULINK is used to integrate the computational tool with the remaining RTHS components so a unique platform can be generated for real-time execution. Finally, the MATLAB/xPC Target is used to generate and compile a C-source code from the SIMULINK model (host PC) that can be downloaded into a target real-time kernel (target PC) for execution.

CHAPTER 3
RTHS SYSTEM SENSITIVITY STUDY

Consider the case of a SDOF structure that is divided into a numerical (denoted by subscript *n*) and an experimental (subscript *e*) portion. A certain amount of mass (*M*), stiffness (*K*) and damping (*C*) are assumed in each portion and the total reference structure system is the summation of both. The reference structure EOM is expressed in equation (3.1), when the structure is subjected to a ground motion.

$$(M_n + M_e)\ddot{x} + (C_n + C_e)\dot{x} + (K_n + K_e)x = -(M_n + M_e)\ddot{x}_g \tag{3.1}$$

Because perfect synchronization cannot be achieved in general, a RTHS implementation can be expressed using different state variables for each portion. Here *x* is defined as the displacement coordinate for the numerical model, and x_m as the experimentally measured displacement. The resulting hybrid system EOM is thus

$$M_n\ddot{x} + C_n\dot{x} + K_n x + M_e\ddot{x}_m + C_e\dot{x}_m + K_e x_m = -(M_n + M_e)\ddot{x}_g \tag{3.2}$$

Without loss of generality it can be assumed that $x = A\sin\omega t, x_m = \Delta A\sin\omega(t - \delta t)$ where A is the response amplitude and ω is the fundamental frequency of the SDOF reference structure; Δ and δt represent the amplitude and phase errors, respectively. By assuming a small δt**,** the de-synchronized states can be approximated through a Taylor series expansion as

$$\begin{aligned} x_m &= \Delta A \sin \omega(t-\delta t) \approx \Delta A(\sin \omega t - \omega \delta t \cos \omega t) = \Delta(x - \delta t \dot{x}) \\ \dot{x}_m &\approx \Delta(\dot{x} - \delta t \ddot{x}) \\ \ddot{x}_m &\approx \Delta(\ddot{x} + \omega^2 \delta t \dot{x}) \end{aligned} \tag{3.3}$$

A linearized RTHS system is therefore constructed by substituting equation (3.3) into equation (3.2)

$$\begin{aligned} &(M_n + \Delta M_e - \Delta \delta t C_e)\ddot{x} + [C_n + \Delta C_e + \Delta \delta t(M_e \omega^2 - K_e)]\dot{x} \\ &+ (K_n + \Delta K_e)x = -(M_n + M_e)\ddot{x}_g \end{aligned} \tag{3.4}$$

A physical actuation control system normally introduces phase lag i.e. $\delta t > 0$ so that the negative stiffness term K_e in equation (3.4) plays the most critical role in RTHS stability. This observation is consistent with the conclusion obtained through an energy approach in (Horiuchi, Inoue, Konno, & Namita, 1999). Another interesting observation is that the amount of mass reduction in equation (3.4) is proportional to C_e which leads to a faster responded RTHS system when subjected to tracking delay.

The states in equation (3.1) and equation (3.4) are now synchronized so that a direct comparison of system parameters can be made to gain additional insights into the dynamic behavior of the hybrid system. Note that both Δ and δt can be very complicated and nonlinear in nature for a realistic physical system, especially when advanced control strategies are applied in a closed-loop system. Some cases are identified and discussed below to understand the sensitivity of the hybrid system to the de-synchronization error.

Case 1: Perfect synchronization is achieved with both $\Delta = 1$ and $\delta t = 0$. The RTHS system in equation (3.4) is obviously identical to equation (3.1), reaching the ultimate goal of improving control performance and reducing RTHS error.

Case 2: When $M_n >> M_e, C_n >> C_e, K_n >> K_e$, i.e. the scale of experimental portion is negligible compared with the numerical counterpart. Both equation (3.1) and equation (3.4) converge to the numerical substructure only so that the RTHS error in this case can be less significant even with the existence of relative large *Δ* and *δt*. This conclusion can be intuitively generalized to other types of hybrid test specimens e.g. RTHS error is intrinsically less sensitive to the de-synchronization/tracking error if only non-structural components are tested physically. A good qualitative measure is the ratio of the total generalized forces between the experimental and computational components.

Case 3: Another special case is when both substructures have identical modal characteristics i.e. damping ratios and natural frequencies. This situation is achieved by enforcing the computational model to be exactly linear proportional to experimental substructure so that $M_e = \lambda M_n, C_e = \lambda C_n, K_e = \lambda K_n$, where *λ* is an arbitrary constant. In this case $\omega^2 = (K_n + K_e)/(M_n + M_e) = K_e / M_e$ and the artificial damping terms in equation (3.4) are cancelled out. Stability is not a concern in this case despite the occurrence of large de-synchronization error.

Case 4: The most generalized RTHS setup is when an arbitrary allocation is allowed between the mass and stiffness of the substructures. Assume $\alpha = M_e / M_n, \beta = K_e / K_n$ so that the artificial RTHS damping term in equation (3.4) is:

$$M_e\omega^2 - K_e = M_e(K_n + K_e)/(M_n + M_e) - K_e = (\alpha - \beta)/(1 + \alpha)K_n \qquad (3.5)$$

It is easy to observe the worst-case scenario occurs when K_n is zero which yields a singular configuration since $\beta \rightarrow \infty$ (i.e. infinity negative damping). In addition $\alpha \rightarrow 0$ may be assumed that provides no cancellation of the negative damping. This situation has been observed during validation experiments, and in practices considered herein a small K_n has to be included to perform a successful RTHS.

Applying similar reasoning, a controller that is too aggressive can sometimes cause a phase lead i.e. $\delta t<0$ which results in artificial added damping into equation (3.4), assuming $\alpha>\beta$ holds true (otherwise, the reverse reasoning needs to be applied). Although this may help to stabilize the RTHS system, test accuracy will still be severely compromised. Although most applications fall within cases 2, 3 and 4, the experimental studies considered herein focus on case 4, the most challenging case, to examine the limit of tracking controller performance. It is demonstrated in Chapter 7 that even a fraction of a milli-second delay can cause RTHS instability, using the proposed worst-case RTHS test matrix. Therefore a high performance motion tracking control strategy becomes an indispensable component of a high fidelity RTHS framework. More quantitative characterization of Δ and δt will be discussed in the following chapters, along with several control strategies to minimize these errors.

CHAPTER 4
MODELING OF ACTUATOR DYNAMICS WITH UNCERTAINTY

One of the main challenges in conducting a successful and accurate hybrid testing is to synchronize the displacement and force boundary conditions between the numerical and the experimental substructures. Although inevitable computational and communication delays are observed among various cyber and physical components, experimental studies (Carrion & Spencer, 2007) reveal that the phase lag associated with hydraulic actuator dynamics contributes the largest portion to this apparent delay in the time domain. A dynamic model for a servo-hydraulic actuation and control system is first introduced in this Chapter. The experimental observations of the physical system nonlinearities motivate the subsequently proposed uncertainty modeling techniques, which can be used to simulate both parametric and non-parametric uncertainties. Sensitivity study of the actuator model is then performed to analyze the variation of actuator dynamics with respect to several key parameters. The goal of this chapter is to introduce some modeling and analysis tools that can potentially improve the performance of the controller design. The RTHS system stability and accuracy can then be analyzed in a similar manner to understand the system behavior when subjected to nonlinearity, modeling inaccuracy and identification error etc. The introduced modeling tools assume linear system formulation with lower and upper bounds for individual uncertain components.

This simple modeling approach can be very useful when dealing with complicated system in which closed-form parameterized model may not even be available. A worst-case system realization can therefore be constructed through combinations of assumed uncertain elements. Important system properties e.g. stability limit and performance specification can be obtained through analyzing this worst-case system.

4.1 Servo-hydraulic Actuator Model

A servo-hydraulic actuator is a type of electro-mechanical device that takes an electrical input and converts it into a piston mechanical linear motion. Both empirical time delay and frequency phase lag modeling approaches are found in the RTHS literature to model this actuator dynamic behavior [(Horiuchi, Inoue, Konno, & Namita, 1999), (Darby, Williams, & Blakeborough, 2002), (Jung & Shing, 2006), (Chen, 2007), (Lim, Neild, Stoten, Drury, & Taylor, 2007), (Ahmadizadeh, Mosqueda, & Reinhorn, 2008)]. However, most of these models do not consider the physics associated with the actuator dynamical components, thus are limited due to simplified assumptions. A parameterized dynamic model(Merritt, 1967) is adopted in this study that considers the various servo-hydraulic actuation and control system components. The block diagram of the overall inner-loop control system is shown in Figure 4.1 that is referred as the plant, unless defined otherwise. The understanding of the plant dynamics is an important initial step to improve the development of high performance outer-loop motion control strategies.

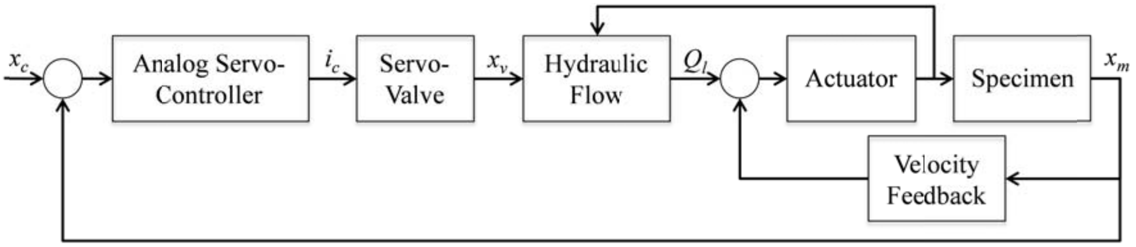

Figure 4.1 Inner-loop Servo-hydraulic Actuation and Control System Model

The basic mechanism of a servo hydraulic actuator (Carrion & Spencer, 2007) is that the servo-valve receives a current input i_c from controller that creates a spool valve displacement x_v.

$$\tau_v \dot{x}_v = -x_v + k_v \cdot i_c \tag{4.1}$$

Controlled hydraulic flow Q_L due to spool displacement causes pressure difference P_L inside actuator chambers that will further induce the piston displacement x_m. The generalized nonlinear flow equation can be linearized to facilitate the control design and frequency domain analysis procedures.

$$\begin{aligned} Q_L &= C_d w x_v \sqrt{\frac{1}{\rho}\left(P_s - \frac{x_v}{\left|x_v\right|} P_L\right)} \\ Q_L &= K_q^{'} x_v - K_c^{'} p_L \end{aligned} \tag{4.2}$$

The continuity equation (conservation of mass flow) essentially governs the behavior of the hydraulic actuator.

$$Q_L = A\dot{x}_m + C_l p_L + \frac{V_t}{4\beta_e}\dot{p}_L \tag{4.3}$$

Parameters in the above equations are defined as follows: k_v is the valve gain, τ_v is the servo-valve time constant, K_q’ is the valve flow gain, K_c’ is the valve flow-pressure gain,

A is the area of the piston, C_l is the total leakage coefficient of the piston, V_t is the total volume of the fluid under compression in both actuator chambers and β_e is the effective bulk modulus. The command displacement x_c is applied by an inner-loop PID controller (proportional gain K_p only within this study).

$$K_p(x_c - x_m) = i_c \tag{4.4}$$

and the equilibrium of force is governed by the equation of motion:

$$f_p = p_L \cdot A = m_t\ddot{x}_m + c_t\dot{x}_m + kx_m + \tilde{f}(t, x_m, \dot{x}_m) \tag{4.5}$$

where m_t, c_t, and k are the mass, damping and stiffness of the piston plus the testing specimen. $\tilde{f}$ represents disturbance terms (e.g. friction) that can be nonlinear in general. After some simple algebraic manipulation, the approximated LTI plant model from the command to the measured displacement can be expressed in equation (4.6) where K_q=K_q'k_v and K_c=K_c'+C_l. The focus of this chapter is to study the actuator displacement input output relationship that is referred as the transfer function in subsequent sections, unless defined otherwise.

$$G(s)=\frac{X_m(s)}{X_c(s)}=\frac{K_p\dfrac{K_qA}{K_c}}{\begin{aligned}&\left(\frac{V_t}{4\beta_eK_c}m_t\tau_v\right)s^4+\left(\frac{V_t}{4\beta_eK_c}m_t+m_t\tau_v+\frac{V_t}{4\beta_eK_c}c_t\tau_v\right)s^3+\left(m_t+\frac{V_t}{4\beta_eK_c}c_t+\dots\right.\\&\left.\frac{A^2}{K_c}\tau_v+c_t\tau_v+\frac{V_t}{4\beta_eK_c}k\tau_v\right)s^2+\left(c_t+\frac{V_t}{4\beta_eK_c}k+\frac{A^2}{K_c}+k\tau_v\right)s+\left(k+K_p\frac{K_qA}{K_c}\right)\end{aligned}} \tag{4.6}$$

It is noted in Figure 4.1 and equation (4.3) that the actuator is dynamically coupled with the test specimen through a natural velocity feedback term. This phenomenon is studied and interpreted as control structure interaction in (Dyke, Spencer, Quast, & Sain, 1995). Experimental studies demonstrate that the linearized model in equation (4.6) can capture the essential dynamics of the actuator. Advanced nonlinear control strategies are found in the literature (Yao, Bu, & Chiu, 2001) in which individual nonlinear terms are designed to be cancelled out to enhance the tracking performance. Although conceptually very attractive, the nonlinear control design may not entirely be suitable for the intended RTHS applications because the experimental substructures are generally unknown. Therefore the plant may not have a closed-form expression, when considering the complex control structure interaction. Accurate modeling is certainly fundamental for any effective control design, but balance is needed to limit the model to be mathematical traceable and, furthermore, controllable. The system equation (4.6) is a linearized model to approximate the physical actuator dynamics. The experimentally identified model using this formulation is therefore only an approximated realization. The modeling error and uncertainty inevitably exist for the physical system, and thus some simulation techniques are introduced below that can account for both parametric and non-parametric uncertainties. Instead of trying to model all physical nonlinearities and input/output disturbances in a strictly closed-form parametric manner, the basic LTI nominal plant is used with uncertainty bounds assumed into model realizations to characterize the physical complexity. System parameter sensitivity studies are performed subsequently, using the concept of a performance degradation curve.

4.2 Modeling of Uncertainty and System Sensitivity Study

A Shore-Western 910D double ended hydraulic actuator was employed in this chapter as the loading device to drive the test specimen. The actuator has a maximum stroke of 6.5” (16.51cm) with a built-in concentric linear variable differential transformer (LVDT), to be readily integrated into a position feedback control system. A Schenck-Pegasus 162M servo-valve rated for 15 gpm (56.8 liters/min) at 1,000 psi (6.9 MPa) pressure drop is used to control the actuator. A servo-valve has a nominal operational frequency range of 0-60 Hz that is driven by a Schenck-Pegasus 5910 digital controller. An Omega load cell with a range of 2 kip (8.9 kN) is included in series with the test specimen to measure the restoring force when needed. A small scale steel compression spring is tested as a first specimen in Chapter 4-6. The linear elastic spring has a nominal stiffness of 215 lb/in (37.6kN/m) and a maximum allowable deflection of 2.77” (7cm). The experimental setup is shown in Figure 4.2.

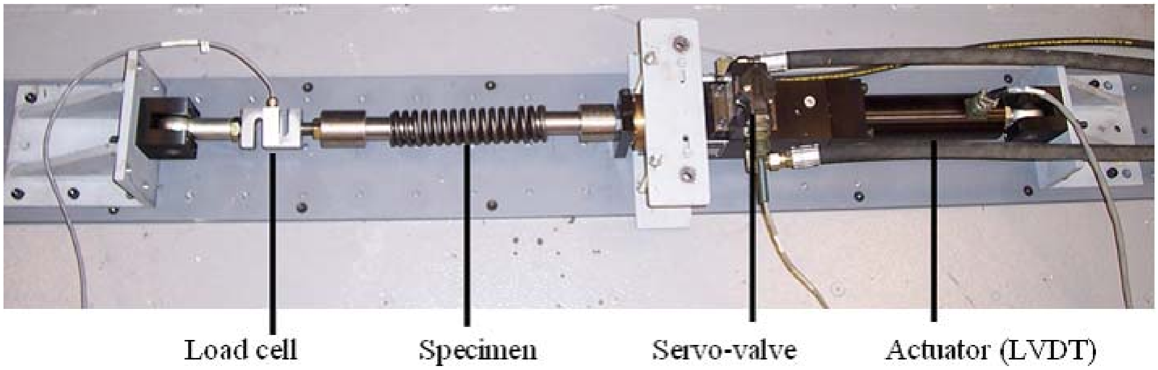

Figure 4.2 Experimental Setup for the Spring Specimen

The actuator is subjected to four different levels of white noise excitation with RMS amplitude of 0.01”, 0.04”, 0.07” and 0.1” (0.025-0.25cm), respectively. The frequency bandwidths for all tests are set to be 0-500 Hz. Two sets of experimental transfer functions are obtained in Figure 4.3 from the command to the measured displacements. The 5910 controller proportional gain is set to two values (1 and 3), under each input excitation level. An ideal actuator tracking control is achieved when the transfer function magnitude is unity and phase lag (phase delay) is zero, over the entire performance bandwidth.

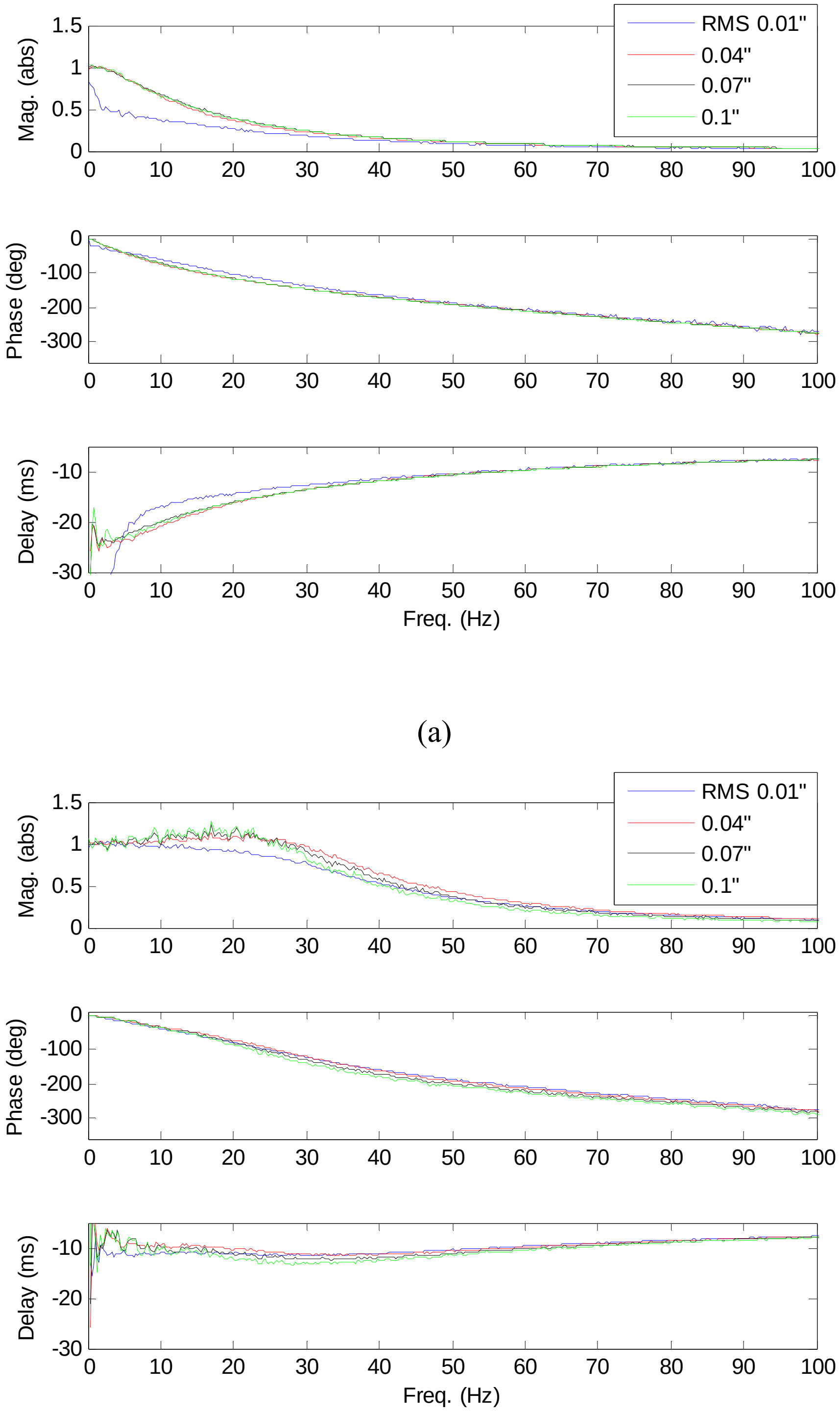

(a)

(b)

Figure 4.3 Plant Transfer Functions with the Spring Specimen
(a): K_p=1; (b): K_p=3

The delay is a measure of the slope of the phase response at a given frequency. It is not surprising that the results in Figure 4.3 show that a moderate proportional gain is desirable to improve the tracking performance, compared to a very low gain. The test under the smallest excitation amplitude (RMS 0.01”) is not capable of overcoming the actuator static friction to excite the mechanical dynamics. Therefore the blue colored transfer functions diverge from others quite significantly in Figure 4.3, demonstrating the inherent nonlinearity in the system. The transfer functions under higher excitation amplitudes are more or less close to each other, although nonlinearity can still be observed over certain frequency ranges. An interesting note is that the system used here appears to have larger nonlinearity under a higher proportional gain setting.

Table 4.1 Identified Nominal Actuator Parameters

K_p	3	mA/in	controller proportional gain
τ_v	4.52e-3	s	servo-valve time constant
K_q	38.97	in^3/s/mA	valve flow gain
K_c'	2.53e-6	in^3/s/psi	valve flow pressure gain
A	0.86	in^2	piston area
C_l	1e-6	in^3/s/psi	piston leakage coefficient
V_t	32.33	in^3	volume of fluid
β_e	95387	psi	effective bulk modulus
m_t	0.06	lb-s^2/in	mass of test specimen
c_t	17.45	lb-s/in	viscous damping coefficient
k	200.32	lb/in	stiffness of specimen

To understand this behavior, a simulation-based parameter study is conducted to evaluate the plant dynamics variation with respect to the individual actuator parameters. Nominal parameters in equation (4.6) are identified and listed in Table 4.1. As an illustration, a 50% normalized uncertainty bound on the mass is assumed. The uncertain plant can assume any mass value between $0.5m_t$ and $1.5m_t$, either greater or less than the nominal value. The simulated transfer functions in Figure 4.4 show how the Monte Carlo samples of uncertain realizations (dot lines) deviate from the nominal plant model (solid line). The worst case realization (dash-dot line) is defined herein as the transfer function with the maximum peak magnitude among all realizations. Similarly the stiffness (k) and the proportional gain (K_p) are chosen as the varying parameter to generate Figure 4.5 and Figure 4.6, respectively. Both parameters assume 50% normalized uncertainty bound too.

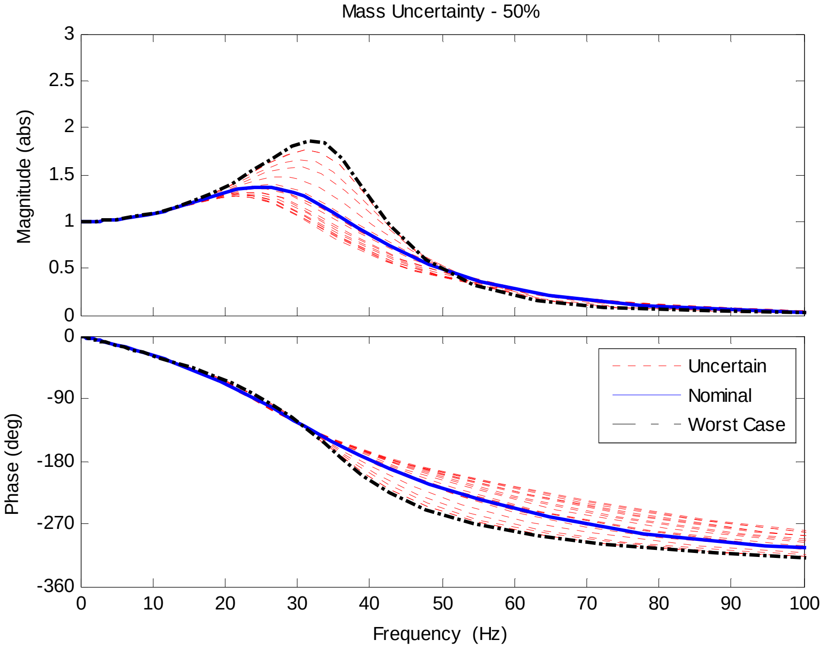

Figure 4.4 Plant Transfer Function Realizations with Mass Uncertainty

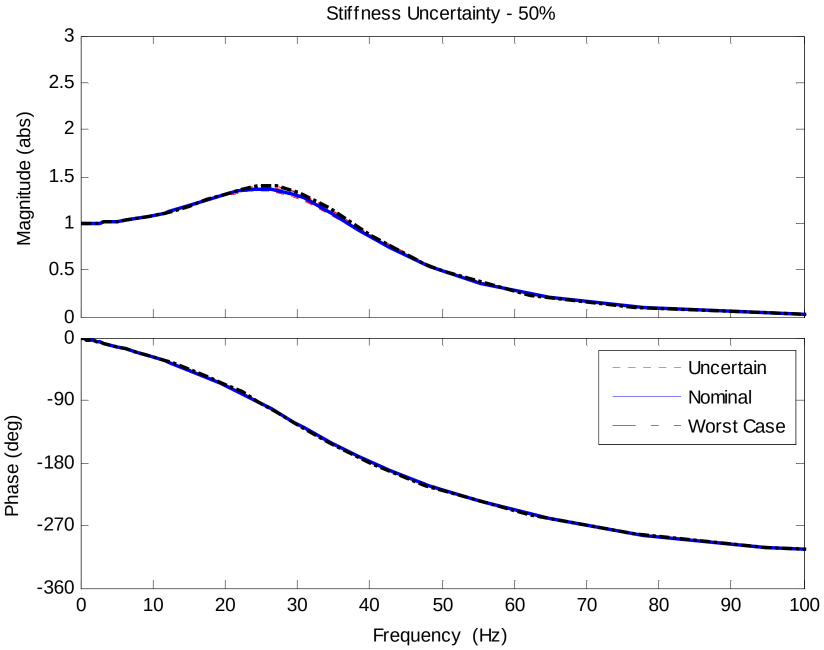

Figure 4.5 Plant Transfer Function Realizations with Stiffness Uncertainty

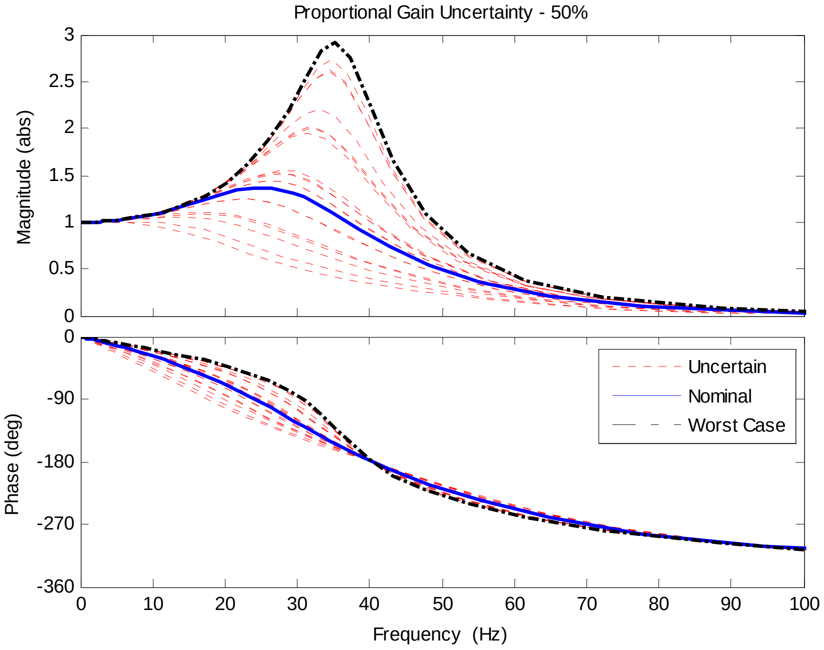

Figure 4.6 Plant Transfer Function Realizations with Proportional Gain Uncertainty

The analysis herein indicates that the plant dynamics is rather insensitive to the stiffness variation (Figure 4.5), but very sensitive to the proportional gain variation (Figure 4.6). Moreover, both the mass and the proportional gain increase result in a plant transfer function magnitude increase. It is therefore advisable to have a less aggressive proportional gain when testing a massive specimen to avoid instability. This numerical sensitivity study may need to be validated more thoroughly, especially when the specimen stiffness is comparable to the actuator loading capacity. Notice that the tracking performance is not likely to satisfy the stringent RTHS requirements, by only tuning the PID control gains. Moreover, a phase tracking improvement is observed to be associated with a trade-off of increased peak magnitude, i.e. a reduced stability margin.

Given a prescribed uncertainty bound, the maximum system gain (MSG) is defined as the peak magnitude of the worst case transfer function realization. MSG is a useful index to characterize the system property (e.g. instability occurs when it approaches to infinity), so that it is used herein to perform the system parameter sensitivity study. The performance degradation curve (PDC) for each varying parameter can be constructed by plotting the MSG vs. the corresponding normalized uncertainty bound. It is expected that PDC is a monotonic non-decreasing function as the uncertainty bound increases.

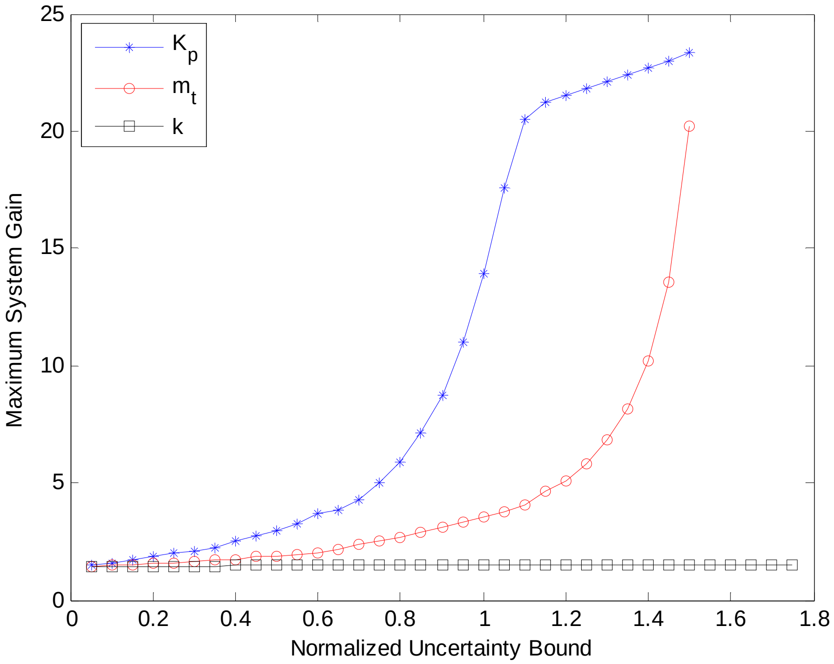

Figure 4.7 Plant Performance Degradation Curve

Figure 4.7 shows comparison of PDCs of the three key plant parameters discussed above. All PDCs start from the nominal system peak magnitude. The slope of the PDC curve measures the sensitivity of system dynamics with respect to the corresponding varying parameter. This study demonstrates more clearly that the servo-hydraulic actuator plant is very sensitive to the proportional gain variation, since the PDC shows the steepest slope, but the plant is rather insensitive to the specimen stiffness change. It is observed that about 150% of the mass or the proportioning gain increase will induce system instability. The observation herein motivates the experimental robustness study in the subsequent chapters. The inner-loop proportional gain is later adjusted within a range of prescribed values besides the nominal value, to evaluate the outer-loop controller robustness in accommodating this significant plant variation.

Time domain analysis is also conducted to compare the step displacement responses of the nominal and the uncertain systems in Figure 4.8 to Figure 4.10. It is observed in Figure 4.8 that an increased mass causes an increase overshoot, which corresponds to the transfer function magnitude peak in Figure 4.4. A longer settling time is observed to be associated with an increased mass. However, the system rise time and steady state response do not change much when the mass varies. It is also observed in Figure 4.10 that an increased proportion gain is beneficial to reduce the system rise time, with a trade-off of a larger overshoot and a longer settling time. Again the step displacement response is observed to be insensitive to the stiffness change in Figure 4.9.

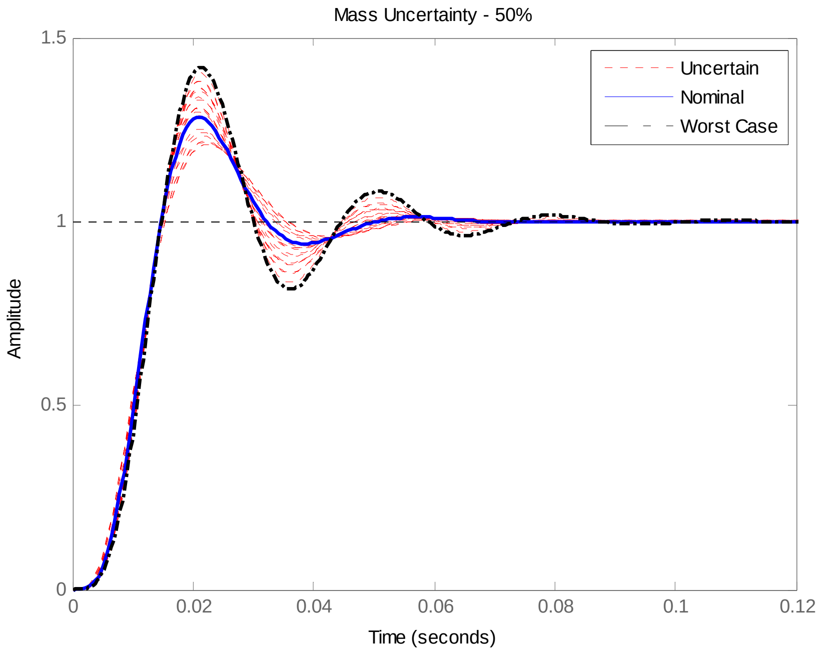

Figure 4.8 Plant Step Displacement Responses with Mass Uncertainty

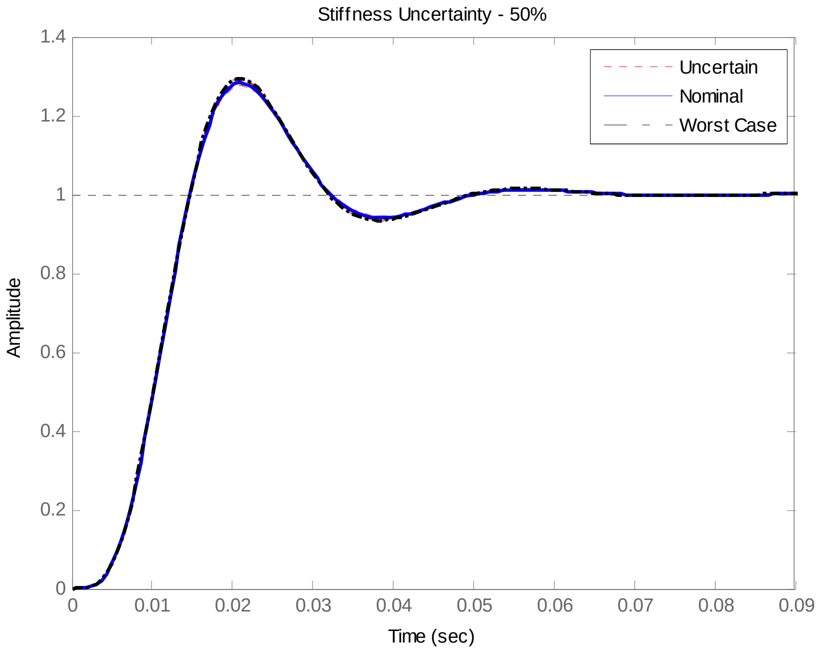

Figure 4.9 Plant Step Displacement Responses with Stiffness Uncertainty

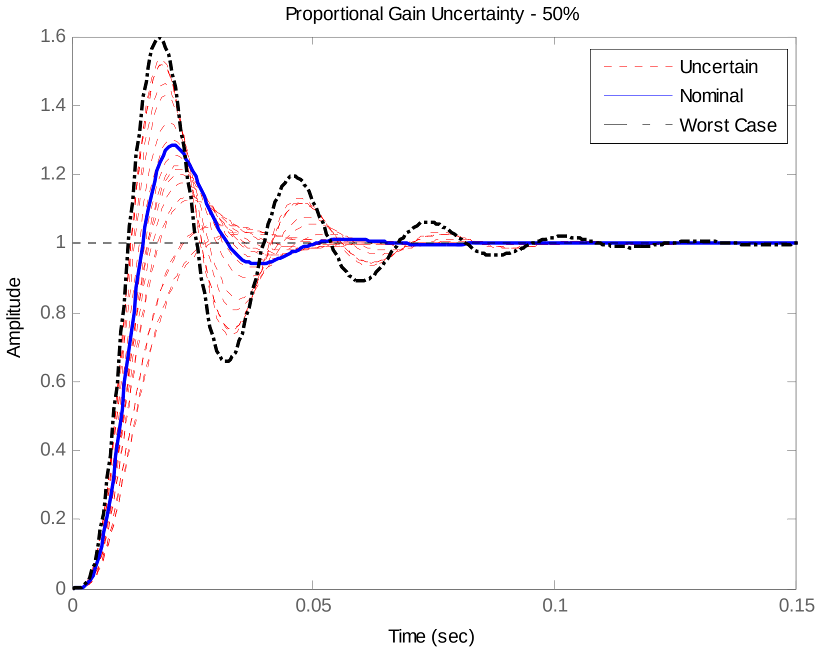

Figure 4.10 Plant Step Displacement Responses with Proportional Gain Uncertainty

Non-parametric uncertainties can also be modeled in a similar manner. A LTI system *B(s)* can first be constructed and its norm is within a specified bound γ.

$$\|B(s)\| \le \gamma \tag{4.7}$$

Frequency domain product of the nominal system $G_{nom}(s)$ and *B(s)* thus characterizes the uncertainty transfer function. The upper and lower bounds of the uncertain system are defined in equation (4.8). Sample uncertain realizations can be assumed anywhere between the selected bounds.

$$G_B(s) = G_{nom}(s) \cdot [I(s) \pm B(s)] \tag{4.8}$$

As an example, a 1st order uncertain transfer function is assumed that has a DC gain |*B(0)*|=0.01, a crossover frequency at 100Hz where |*B(100)*|=1 and a high frequency gain of |*B(inf)*|=1.5. The selection of this example is realistic for a typical physical system that has smaller uncertainty at lower frequency, but the uncertainty grows as the frequency increases. Both the nominal system and the uncertain system transfer function bounds are shown in Figure 4.11. It is observed the nominal system magnitude and phase lie in between the lower and upper bounds, as expected. Similarly, time domain step displacement responses are shown in Figure 4.12. Undesirable larger overshoot is observed as the uncertain system approaches the upper bound, but with a reduced rise time. Oppositely, smaller overshoot but increased rise time is observed as the uncertain system approaches the lower bound.

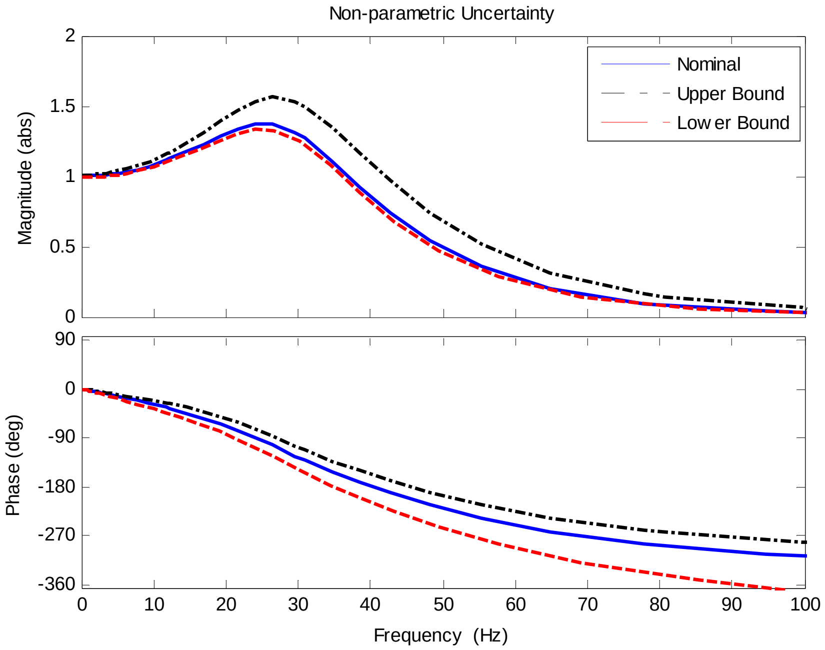

Figure 4.11 Plant Transfer Function Realizations with Non-parametric Uncertainty

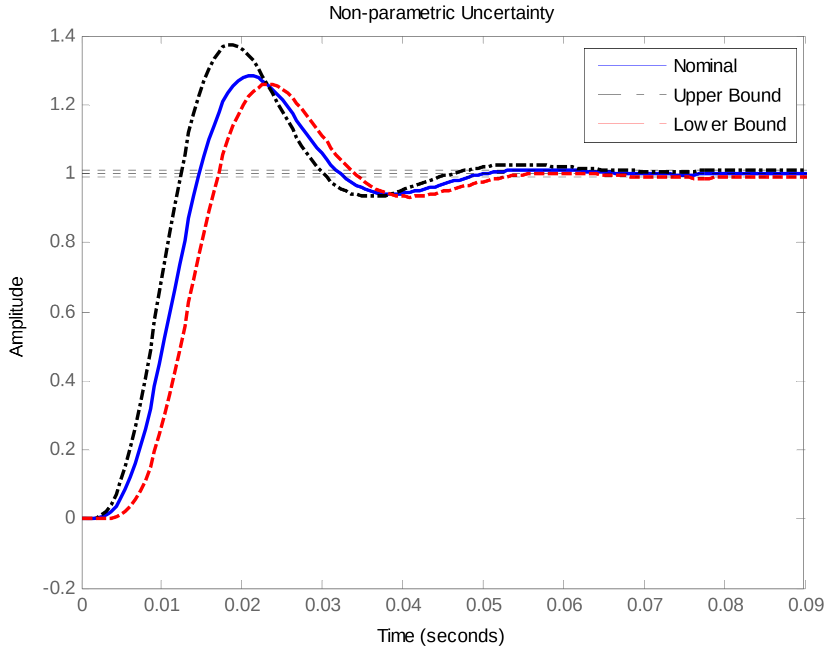

Figure 4.12 Plant Step Displacement Responses with Non-parametric Uncertainty

It can be concluded that a less aggressive proportional gain is preferred for increased stability margin, especially when the plant dynamics show significant amount of uncertainty. But the trade-off is the increased phase lag and/or rise time that means significant tracking error. The analysis in this section demonstrates the limitation of the PID control strategy in its ability to achieve both the magnitude and the phase tracking requirement. Large parametric and/or non-parametric uncertainties can have a significant influence on the inner-loop PID control system dynamics. More advanced control strategies are therefore necessary that will potentially work not only with the nominal plant, but also the system with uncertainties.

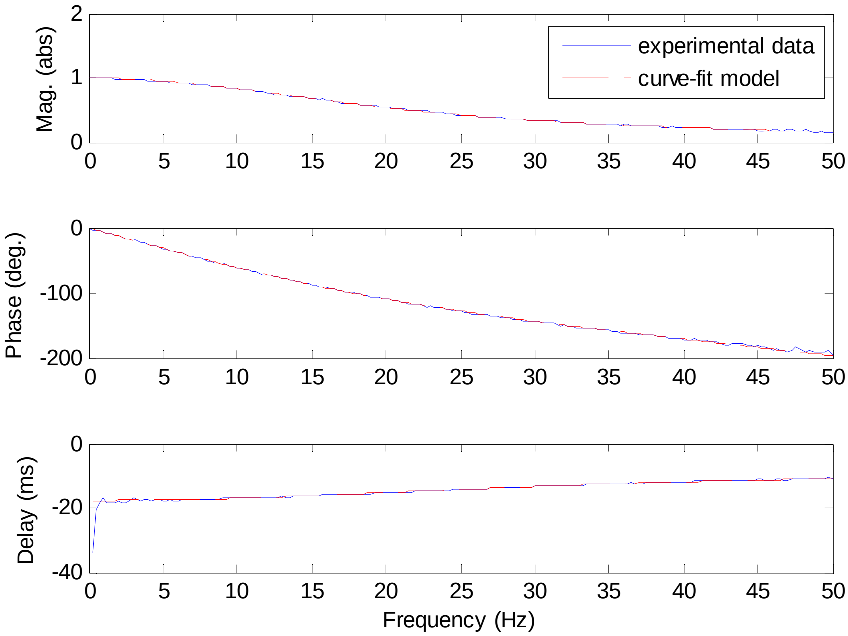

Figure 4.13 Plant Experimental Transfer Function with the Spring Specimen

To verify the analysis procedure above, actuator tracking performance is experimentally evaluated using the setup shown in Figure 4.2. The SC6000 controller is used instead of the 5910 controller for this test, with the nominal proportional gain set to be 7. The plant transfer function is obtained using a white noise RMS amplitude of 0.02” (0.05 cm) and a frequency bandwidth of 0-100 Hz. The plant transfer function is identified through a curve-fitting procedure that is shown in Figure 4.13. A tracking experiment is subsequently conducted using a chirp as the command displacement at a 0.3” (0.76 cm) amplitude and a frequency bandwidth of 0-10 Hz. Control and data acquisition are conducted at a sampling frequency of 5120 Hz.

The measured displacement in Figure 4.14 shows both an amplitude roll-off and a phase delay compared to the command displacement. This observation coincides with the frequency domain experimental observation in Figure 4.13. The tracking error grows larger as the command signal frequency increases. The displacement x-y plot on the bottom left subplot in Figure 4.14 (a) shows a strong hysteresis (instead of a straight 45 degree line for an ideal tracking), which indicates significant phase error. The normalized RMS displacement tracking error for the entire time history is calculated in equation (4.9) to be 56.43%. More experiments will be conducted in the next chapters to compare the tracking performance using various outer-loop controllers.

$$E_T = \sqrt{\frac{\frac{1}{N}\sum_{i=1}^{N}(x_{c,i} - x_{m,i})^2}{\frac{1}{N}\sum_{i=1}^{N}(x_{c,i})^2}} \times 100\% \tag{4.9}$$

The result in Figure 4.14 shows more than 10 milli-second delay both from the frequency and the time domain. This observation is far from acceptable for the RTHS stability limit illustrated in Chapter 7.

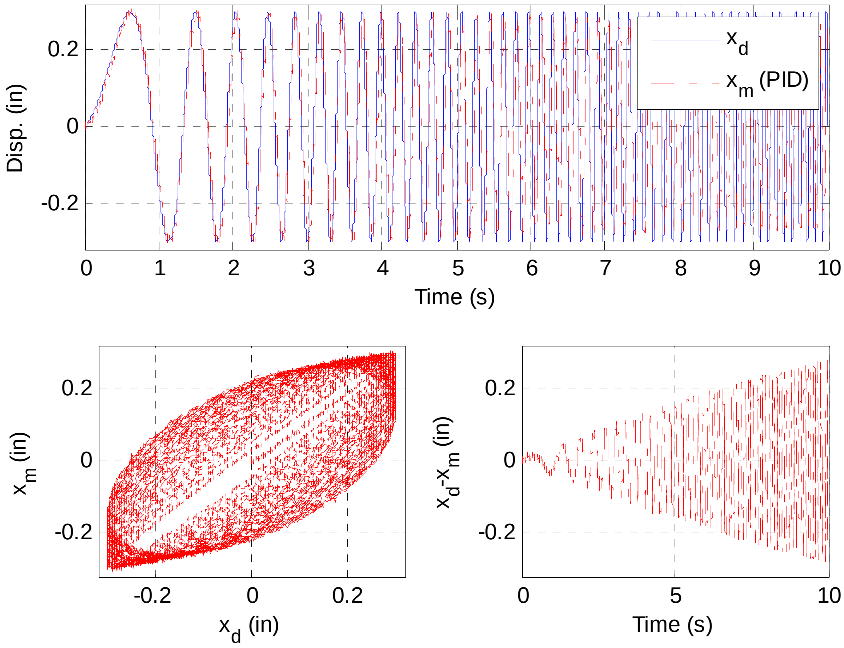

(a)

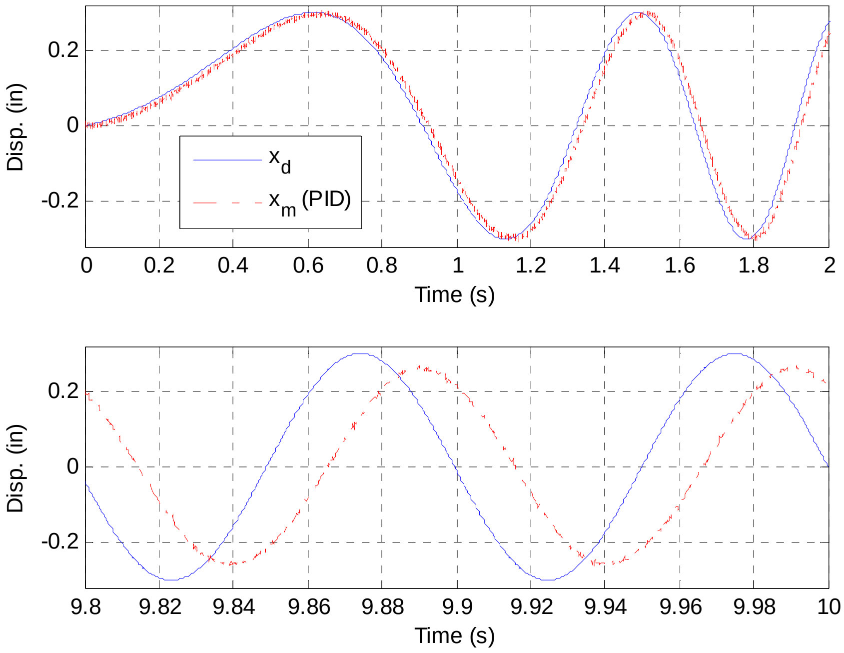

(b)

Figure 4.14 Actuator Tracking Experiment with the Spring Specimen (PID Controller)

It is concluded therefore that the simple PID control strategy is not adequate for the stringent RTHS requirement. More advanced control strategies are therefore implemented and evaluated in the following chapters.

4.3 Summary

A classical servo-hydraulic actuator and control system model is adopted in this chapter. Both parametric and non-parametric uncertainty modeling techniques are introduced to represent the physical system nonlinearities and dynamic variations, in additional to the nominal LTI plant model. A parametric study is then conducted to understand the sensitivity of the plant dynamics with respect to several key parameters. A frequency dependent uncertainty function is introduced too as a simplified approach to characterize the complex non-parametric dynamics. The understanding of the plant uncertainty is useful not only to model and analyze the system, but also to improve the outer-loop controller design. The PID control strategy is demonstrated to be ineffective through both simulation and experiment. This chapter motivates to propose more advanced adaptive and robust strategies that are intended not only to control the nominal system, but also system with uncertainties.

CHAPTER 5
MODEL REFERENCE ADAPTIVE CONTROL OF ACTUATOR

The assumption of a linear time invariant (LTI) system is by all means a fundamental basis to model a dynamical system. This assumption facilitates many of the classical and modern control theory development. Although considerable achievements have been made within the scope of linear control theory, it is a keen interest of both academia and industry to further explore more advanced mathematical tools to improve the controller performance. Adaptive control is one area that has attracted much attention for many decades [(Landau, 1979), (Narendra & Annaswamy, 1989), (Slotine & Li, 1991), (Ioannou & Sun, 1996)]. The adaptive design strategies can vary distinctively for each specific formulation. However, the common philosophy behind adaptive control is to have a mechanism to automatically detect the plant dynamics variation, so that online controller adjustment can be made to accommodate the changes. An adaptation law is a unique component for adaptive control design, in addition to the associated control law. An adaptive controller is normally nonlinear due to the existence of this adaptation law, which can be interpreted as an online dynamic observer/estimator.

The servo-hydraulic actuation and control system is studied exclusively in Chapter 4 where uncertainties are modeled and analyzed. A generalized model reference adaptive control (MRAC) strategy is introduced in this chapter that is suitable for plant with parametric uncertainties. The basic MRAC design philosophy is to introduce feedback control and adaptation mechanisms to the plant so that the closed-loop system can match the reference system. Therefore the controlled plant output can follow the reference output, at least asymptotically. Some mathematical definitions and lemmas are introduced first to facilitate the understanding of the MRAC controller design. Control and adaptation laws design are presented in the following sections, where the plant formulation is assumed with increased complexity. Finally the MRAC is implemented and evaluated experimentally about its performance to control the motion of the servo-hydraulic actuator.

5.1 Mathematical Preliminaries

The concept of a positive real system is important in the analysis and design of many nonlinear control problems (Narendra & Annaswamy, 1989). A positive real (PR) transfer function $H(p)$ is defined for a linear system as:

$$\mathrm{Re}[H(p)] \geq 0 \quad \text{for all} \quad \mathrm{Re}[p] \geq 0 \tag{5.1}$$

Furthermore, the transfer function is strictly positive real (SPR) if the system $H(p-\varepsilon)$ is positive real for some $\varepsilon>0$. Herein in this chapter we adopt the notation 'p' being the Laplace variable that is more widely accepted in the adaptive control literature. The purpose is to make a distinction with the standard variable 's' to avoid confusion due to the commonly mixed use of time and frequency domain notations.

The Kalman-Yakubovich Lemma is an important mathematical tool that is associated with a SPR system's state space representation. The lemma is introduced here to facilitate the construction of a Lyapunov function. A globally stable adaptation law can therefore be synthesized through this Lyapunov function. Consider a controllable LTI system:

$$\begin{aligned} \dot{x} &= Ax + Bu \\ y &= C^T x \end{aligned} \tag{5.2}$$

The transfer function $H(s) = C^T(sI - A)^{-1}B$ is SPR if and only if there exist positive definite matrices P and Q such that

$$\begin{aligned} A^T P + PA &= -Q \\ PB &= C \end{aligned} \tag{5.3}$$

Another lemma is introduced to synthesize the adaptation laws for the MRAC design in the next section. Consider two signals e and ϕ related by the following dynamic equation:

$$e(t) = H(p)[k\phi^T(t)v(t)] \tag{5.4}$$

where *e(t)* is a scalar output signal, *H(p)* is a SPR transfer function, *k* is an unknown constant with known sign, *ϕ(t)* is a $m \times 1$ vector function of time, and *v(t)* is a measureable $m \times 1$ vector. If the vector ϕ varies according to

$$\dot{\phi}(t) = -\operatorname{sgn}(k)\gamma e v(t) \tag{5.5}$$

with γ being a positive constant, then *e(t)* and *ϕ(t)* are globally bounded. Furthermore, if v is bounded, then $e(t) \to 0$ as $t \to \infty$. Here *e(t)* is the output of the SPR transfer function *H(p)* subjected to input $[k\phi^T(t)v(t)]$. The physical interpretation of the above lemma is that if the input signal *ϕ(t)* for a SPR system *H(p)* in equation (5.4) depends on the output *e(t)* in the form of equation (5.5), then the overall feedback system is globally stable. A schematic view of a global stable adaptive system is shown in Figure 5.1.

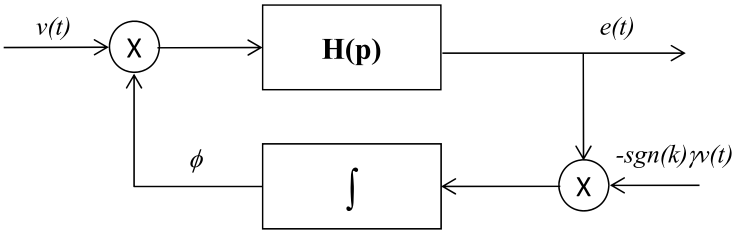

Figure 5.1 Global Stable Adaptive System

The above adaptive law synthesis Lemma is fundamental to the derivation of the MRAC design in the next section. The proof of the lemma is straightforward by constructing a Lyapunov function. Assume the state-space representation of equation (5.4) being:

$$\begin{aligned} \dot{x} &= Ax + B[k\phi^T v] \\ e &= C^T x \end{aligned} \tag{5.6}$$

By selecting a positive definite Lyapunov function *V* of the form:

$$V(x,\phi) = x^T P x + \frac{|k|}{\gamma}\phi^T \phi \tag{5.7}$$

Its time derivative is evaluated by applying equation (5.3), (5.5) and (5.6).

$$\dot{V}(x,\phi) = x^T(PA + A^T P)x + 2x^T PB(k\phi^T v) - 2\phi^T PB(kev) = -x^T Qx \le 0 \tag{5.8}$$

It can be seen that the derivative in equation (5.8) is non-negative semi-definite so that the system defined by equations (5.4) and (5.5) is globally stable. The equations (5.7) and (5.8) also imply that *e(t)* and *ϕ(t)* are globally bounded.

5.2 MRAC Formulation

The MRAC formulation in this section was originally presented in (Narendra & Annaswamy, 1989) and (Slotine & Li, 1991). Only important definitions and derivations are included herein to facilitate the understanding of the control design. A schematic view of a simplest model-reference adaptive control system is shown in Figure 5.2. The MRAC system is composed of four main components: a plant contains known system structure but unknown parameters; a reference model specifies the desired output y_m of the control system; a feedback control law contains adjustable parameters; and an adaptation law to update the adjustable control parameters.

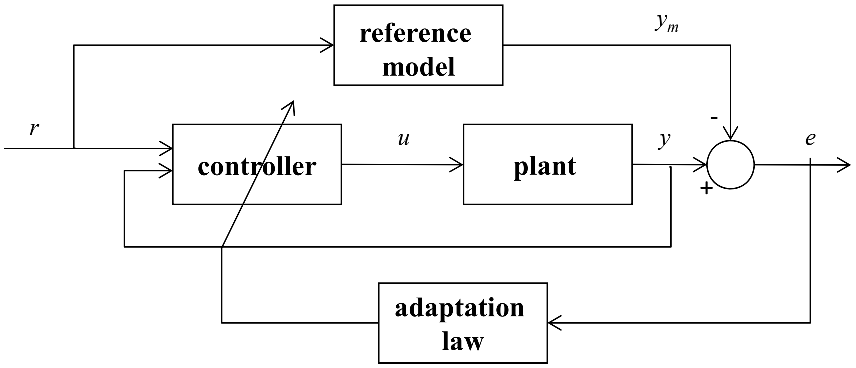

Figure 5.2 First-order Plant MRAC Formulation

The plant and reference models are restricted to be LTI system within the scope of this text, where the number of poles and zeros depend on the intended control application. Although a higher order plant is generally desirable for better modeling accuracy over broader frequency ranges, the control and adaptation laws can become very mathematically involved to design. The reference model defines the control performance specifications such as rise time, settling time and overshoot etc. However, the reference system formulation needs to be restricted to ensure that a perfect tracking can be achievable, given the plant parameters are known a priori. For a more realistic application when plant parameters are unknown, the adaptation mechanism will adjust controller parameters so that a perfect tracking is asymptotically achievable. In a MRAC system, the adaptation law searchers for control parameters such that the closed-loop plant response y converge to the reference output y_m, when subjected to the reference input r.

The simplest MRAC formulation assumes that both the reference model and the plant can be approximated by first-order dynamical systems. The plant is assumed to be

$$\dot{y} = -a_p y + b_p u \tag{5.9}$$

where the plant parameters a_p and b_p are assumed to be unknown. A reference model is

$$\dot{y}_m = -a_m y_m + b_m r \tag{5.10}$$

The control law is chosen to be

$$u = \hat{a}_r(t) r + \hat{a}_y(t) y \tag{5.11}$$

so that it can enable a perfect model match, if the plant initial parameters ($a_{p,0}, b_{p,0}$) are invariant and known in advance. The ideal control parameters that allows this perfect tracking are $a_r^* = b_m / b_{p,0}$ $a_y^* = (a_{p,0} - a_m) / b_{p,0}$.

The time derivative of the tracking error is evaluated through equations (5.9) to (5.11).

$$\begin{aligned} \dot{e} = \dot{y} - \dot{y}_m &= -a_m(y - y_m) + (a_m - a_p + \hat{a}_y b_p) y + (\hat{a}_r b_p - b_m) r \\ &= -a_m e + b_p(\tilde{a}_r r + \tilde{a}_y y) \end{aligned} \tag{5.12}$$

where the parameter estimation errors are the difference between the controller parameters and the ideal parameters.

$$\begin{aligned} \tilde{a}_r &= \hat{a}_r - a_r^* = \hat{a}_r - \frac{b_m}{b_{p,0}} \\ \tilde{a}_y &= \hat{a}_y - a_y^* = \hat{a}_y - \frac{a_{p,0} - a_m}{b_{p,0}} \end{aligned} \tag{5.13}$$

The error in equation (5.12) can then be written in the form of equation (5.4) as

$$e = \frac{b_p}{p + a_m}\left(\tilde{a}_r r + \tilde{a}_y y\right) \tag{5.14}$$

According to equations (5.5), the adaptation law for a global stable closed-loop system is

$$\begin{aligned} \dot{\hat{a}}_r &= \dot{\tilde{a}}_r = -\operatorname{sgn}(b_p)\gamma e r \\ \dot{\hat{a}}_y &= \dot{\tilde{a}}_y = -\operatorname{sgn}(b_p)\gamma e y \end{aligned} \tag{5.15}$$

where γ being a positive constant representing the adaptation gain. The direction of the search for the proper controller parameters is determined by $\operatorname{sgn}(b_p)$.

Considerable challenges arise when trying to generalize the MRAC formulation to a higher order plant, especially when full state feedback measurements are not available. Both the plant and the reference models take generalized representations in equation (5.16)

$$\begin{aligned} W(p) &= k_p \frac{Z_p(p)}{R_p(p)} = k_p \frac{b_o + b_1 p + \ldots + b_{m-1} p^{m-1} + p^m}{a_o + a_1 p + \ldots + a_{n-1} p^{n-1} + p^n} \\ W_m(p) &= k_m \frac{Z_m(p)}{R_m(p)} \end{aligned} \tag{5.16}$$

where Z_m and R_m are monic Hurwitz polynomials of degree m_m and n_m, respectively. The relative degree of the reference model has to be larger than or equal to the plant (i.e. $n_m - m_m \geq n - m$) to allow the possibility of a perfect model match.

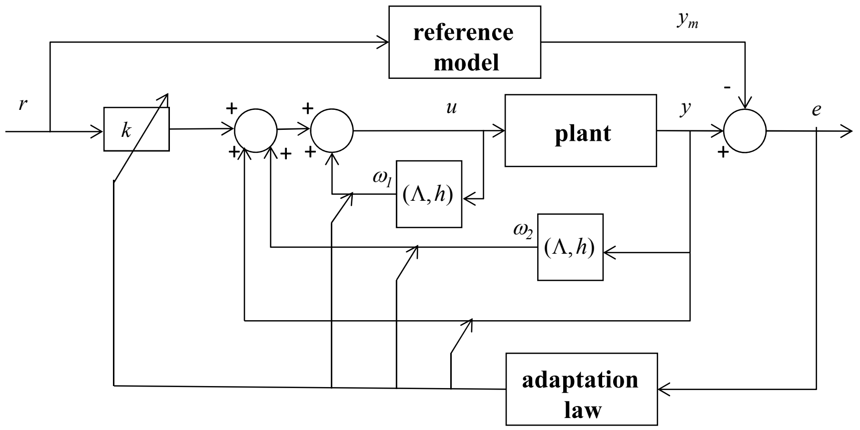

Figure 5.3 Generalized MRAC Formulation

A generalized MRAC formulation is schematically shown in Figure 5.3, when the plant model is not limited to a first-order system. Different from the simple algebraic control law in equation (5.11) for a first-order plant, it is now necessary to introduce dynamics into the control law synthesis since the output provides only partial information about the system states. The control law of the generalized MRAC design is

$$u(t) = \theta(t)^T \omega(t) \tag{5.17}$$

where $\theta(t) = [k(t) \quad \theta_1(t) \quad \theta_2(t) \quad \theta_0(t)]^T$ is a $2n \times 1$ vector containing all online updated controller parameters, and $\omega(t) = [r(t) \quad \omega_1(t) \quad \omega_2(t) \quad y(t)]^T$ contains the corresponding measurable signals. Dynamic variables are introduced into the control law synthesis.

$$\begin{aligned} \dot{\omega}_1(t) &= \Lambda \omega_1 + hu \\ \dot{\omega}_2(t) &= \Lambda \omega_2 + hy \end{aligned} \tag{5.18}$$

where the total states is $n-1$ and the system (Λ, h) is controllable. The parameter estimation errors are determined by subtracting the ideal parameters from the estimated parameters as

$$\tilde{\theta}(t) = \theta(t) - \theta^* \tag{5.19}$$

The tracking error is related to the parameter error by the following equation

$$e(t) = W_m(p)[\tilde{\theta}^T(t)\omega(t)/k^*] \tag{5.20}$$

If the plant has unity relative degree such that a SPR reference system can be constructed, a similar adaptation law as described in equation (5.15) can be derived in (5.21).

$$\dot{\theta} = -\operatorname{sgn}(k_p)\gamma e(t)\omega(t) \tag{5.21}$$

Otherwise, when the relative degree of the plant is larger than one, the reference model cannot be SPR so that an augmented error needs to be defined:

$$\varepsilon(t) = e(t) + \alpha(t)\{\tilde{\theta}^T W_m[\omega] - W_m[\tilde{\theta}^T\omega]\} \tag{5.22}$$

Adaptation laws are obtained to update the controller parameters *Θ(t)* and the parameter *α(t)* that forms the augmented error, according to the follow equation

$$\begin{aligned} \dot{\theta}(t) &= -\frac{\operatorname{sgn}(k_p)\gamma\varepsilon\overline{\omega}}{1+\overline{\omega}^T\overline{\omega}} \\ \dot{\alpha}(t) &= -\frac{\gamma\varepsilon\eta}{1+\overline{\omega}^T\overline{\omega}} \end{aligned} \tag{5.23}$$

where $\eta(t) = \theta^T W_m(p)[\omega] - W_m(p)[\theta^T\omega]$ is the auxiliary error and $\overline{\omega}(t) = W_m(p)[\omega]$. It is observed that although the control law in equation (5.17) is linearly parameterized in terms of the controller parameters, the existence of the adaptation law in equation (5.23) makes the MRAC a nonlinear control design. The global convergence of the tracking error can be demonstrated. However, the proof is mathematically involved that is beyond the scope of this study.

5.3 MRAC Control of Hydraulic Actuator

Both experimental and simulation studies in Chapter 4 reveal that the uncertainties inevitably exist for complex physical system components. The MRAC algorithm is implemented in this Chapter as an attempt to achieve a robust tracking performance. The minimal control synthesis adaptive design in [(Bonnet, et al., 2007), (Lim, Neild, Stoten, Drury, & Taylor, 2007)] assume a first-order plant transfer function. However, a higher-order assumption is expected to capture the plant dynamics better. Therefore, both the plant and reference models in this section assume two poles and no zeros i.e. $n=n_m=2$ and $m=m_m=0$. The motivation to choose this assumption is also that the structural mass, damping and stiffness description is intrinsically a 2nd order dynamical system. As discussed in the previous section, the MRAC design becomes more challenging for this higher order plant because only the output feedback is available, instead of the full state feedback. Moreover, the plant and reference model assumption herein are not SPR, so that the more generalized MRAC control law in equation (5.17) and the adaptive law in equation (5.23) are used for the design.

In our application of actuator motion control, the input r in Figure 5.3 is the desired displacement trajectory and the output y_m is the best achievable actuator output displacement. The reference model is designed to have a maximal flat unity amplitude and a minimal phase lag, over the desired tracking performance bandwidth. In the MRAC design, the reference model poles are placed far away from the complex plane origin to ensure small phase lag. Appropriate damping ratios are designed for each system pole to enable a maximal flat amplitude response. Since the reference model governs the tracking performance specification, it is important to design it properly for a realistic physical implementation. Although an aggressive reference model design can achieve a small rise time, it is likely to reduce the system stability margin. The reason is that the physical plant may not be characterized completely by a 2nd order dynamical model. The experimental implementation in this study designs the reference model as

$$y_m = \frac{k_m}{p^2 + a_{m1}p + a_{m2}} r = \frac{2.47e6}{p^2 + 2.36e3p + 2.47e6} r \tag{5.24}$$

The plant model is obtained by curve-fitting the experimental transfer function that is shown in Figure 4.13.

$$y = \frac{k_p}{p^2 + a_{p1}p + a_{p2}} u = \frac{1.44e4}{p^2 + 2.22e2p + 1.44e4} u \tag{5.25}$$

The dynamics within the control law synthesize is designed as

$$\begin{aligned} \omega_1 &= \frac{1}{(p+\lambda_0)} u = \frac{1}{(p+5)} u \\ \omega_2 &= \frac{1}{(p+5)} y \end{aligned} \tag{5.26}$$

Initial control parameters are calculated below that allows a perfect model match, if equation (5.25) can describe the plant perfectly.

$$\begin{aligned} &k(0) = k_m / k_p = 171.85 \\ &\theta_1(0) = a_{p1} - a_{m1} = -2.13e3 \\ &\theta_2(0) = \{[(\lambda_0 - a_{p1} + a_{m1})a_{p2} - a_{m2}\lambda_0] - \lambda_0[(\lambda_0 - a_{p1} + a_{m1})a_{p1} \\ &\qquad + a_{p2} - a_{m2} - a_{m1}\lambda_0]\} / k_p = 1.97e3 \\ &\theta_0(0) = [(\lambda_0 - a_{p1} + a_{m1})a_{p1} + a_{p2} - a_{m2} - a_{m1}\lambda_0] / k_p = -138.58 \end{aligned}$$

A unity-gain, low-pass filter is designed to eliminate the high-frequency measurement noise effect, before the command is sent to the physical servo-controller. The filter design herein assumes the same amount of poles and zeros to keep the number of relative degree unchanged for the plant.

$$F(s) = \frac{s^2 + 5.62e2s + 7.89e4}{20s^2 + 1.26e3s + 7.89e4} \tag{5.27}$$

An implementation of the MRAC design in SIMULINK is shown in Figure 5.4.

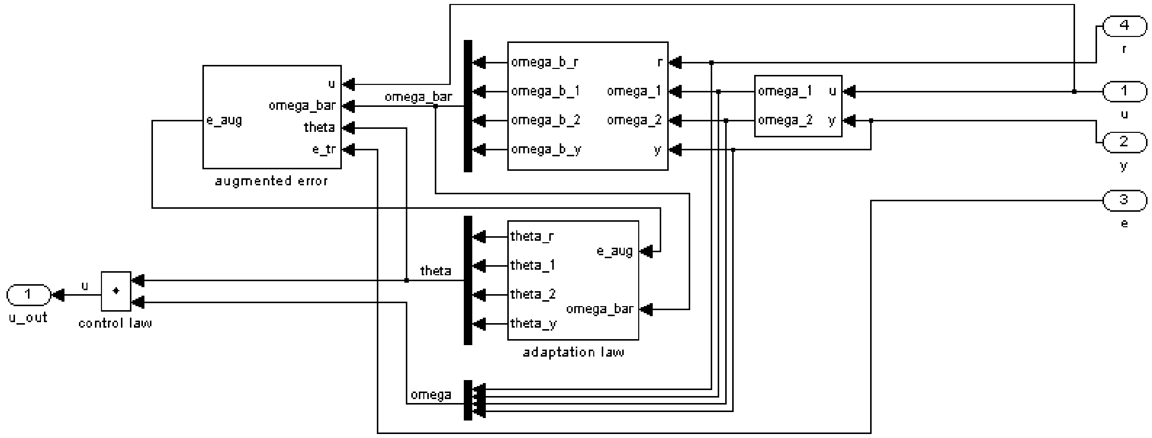

Figure 5.4 SIMULINK Implementation of MRAC

The tracking experiment is conducted again on the spring specimen discussed in Chapter 4, plus the outer-loop MRAC controller to evaluate the actuator tracking performance. Control and data acquisition are conducted at a sampling frequency of 5120 Hz. Experimental data are compared with the ones obtained using the PID controller and the results are shown in Figure 5.5. It is obvious that the MRAC can largely improve both the amplitude and phase responses, especially at the higher frequency range in Figure 5.5 (b) where the phase lag is reduced by more than half. The normalized tracking error for the whole time history is reduced to 20.26% compared to 56.43%, when only the inner-loop PID controller is used. The improvement can also be observed in the displacement x-y plot on the bottom left subplot of Figure 5.5 (a), which shows reduced hysteresis.

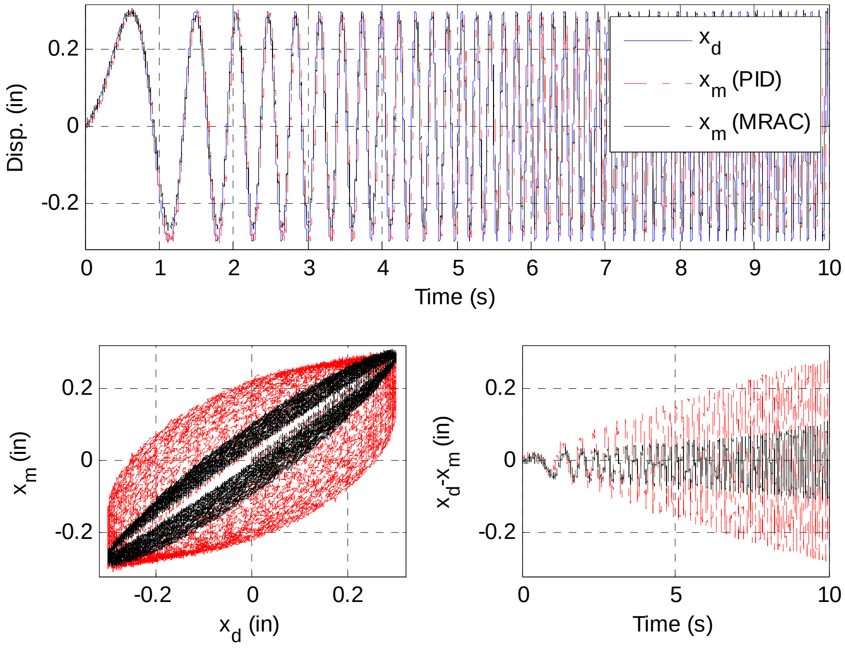

(a)

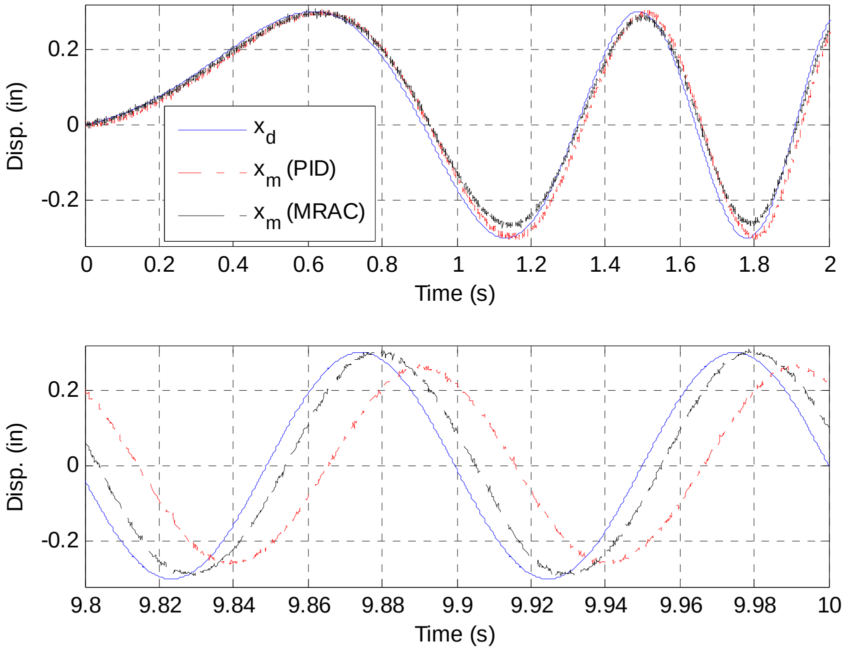

(b)

Figure 5.5 Actuator Tracking Experiment with the Spring Specimen (MRAC Controller)

Theoretically, the above MRAC design works best when the plant formulation is perfect (e.g. the 2nd order model used in this design), but only the individual parameters can vary. Depending on the test specimen and the intensity of control structure interaction, the physical plant dynamics may deviate largely from the assumed model formulation. The global stability and convergence of the tracking error are therefore not guaranteed for the closed-loop system. In this controller formulation, the tracking error between the desired displacement r and the measured displacement y are contributed from two main sources. 1) the error between the reference output y_m and the desired displacement r since the reference model cannot be a perfect unity-gain, zero-phase system; 2) the error e between the reference output y_m and the physical actuator displacement y.

5.4 Summary

A generalized MRAC design strategy is introduced and implemented to control the motion of the physical actuator with a spring specimen. The MRAC tracking performance improvement is demonstrated experimentally by comparing with the PID control. Although it may be adequate for some RTHS applications, a nearly 5 ms delay is observed using the MRAC that is still too large for the experiments planned in Chapter 7. One way to improve the tracking performance is to design a more aggressive reference model. However, the global stability becomes a concern when the physical plant dynamics is deviated from the assumed model formulation. The above presented MRAC theory is developed only to deal with the plant parametric uncertainty, but not non-parametric uncertainty. Another disadvantage is that the algorithm is not straight forward to expand to multivariable control applications. It is therefore desirable to have a control strategy that can accommodate both parametric and non-parametric plant uncertainties. Ideally the controller should also be applicable to generalized RTHS implementations that engage multiple actuators. The H_∞ loop shaping robust optimal control strategy is therefore proposed and tested in the next chapters.

CHAPTER 6
ROBUST H_∞ LOOP SHAPING CONTROL OF ACTUATOR

The modeling of a physical system for feedback control inevitably involves imperfections. Even a sophisticated model may not be able to reproduce perfectly the physical plant dynamics, which are normally complex and nonlinear. Assuming the nominal plant transfer function is known, we can define the transfer functions of a set of ‘close’ systems. The motivation of this chapter is to introduce a robust controller design strategy that can stabilize not only the nominal plant, but a class of systems that are ‘close’ to the nominal model. The theory of H_∞ optimal control is briefly introduced first, based on which a loop shaping design strategy is developed. The controller design is then analyzed both through simulation and experiment to evaluate its effectiveness to control the motion of hydraulic actuator.

6.1 H_∞ Optimal Control Preliminaries

Some mathematical notations and definitions are introduced in this section to facilitate the understanding of the H_∞ control theory formulations. Only important definitions and theorems are included in this section to facilitate the understanding of the control design. Interested readers are encouraged to consult relevant references [(Glover & McFarlane, 1989), (McFarlane & Glover, 1990), (McFarlane & Glover, 1992), (Zhou & Doyle, 1998)] for more rigorous proof of the theorems and in depth theory development, which is beyond the scope of this dissertation.

The L_∞ / H_∞ norm of a dynamical system *G* is given

$$\|G\|_\infty \equiv \sup \bar{\sigma}[G(j\omega)] \tag{6.1}$$

where RH_∞ denotes the space of all real-rational transfer function matrices that have no pole in the right half complex plane i.e. $\mathrm{Re}(s) > 0$. Here $\bar{\sigma}(\bullet)$ denotes the maximum singular value of *G*.

Suppose $\tilde{M}, \tilde{N} \in RH_\infty$ have the same number of rows, the pair $(\tilde{N}, \tilde{M})$ constitutes a left coprime factorization (LCF) of $G \in R$ if and only if:

(a) $\tilde{M}$ is square, $\det(\tilde{M}) \neq 0$

(b) $G = \tilde{M}^{-1}\tilde{N}$

(c) $\tilde{N}$ and $\tilde{M}$ are left coprime.(i.e. there exist $U, V \in RH_\infty$ such that $\tilde{M}V + \tilde{N}U = I$)

A normalized left coprime factorization of a nominal plant *G* is a LCF $(\tilde{N}, \tilde{M})$ of *G* that satisfies

$$\tilde{M}\tilde{M}^* + \tilde{N}\tilde{N}^* = I \tag{6.2}$$

for all $s \in jR$ (the imaginary axis of the complex plane), where $(^*)$ denotes the complex conjugate transpose of a matrix.

Let $G = \left[\begin{array}{c|c} A & B \\ \hline C & D \end{array}\right]$ be a minimal state-space realization. A normalized LCF factorization (Vidyasagar, 1988) of *G* can be represented as

$$\left[\widetilde{N}, \widetilde{M}\right] \equiv \left[\begin{array}{c|cc} A + HC & B + HD & H \\ \hline R^{-1/2}C & R^{-1/2}D & R^{-1/2} \end{array}\right] \tag{6.3}$$

where $R = I + DD^*$, $H \equiv -(ZC^* + BD^*)R^{-1}$ and *Z* is the unique, positive definite solution to the generalized filtering algebraic Riccati equation (GFARE):

$$\begin{aligned} &\left(A - BD^*R^{-1}C\right)Z + Z\left(A - BD^*R^{-1}C\right)^* - ZC^*R^{-1}CZ + \\ &B\left(I - D^*R^{-1}D\right)B^* = 0 \end{aligned} \tag{6.4}$$

Assume *G* is the nominal plant transfer function that is written as $G = \widetilde{M}^{-1}\widetilde{N}$ where $\widetilde{M}$, $\widetilde{N}$ are stable transfer functions representing a LCF of *G*. We can define the transfer function of a set of 'close' systems by $G_\Delta = (\widetilde{M} + \Delta_M)^{-1}(\widetilde{N} + \Delta_N)$ where Δ_M, Δ_N represent stable unknown transfer functions (i.e. plant model uncertainties) that is bounded and satisfying $\left\|\left[\Delta_N, \Delta_M\right]\right\|_\infty < \varepsilon$. Herein a perturbation class associated with a normalized coprime factor uncertainty is defined as:

$$\Omega_\varepsilon \equiv \left\{\Delta = [\Delta_N, \Delta_M]; \Delta \in RH_\infty^{p\times(m+p)}; \|\Delta\|_\infty < \varepsilon\right\} \tag{6.5}$$

where the nominal system *G* is assumed to have the input-output dimension of $p \times m$ and ε is the uncertainty bound. A schematic view of the H_∞ optimization problem is shown in Figure 6.1. The design objective is to obtain an optimal controller *K* that can stabilize not only the nominal plant *G*, but a class of uncertain systems G_Δ that are close to the nominal model.

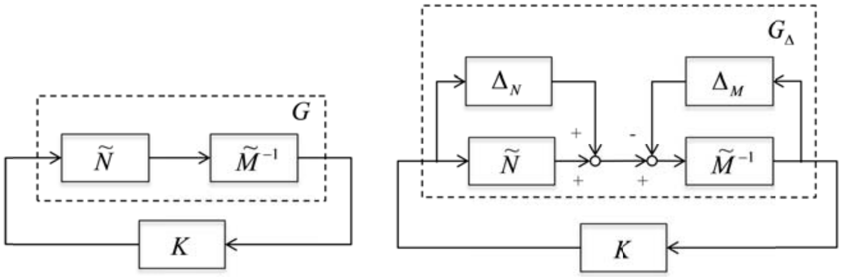

Figure 6.1 H_∞ Optimal Control Problem Formulation

Let $(\widetilde{N}, \widetilde{M})$ be a normalized LCF of *G*. Then, the largest positive number $\varepsilon = \varepsilon_{\max}$ such that $G_\Delta = (\widetilde{M} + \Delta_M)^{-1}(\widetilde{N} + \Delta_N)$ can be stabilized by a single controller *K* chosen over all stabilizing controllers for all $\Delta \in \Omega_\varepsilon$ is given by:

$$\varepsilon_{\max} = \left(\inf_K \left\| \begin{bmatrix} K \\ I \end{bmatrix} (I - GK)^{-1} \widetilde{M}^{-1} \right\|_\infty \right)^{-1} \tag{6.6}$$

By selecting the normalized LCF representation, the solution to the robust stabilization problem can be obtained explicitly without iteration. Optimal solutions to the normalized LCF problem give the maximum stability margin

$$\varepsilon_{\max} = \{1 - \left\| \widetilde{N}, \widetilde{M} \right\|_H^2 \}^{1/2} > 0 \tag{6.7}$$

where the Hankel Norm, denoted $\|\bullet\|_H$ is the maximum Hankel singular value which is defined as the square root of the eigenvalues for the product of the system controllability Gramian and the observability Gramian.

A sub-optimal controller of a particular solution for the normalized LCF robust stabilization problem is to obtain the stabilizing controller *K* such that

$$\left\| \begin{bmatrix} K \\ I \end{bmatrix} (I - GK)^{-1} \widetilde{M}^{-1} \right\|_{\infty} \leq \gamma \tag{6.8}$$

where $\gamma > \varepsilon_{\max}{}^{-1}$ is a pre-specified tolerance level for the allowable uncertainty. A particular representation called the central or maximum entropy controller in [(Glover & McFarlane, 1989), (McFarlane & Glover, 1990)]. The controller is formulated as

$$K = \left[\begin{array}{c|c} A^c + \gamma^2 W_1^{*-1} Z C^* (C + DF) & \gamma^2 W_1^{*-1} Z C^* \\ \hline B^* X & -D^* \end{array} \right] \tag{6.9}$$

The generalized control algebraic Riccati equation (GCARE) is solved to obtain X in additional to Z obtained in equation (6.4)

$$\begin{aligned} &\left(A - BS^{-1}D^*C\right)^* X + X\left(A - BS^{-1}D^*C\right) - XBS^{-1}B^*X + \\ &C^*\left(I - D^*S^{-1}D^*\right)C^* = 0 \end{aligned} \tag{6.10}$$

where intermediate terms are defined and calculated as

$$\begin{aligned} S &= I + D^*D \\ F &= -S^{-1}\left(D^*C + B^*X\right) \\ A^c &= A + BF \\ W_1 &= I + \left(XZ - \gamma^2 I\right) \end{aligned} \tag{6.11}$$

6.2 Loop Shaping H_∞ Controller Design

Here an H_∞ loop shaping strategy [(McFarlane & Glover, 1992), (Zhou & Doyle, 1998)] is adopted and modified to control the motion of hydraulic actuator(s). A block diagram of the proposed controller formulation is depicted in Figure 6.2. Given a dynamic plant *G(s)* that contains the overall dynamics of the inner-loop servo-hydraulic control and actuation system, the design objective is to acquire a stabilizing outer-loop controller *H(s)* which facilitates the best tracking between a desired displacement trajectory x_d, calculated from the computational substructure, and the measured displacement x_m of the physical specimen. For practical reasons, a unity gain, low-pass filter $F_s(s)$ is also inserted in the feedback path. This filter is mainly needed to reduce the effect of relative large measurement noise n, where d_i and d_o are generalized input and output disturbances, respectively. The inner-loop servo-hydraulic actuation and control system is referred as the plant in this chapter, and the transfer function refers to its displacement input output relationship, unless defined otherwise.

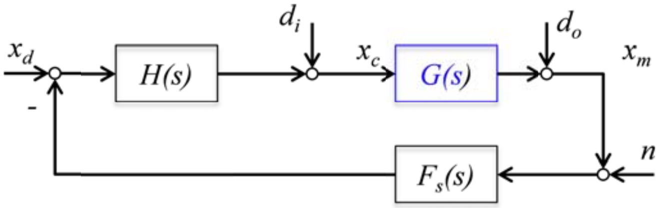

Figure 6.2 Proposed H_∞ Loop Shaping Controller Formulation

The system input-output is defined in equation (6.12) for a standard loop shaping formulation when $F_s(s)$ is temporarily not considered. The effect of $F_s(s)$ on the closed-loop system dynamics is demonstrated later in Figure 6.10. Here S_s represents the system output sensitivity regarding I/O disturbances, and T_s is the complementary sensitivity that determines the tracking performance.

$$\begin{aligned} x_m &= T_s(x_d - n) + S_s G d_i + S_s d_o \\ S_s &= (I + GH)^{-1} \\ T_s &= I - S_s = GH(I + GH)^{-1} \end{aligned} \tag{6.12}$$

It is clear from equation (6.12) that one way to achieve high performance tracking and strong disturbance rejection is to choose T_s close to unity and S_s to zero. Both goals can be achieved through shaping a large open loop gain $G(s)H(s)$ within the performance frequency range. Therefore, a closed-loop design specification is transformed into an open loop gain shaping problem. Herein, the loop gain is defined as the maximum singular value of a generalized multi-input, multi-output (MIMO) system that is equivalent to the magnitude of the transfer function in the special case of a single-input, single-output (SISO) system. A controller with unrealistic large loop gain is likely to yield instabilities due to un-modeled dynamics in the physical systems. The loop gain at higher frequencies therefore should be kept small to provide robust stability and accommodate system uncertainties. Depending on the physical plant dynamics and uncertainty level, the proposed H_∞ design philosophy is summarized as a trade-off between large loop gain for tracking performance and small loop gain for robustness.

For practical implementation, an important issue is related to the measurement noise n. Noise rejection in this design methodology is conflicted with the tracking performance requirement, which is clear in equation (6.12). High loop gain will enable noise being passed through the performance bandwidth. The relatively large actuator LVDT feedback noise present in this study could significantly deteriorates the outer-loop system performance. A numerical simulation is performed to examine the effects of this noise propagation using the identified plant model in equation (6.14) and the designed controller $H(s)$. A 0-5 Hz chirp signal at amplitude of 0.1” is used as the desired trajectory to drive the simulated outer-loop system. Three different noise levels are considered with root mean square (RMS) values of 0”, 0.001” and 0.005”, respectively. The bandwidth of the noise is chosen to be 1024 Hz to simulate broadband electronic measurement. Notice from the results shown in Figure 6.3 that even a small amount of noise can have a dramatic influence on the performance of the closed-loop control system. The H_∞ controller may magnify the broadband noise significantly and contaminate the command trajectory x_c that is sent to the plant. The measured trajectory x_m is not affected much because the plant acts as a physical low-pass filter to reduce the high frequency effects. However, this implementation is very risky in practical design because un-modeled dynamics can be excited, which is likely to induce instability issue. A filtering technique $F_s(s)$ is thus essential for practical implementations.

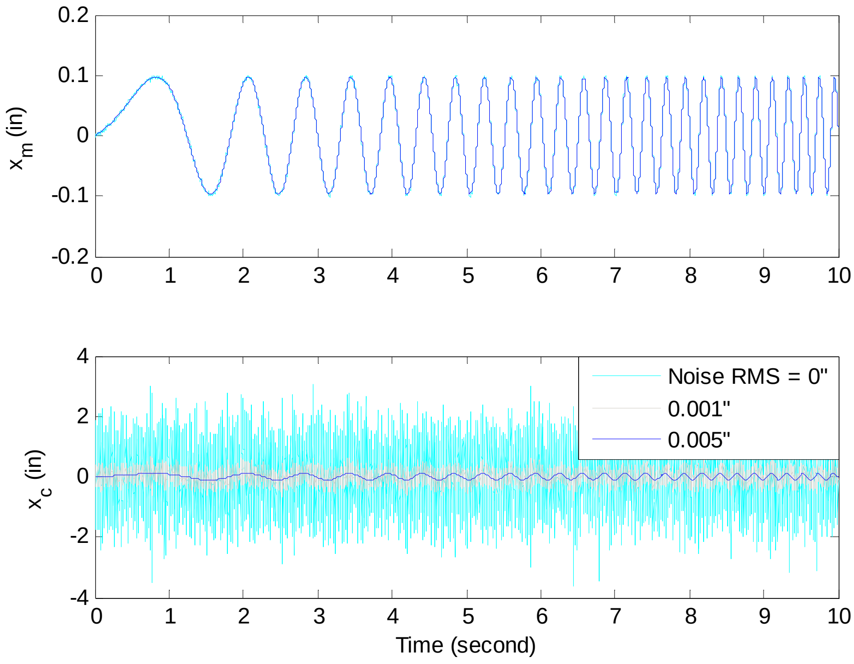

Figure 6.3 Effect of Measurement Noise on Command Signal

Another design goal to keep the controller less aggressive is to avoid input saturation. Having a large loop gain outside of the bandwidth of the plant i.e. $GH>>I$ and $G<<I$ is likely to cause actuator saturation.

Given the nominal plant $G(s)$, the proposed H_∞ loop shaping controller design is composed of four main steps:

1) The 1st step is to design a system $G_d(s)$ that specifies the target open-loop shape. The loop shape design follows the aforementioned principal to balance both the tracking performance and robustness requirements. A pre-compensator $W(s)$ is therefore calculated that satisfies $G_d(s) = G(s)W(s)$. However, $W(s)$ from this simple filter design step can be a non-causal system that is unable to be implemented physically, adding to the fact that the closed-loop robust stability is not guaranteed.
2) A 2nd design step is then to synthesize a stabilizing controller $K(s)$ for the target system $G_d(s)$, using the formulation in equation (6.9) that solves an H_∞ optimization problem for a tolerance level γ.
3) The primary H_∞ controller is thus constructed by combining the H_∞ controller with the pre-compensator i.e. $H(s)=W(s)K(s)$.
4) A unity-gain, low-pass filter $F_s(s)$ is designed to reduce the effect of measurement noise. If designed properly, $F_s(s)$ can further enhance the phase tracking in addition to the primary controller $H(s)$. Consider the system in Figure 6.2 when the disturbances and noise are ignored for now, the transfer function is

$$Y(s) = \frac{X_m(s)}{X_d(s)} = \frac{G(s)H(s)}{I + F_s(s)G(s)H(s)} \tag{6.13}$$

where the $F_s(s)$ term is a phase-lag filter in the feedback path that will result in a phase-lead for the overall closed-loop system. This phase-lead design feature can be explored to further compensate the actuator inherent phase-lag to enhance the system performance.

6.3 Controller Performance and Robustness Experiment Evaluation

The experimentally identified plant displacement transfer function with the linear spring specimen is

$$G(s) = \frac{2.59e9}{s^4 + 6.12e2s^3 + 2.82e5s^2 + 4.59e7s + 2.60e9} \tag{6.14}$$

The H_∞ controller is designed using the MATLAB Robust Control Toolbox (The Mathworks Inc., 2011a). Both a model based feed-forward compensation controller (Carrion & Spencer, 2007) and an inverse compensation controller (Chen, 2007) are implemented herein for comparison purposes. Note that only the feed-forward portion of the model based compensator is evaluated. Basic linear inverse compensator is herein evaluated since the frequency domain analysis tools are not applicable when the adaptive mechanism is activated.

A series of simulation are conducted using the plant model (6.14). A chirp command displacement with 0.3” amplitude and frequency bandwidth of 0-10 Hz is used to evaluate the controllers’ tracking performance. The controller parameters vary for each simulation and the optimal values are determined to be $\alpha_{mb}=16$ (equation (1.10)) and

$\alpha_{inv}=18$ ((1.8)), each of which achieve the smallest RMS tracking error for its corresponding control strategy, respectively. The RMS tracking error is evaluated using equation (6.15) at each time step *i* of the whole response time histories.

$$E_{Tracking} = \sqrt{\frac{\frac{1}{N}\sum_{i=1}^{N}(x_{d,i} - x_{m,i})^2}{\frac{1}{N}\sum_{i=1}^{N}(x_{d,i})^2}} \times 100\% \qquad (6.15)$$

The tracking experiments are conducted too using the same setup described in Chapter 4 and the above described chirp command. Control and data acquisition are conducted at a sampling frequency of 5120 Hz. All outer-loop controllers are transformed into discrete forms using a bilinear transformation for digital implementation. The experimental RMS tracking errors are shown in Figure 6.4, which validates the selected optimal control parameters indeed yield the smallest tracking error.

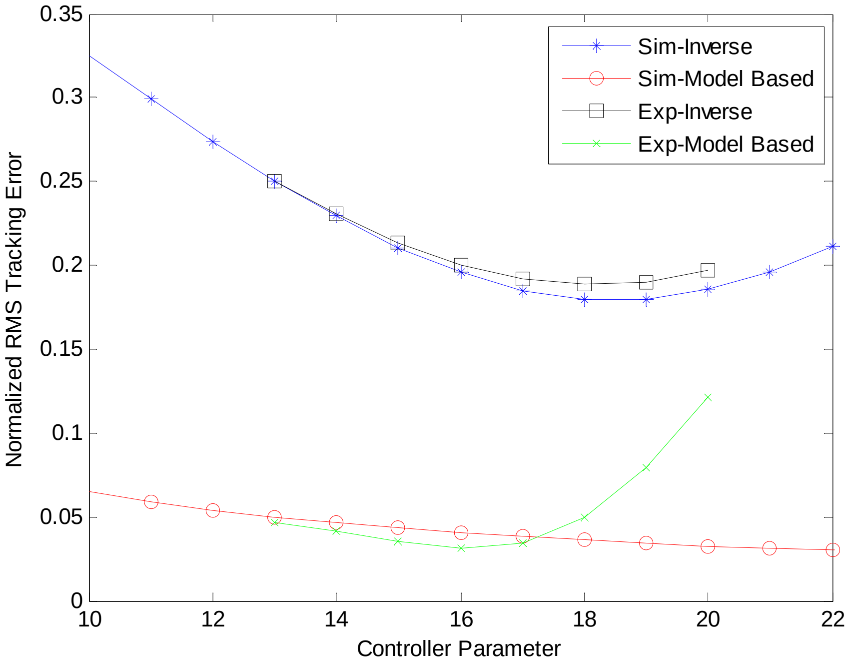

Figure 6.4 Optimal Control Parameters with the Spring Specimen

The designed H_∞ controller assume a target loop shape as

$$G_d(s) = \frac{2.39e5}{s^2 + 628.32s + 3.95e3} \tag{6.16}$$

A unity-gain, 2nd order Butterworth low-pass filter $F_s(s)$ with a cutoff frequency of 50 Hz is applied in this design for noise filtering. The experimental tracking results are compared with the PID controller and shown in Figure 6.5. It is obvious that the H_∞ controller achieves superior tracking performance over the entire evaluated frequency range, both in amplitude and phase. The overall normalized error is reduced by one order of magnitude to 2.83%. Also the displacement x-y plot shows a nearly straight 45 degree line without hysteresis.

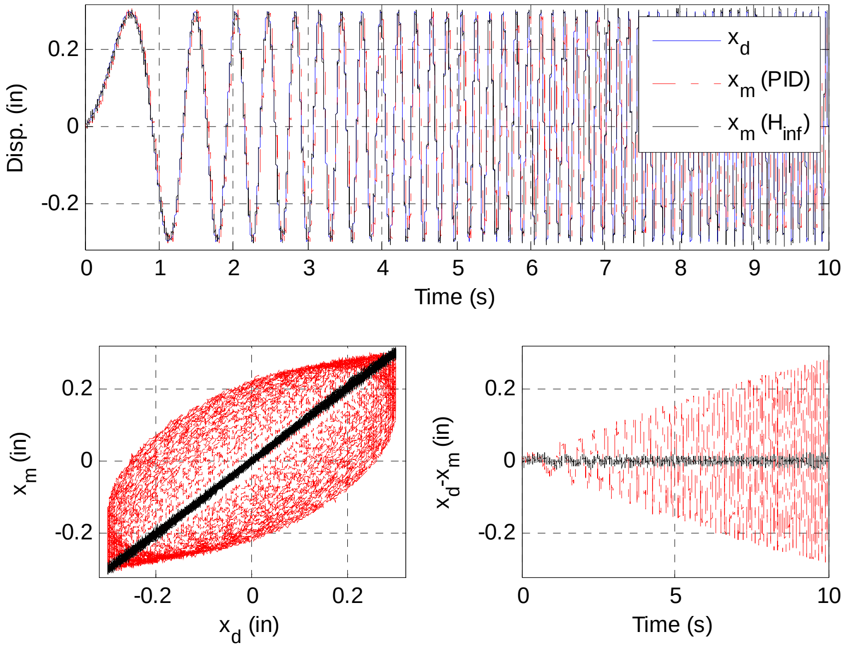

(a)

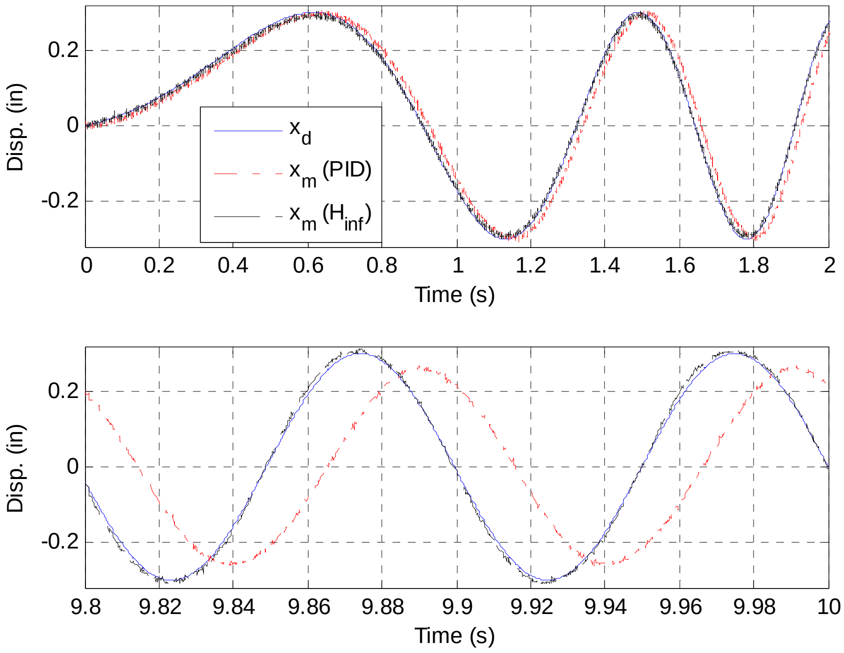

(b)

Figure 6.5 Actuator Tracking Experiment with the Spring Specimen (H_∞ Controller)

In summary, Table 6.1 shows a direct comparison of the normalized RMS tracking error using various discussed outer-loop control strategies. It is seen that both the proposed H_∞ and the model based controllers achieve very good tracking performance. But since the assumption of constant time delay is not quite applicable for this plant dynamics, the inverse controller shows degraded performance. Another set of tracking experiments are conducted by replacing the original linear spring of 215 lb/in into a stiffer one that is 345 lb/in. Experimental setup is kept identical besides this spring specimen change, while all original designed outer-loop controllers are evaluated using this new setup. Experimental tracking errors for the 2nd spring specimen are very close to the 1st one in Table 6.1, for all control strategies evaluated. This observation validates the sensitivity analysis finding in Chapter 4. It demonstrates experimentally that the plant dynamics is not sensitive to the specimen stiffness variation, at least within the considered range. An important implication for this observation is that the RTHS methodology can be quite promising for conventional structural members testing, where nonlinearity is largely associated with the structural specimen stiffness.

Table 6.1 Tracking Error Comparison with the Spring Specimen (%)

	PID	MRAC	Inverse	Model Based	H_∞
Spring #1	56.43	20.26	18.86	3.08	2.83
Spring #2	57.52	20.67	17.75	2.96	2.92

The outer-loop controllers' robustness property is evaluated through another test matrix. The inner-loop proportional gain is changed from the nominal setting of 7 to other values between 5 and 9. The sensitivity analysis in Chapter 4 indicates that the plant dynamics do vary significantly when this proportional gain is changed. The tests are repeated on spring #1 without identification or redesign the outer-loop controllers (i.e. the original controller is applied). The various outer-loop control strategies are tested on the new systems for robustness and the results are shown in Table 6.2. The performance of the model based strategy depends very much on the plant modeling accuracy so that it cannot handle the plant variation very well. The plant assumptions for both the inverse and the MRAC strategies are simplified. The nominal tracking performances using these two strategies are therefore not very satisfactory. However, the simplified plant assumptions are robust to the introduced plant changes therefore the tracking errors do not grow significantly (in some cases the errors are reduced). The proposed H_∞ controller achieves not only the best nominal performance, but also the strongest robustness to deal with the plant variation. The tracking errors using the H_∞ controller are consistently the smallest among all strategies evaluated.

Table 6.2 Robustness Evaluation with the Spring Specimen (%)

P gain	MRAC	Inverse	Model Based	H_∞
5	24.82	27.94	20.05	6.25
6	22.24	22.03	10.73	3.99
7 (nominal)	20.26	18.86	3.08	2.83
8	18.82	18.44	4.73	3.05
9	17.63	19.74	10.23	3.60

A similar procedure is tested on a single-floor, single-bay moment resisting frame (MRF) specimen. The SC6000 inner-loop controller is used with a 2.2 kip actuator to drive the motion of the MRF. The inner-loop controller proportional gain is set to 3. The experimental setup is shown in Figure 6.6. The experimentally identified actuator displacement transfer function with the MRF specimen is shown in Figure 6.7.

$$G(s) = \frac{4.52e9}{s^4 + 577s^3 + 2.68e5s^2 + 6.28e7s + 4.93e9} \tag{6.17}$$

The optimal outer-loop controller parameters are chosen in this case as $\alpha_{mb}=17$ and $\alpha_{inv}=15$, respectively, which are determined from Figure 6.8 that can best track the pre-defined chirp displacement trajectory.

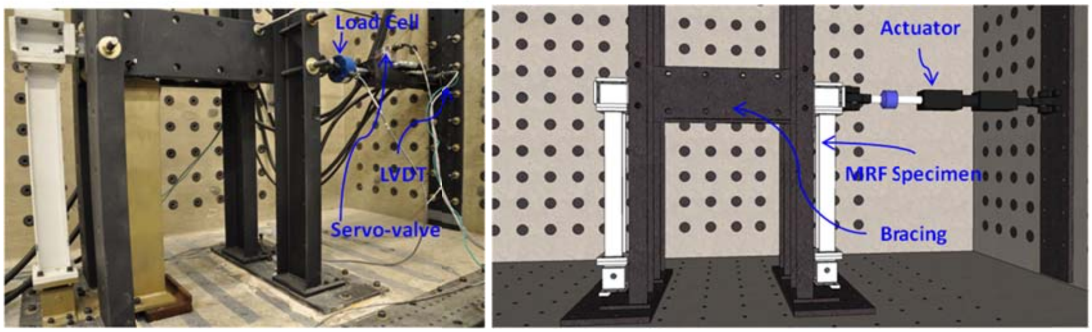

Figure 6.6 Single Floor MRF Experimental Setup

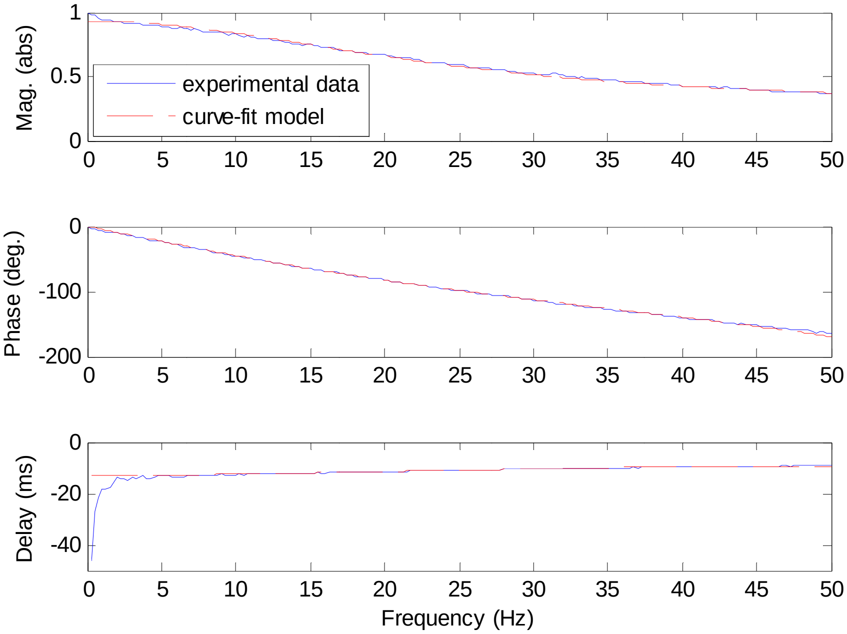

Figure 6.7 Experimental Transfer Function with the MRF Specimen

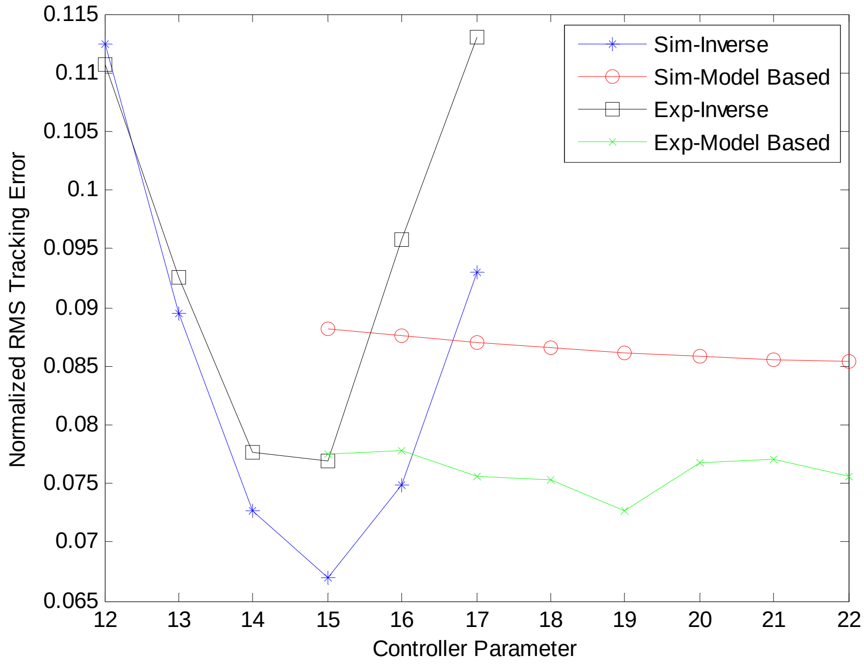

Figure 6.8 Optimal Control Parameters with the MRF Specimen

The H_∞ controller design assumes the same target loop shape in equation (6.16). The designed open loop gain shape is shown in Figure 6.9 that follows the target loop $G_d(s)$ within a tolerance level. T_s and S_s are presented too. T_s is very close to unity in the low frequency range that guarantees a good tracking performance. At the other end, T_s is small in the high frequency range for increased robustness where modeling error is large. Figure 6.10 provides a plot of the plant transfer function $G(s)$ used in this study, and comparisons with the outer-loop H_∞ control systems. The phase error is reduced to nearly zero when $F_s(s)$ is considered. Phase improvement herein is more than 30 times compared to the system without $F_s(s)$ and 90 times compared to the plant, at the extreme upper end of the bandwidth at 25 Hz. The trade-off is that the magnitude at the highest frequency in this bandwidth is amplified by about 1.6.

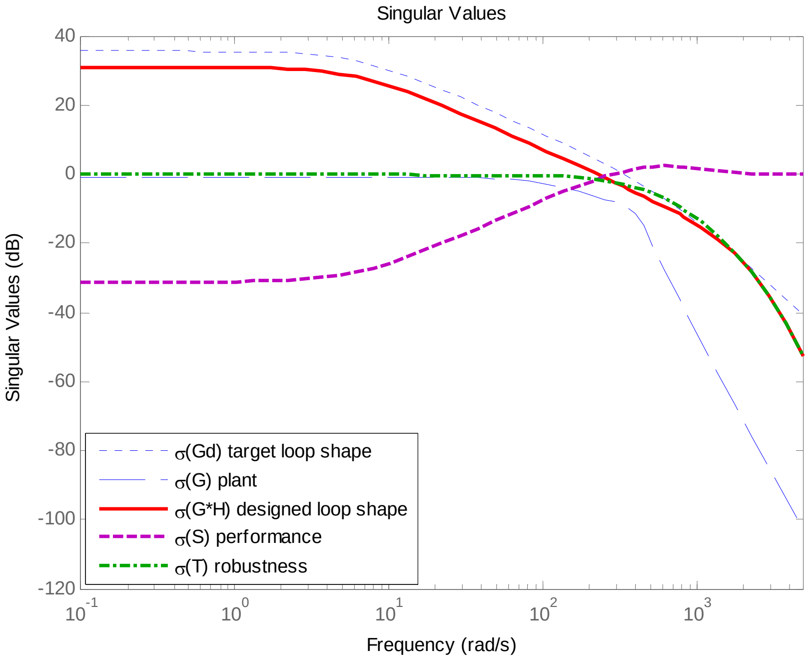

Figure 6.9 H_∞ Controller Design with the MRF Specimen

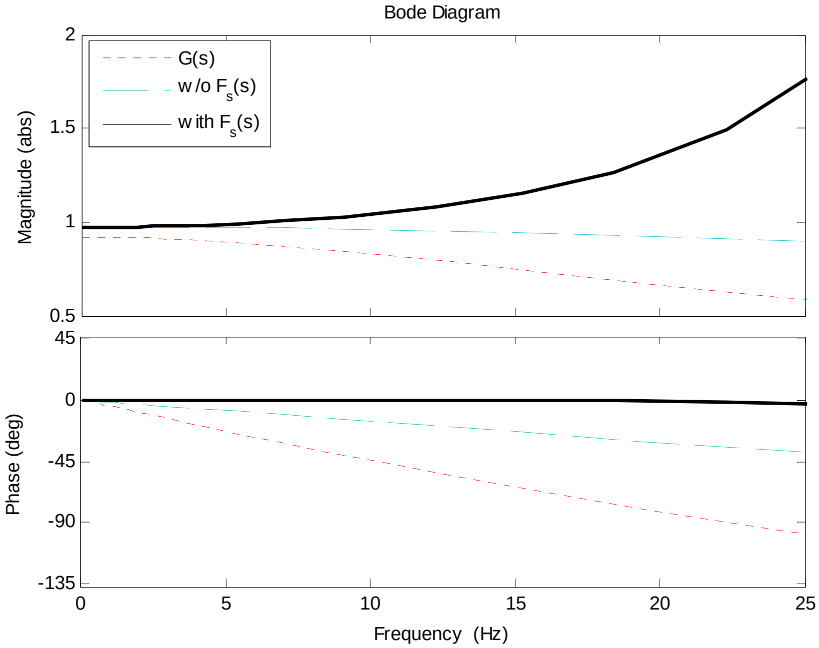

Figure 6.10 Transfer Function of the H_∞ Outer-loop Control System

The moderate target loop gain designed herein is a consideration to accommodate the relatively large physical system modeling error and nonlinearity. Control and data acquisition are conducted at a sampling frequency of 1024 Hz for this test matrix, which is a more realistic value for the RTHS applications.

Table 6.3 summarizes a comparison of the normalized actuator tracking error with the MRF specimen. The MRAC design tends to go unstable for these tests, due to the large plant uncertainty, so that it is not included in this study. This experimental setup is more challenging compared to the linear spring test because the specimen has its own dynamics with complicated boundary conditions. The specimen stiffness increases tremendously, which induces much stronger control structure interaction. Although the plant becomes more complicated, the inverse controller tracking performance improved compared to Table 6.1. This observation can be explained in Figure 6.7 where the actuator delay is fairly constant when the MRF specimen is tested, which satisfies the assumption of the inverse control strategy. It is observed that the proposed H_∞ controller still performs the best among all controller evaluated.

Table 6.3 Tracking Error Comparison with the MRF Specimen (%)

PID	Inverse	Model Based	H_∞
44.07	7.70	7.57	4.59

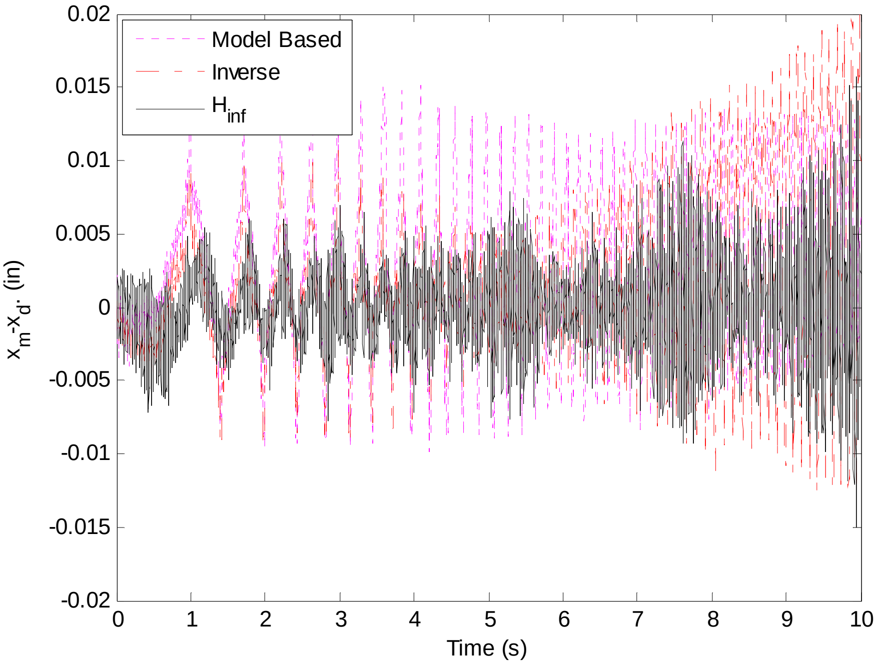

Figure 6.11 Actuator Tracking Error with the MRF Specimen

The experimental tracking error time histories with the MRF specimen are compared in Figure 6.11. It is observed that the inverse controller yields an increased error when the signal frequency increases. The model based controller yields significant error at lower frequencies. The tracking error dynamic patterns are different for each outer-loop controller evaluated. The analysis of this error and its implication in terms of RTHS stability and accuracy are investigated in Chapter 7, to demonstrate further the superior performance of the proposed H_∞ strategy. The H_∞ controller robustness property is demonstrated too in the following chapters.

6.4 Summary

An H_∞ loop shaping control strategy is introduced in this chapter. The original formulation of the control design is presented first and then a filtering design technique is proposed to facilitate physical implementation. The superior performance of the proposed controller is demonstrated experimentally to control the hydraulic actuator motion, using both a linear spring and a MRF specimen. The proposed controller is observed to achieve not only the smallest tracking error in general, but also strong robustness when the plant dynamics is subjected to variation. The actuator tracking delay can be reduced from more than 10 ms using the PID controller to less than a fraction of 1 ms using the proposed H_∞ controller. The H_∞ controller will be evaluated in the next chapters for the RTHS applications, which can nearly triple the test stability limit compared to several other strategies.

CHAPTER 7
SINGLE FLOOR MRF EXPERIMENT

A validation test matrix is constructed using the single floor MRF specimen to evaluate the effectiveness of the developed RTHS framework. The test matrix assumes the worst case substructure scheme. A generalized dynamical system analysis procedure is applied to evaluate the various RTHS components and their complex interactions. Several outer-loop control strategies are evaluated including the proposed H_∞ controller. A series of RTHS systems are compared against the reference structural systems. The stability limit and test accuracy can be predicted well before conducting online testing. The test matrix is then experimentally validated and the results show great similarity compared with the analysis results. The proposed H_∞ control strategy is demonstrated to improve significantly both the test stability limit and accuracy. Another key feature of the proposed controller is its robust performance in terms of unmodeled dynamics and uncertainties, which inevitably exist in any physical system. This feature is essential to enhance test quality for specimens with nonlinear dynamical behavior, thus ensuring the validity of proposed approach for more complex RTHS implementations.

7.1 Test Matrix Construction

The selection of the substructures is based on the worst case proportioning scheme discussed in Chapter 3. The single floor MRF specimen is tested experimentally using the setup described in Chapter 6. The numerical substructure assumes seismic mass and damping but no stiffness. The RTHS system is therefore added to a maximum amount of negative damping when the experimental substructure is subjected to a lag/delay. A schematic view of this worst case RTHS setup is shown in Figure 7.1. In practice, a small amount of stiffness K_n needs to be assumed in the numerical substructure to avoid the mathematical singularity in this problem.

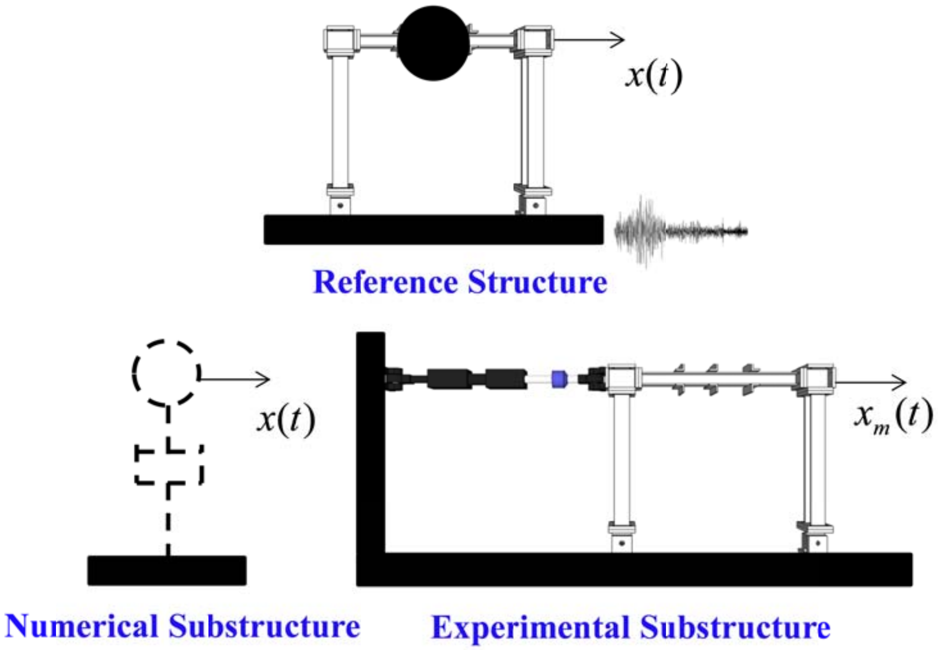

Figure 7.1 Worst-case RTHS Substructure Scheme

The MRF stiffness is obtained using a quasi-static test with a displacement trajectory shown in Figure 7.2. Experimental MRF properties are identified and listed in Table 7.1. Note that the physical damping C_e is challenging to identify accurately when the hydraulic actuator is attached. The influence of C_e on RTHS accuracy is elaborated in the later section of this chapter.

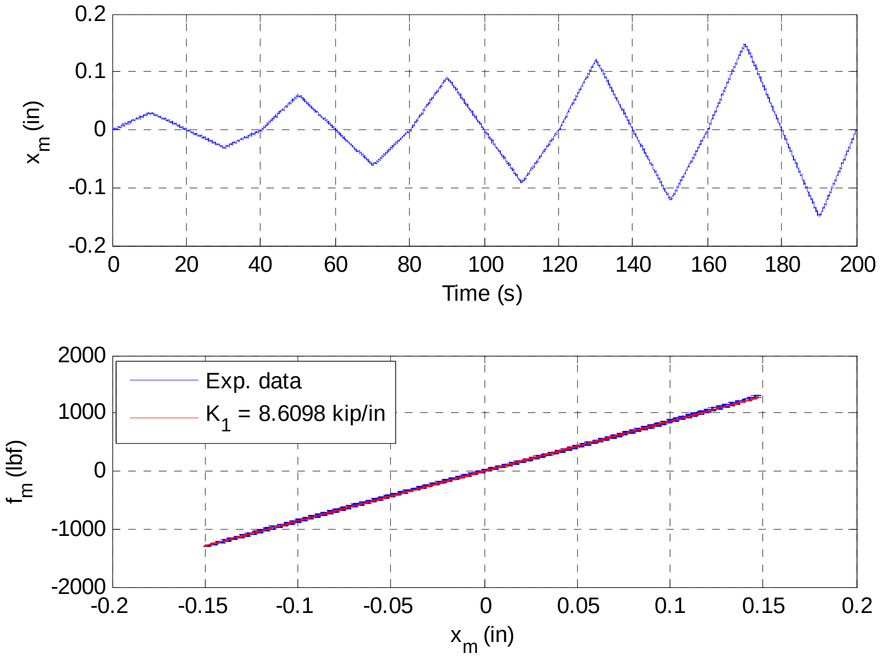

Figure 7.2 Quasi-static Test on the Single Floor MRF

Table 7.1 Test Matrix Structural Parameters

	Experimental	Numerical	Reference
Mass (lb-s^2/in)	M_e=8.55e-2	$M_n=M_t-M_e$	$M_t= K_t/\omega^2$
Stiffness (lb/in)	K_e=8.6e3	$K_n=0.01$ x K_e	$K_t= K_e+K_n$
Damping (lb-s/in)	C_e=5.42	$C_n=C_t-C_e$	C_t=2 x 0.02 x $(M_t$ x $K_t)^{1/2}$

A series of systems are constructed by assuming different values of the natural frequency ω of the reference structure. The total mass M_t is determined for each chosen ω and the total damping ratio is assumed to be *2%* in each reference system. The numerical mass and damping are thus obtained by subtracting the experimental parts from the reference structure. This imbalance of mass and stiffness configuration represents the (semi) worst-case RTHS system configuration illustrated in Chapter 3, e.g. when $\omega=1Hz$, $\alpha=3.9e-4$ and $\beta=100$.

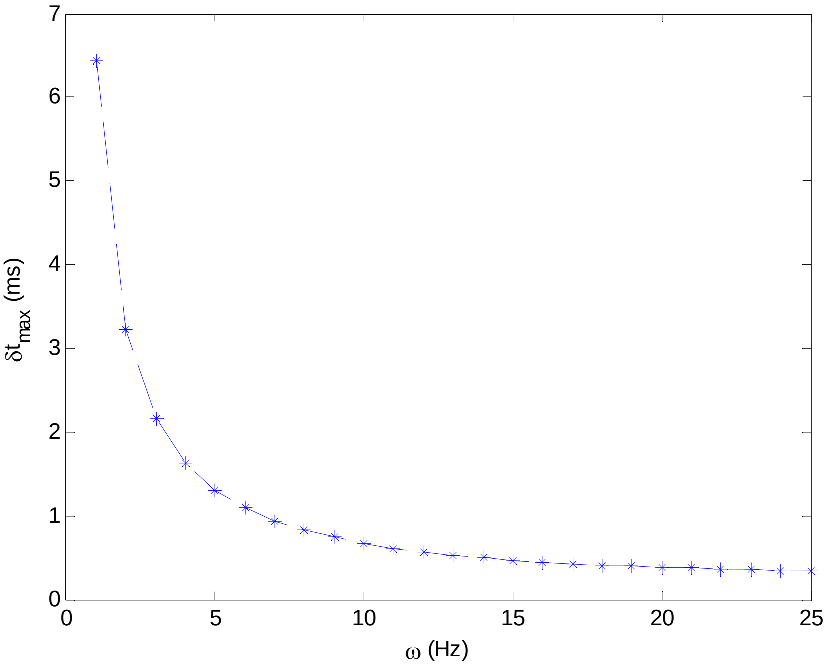

Figure 7.3 Maximum Allowable Delay

One quick way to estimate the maximum allowable system delay, once the test setup is determined, is by calculating damping term in equation (3.4). If we assume perfect amplitude tracking $\Delta=1$, $\delta t_{\max} \leq C_t /(K_e - M_e\omega^2)$ is a useful index to evaluate the RTHS system stability margin. Δ can be obtained more accurately using the transfer function magnitude, once a tracking controller is selected. Figure 7.3 shows this maximum allowable delay limit for the designed test matrix in this chapter. Dramatic challenges arise as the frequency ω increases because: 1) the physical actuator has to track a higher frequency signal; 2) the physical substructure represents a larger portion as the numerical mass is reduced, and is the source of most of the experimental error. Notice that about 1/3 ms delay drives the RTHS system to instability when ω increases to 25Hz. For the actuators used in this study, the inner-loop servo-actuator delay is about 12-13 ms within the bandwidth of interest. Thus, without an advanced motion control system, a stable RTHS cannot be achieved even at a very low frequency of $\omega=1Hz$. This conclusion is validated and shown experimentally later.

7.2 Frequency Domain RTHS System Analysis

The dynamics of the closed-loop RTHS systems are analyzed before conducting physical experiments. A reference structure is used to examine the system error. In addition to the proposed H_∞ strategy, both the model based and the inverse compensation strategies are implemented and evaluated. The optimal controller parameters are chosen as $\alpha_{mb}=17$ and $\alpha_{inv}=15$, respectively, as determined in Chapter 6. The RTHS system transfer functions of each system, from the input ground acceleration to the output displacement x_d, are compared in Figure 7.4 for the case of $\omega=1Hz$, $5Hz$ *and* $8Hz$, respectively. In this analysis, the transfer function calculations are performed in the continuous-time domain. It is clear that the proposed H_∞ RTHS system does match the reference system dynamics very well for all cases, especially near the system's fundamental frequency. Other RTHS systems considered appear to perform reasonably well when $\omega=1Hz$. But significant natural frequency shifts and damping reductions are observed when the fundamental frequency increase to $\omega=8Hz$. Analysis shows that a further increased frequency at $\omega=9Hz$ will cause system instability. One drawback of the proposed H_∞ design is that it introduces a 2nd artificial mode for the RTHS system at around 37Hz. This mode is caused by the low-pass filter in the H_∞ controller design, in which the primary objective is to minimize phase lag. Although we need to be aware of it, this mode is beyond the bandwidth of typical earthquake engineering applications.

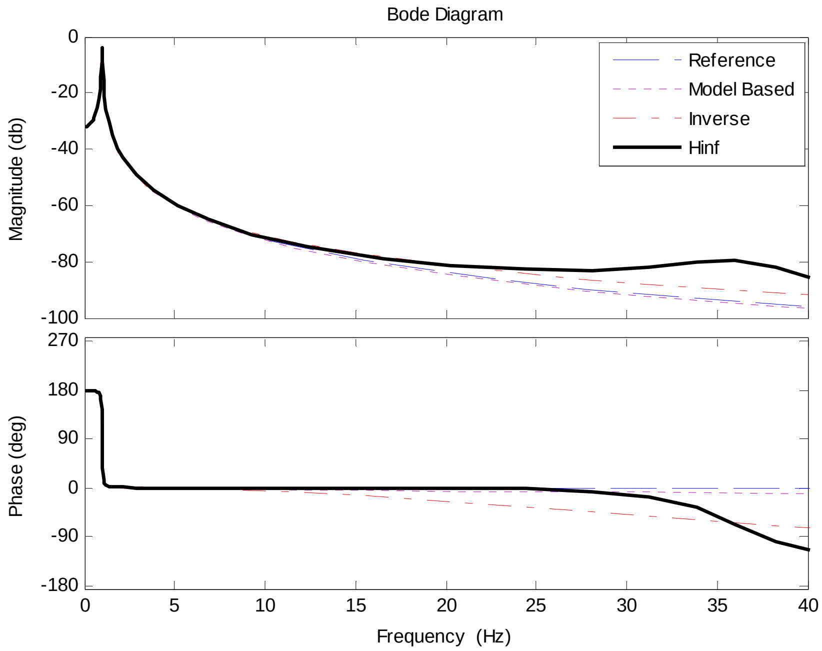
Bode Diagram
Magnitude (db)
0
-20
-40
-60
-80
-100
Phase (deg)
270
180
90
0
-90
-180
0
5
10
15
20
25
30
35
40
Frequency (Hz)
Reference
Model Based
Inverse
Hinf

(a)

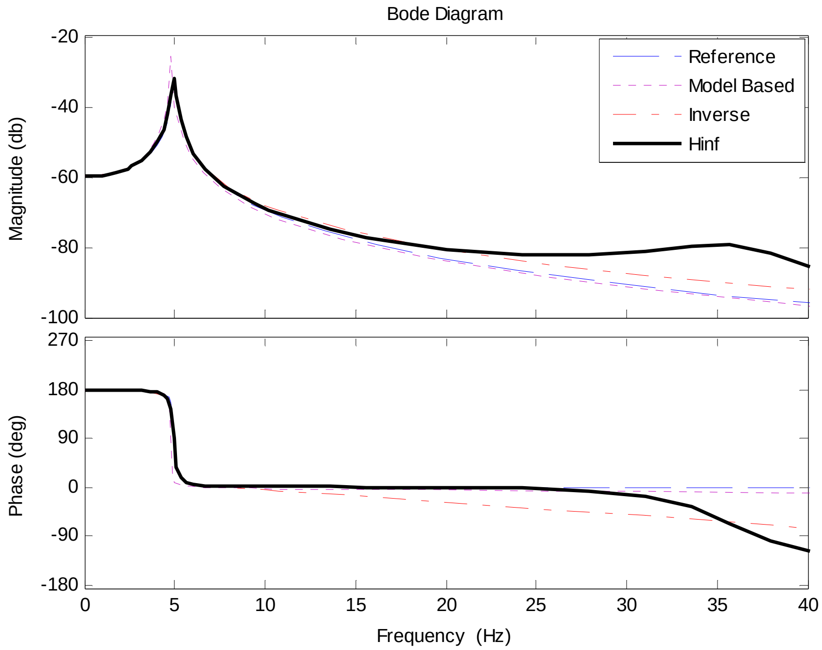
Bode Diagram
Magnitude (db)
-20
-40
-60
-80
-100
Phase (deg)
270
180
90
0
-90
-180
0
5
10
15
20
25
30
35
40
Frequency (Hz)
Reference
Model Based
Inverse
Hinf

(b)

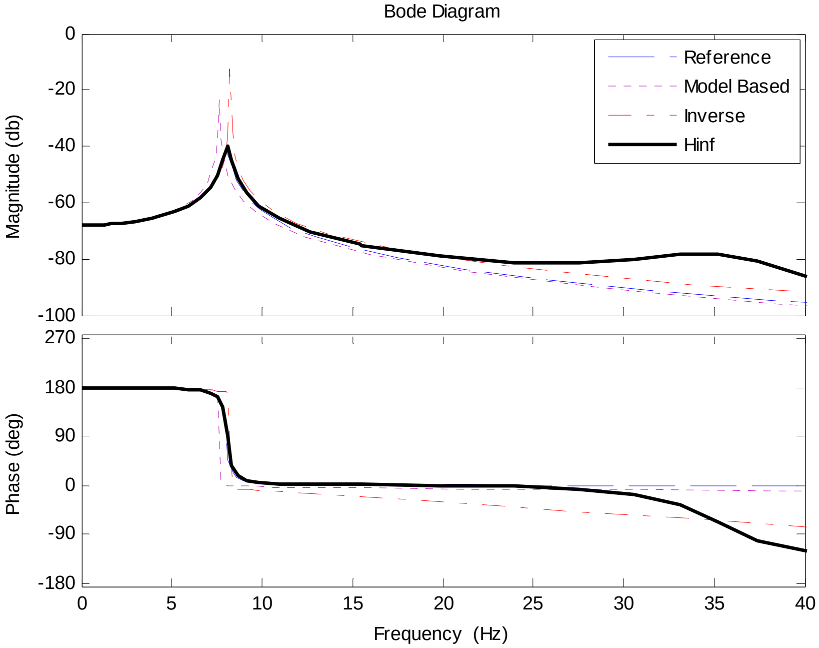

(c)
Figure 7.4 RTHS and Reference Systems
(a): *ω=1Hz;* (b): *ω=5Hz;* (c): *ω=8Hz*

In these lightly damped systems the essential dynamics can be characterized by the maximum gain, i.e. transfer function magnitude peak (M_{RTHS}), and its associated frequency (ω_{RTHS}). The normalized maximum system gain error is thus defined as the Euclidean norm of the distance between the RTHS and the reference system maximum gain (M_{REF}).

$$E_{SS} = \sqrt{\left(M_{RTHT} / M_{REF} - 1\right)^2 + \left(\omega_{RTHT} / \omega - 1\right)^2} \tag{7.1}$$

This index is useful to capture both the shift in the system frequency and the error in the magnitude. The normalized error for each of the system is plotted against the fundamental frequency in Figure 7.5. Larger errors indicate that the RTHS system is approaching unstable behavior.

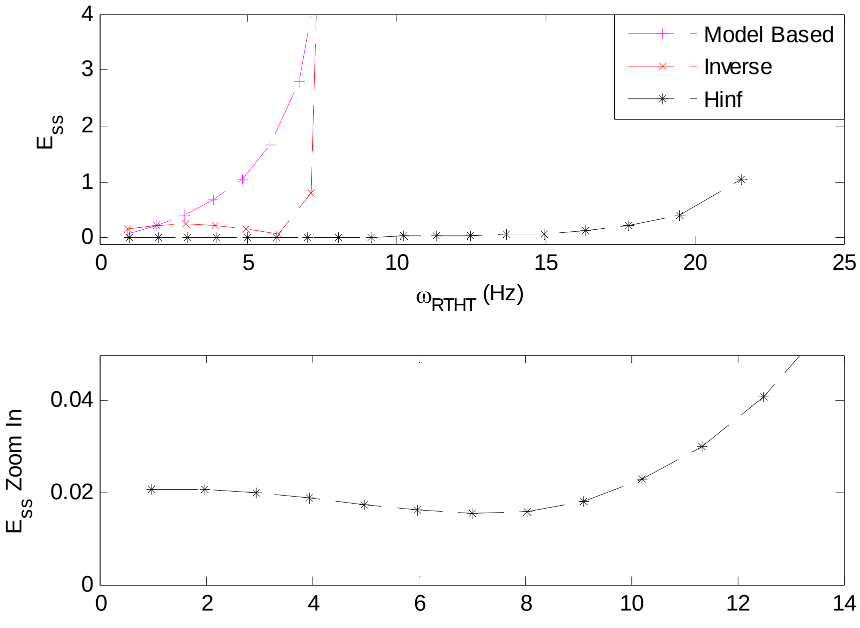

Figure 7.5 Normalized RTHS System Error

7.3 RTHS Experimental Validation

The procedure discussed in the previous section is repeated using the experimental setup in Figure 6.6. The responses are kept within the elastic range of the physical frame so that they are ready to be compared with the reference analytical solutions. The text matrix in Table 7.1 is subjected to the NS component of the 1940 El-Centro earthquake. The input is scaled by a gain that ranges between 0.02 to 3 times the original intensity, to accommodate the actuator force and stroke capacity for the various structural configurations, and to standardize the amplitude of the actuator motion. All tests are conducted in real-time, with a sampling rate of 1024Hz. The equation of motion for the numerical substructure is evaluated using the CR integration algorithm within the RT-Frame2D code (nees.org). All outer-loop controllers are transformed into discrete forms using a bilinear transformation for digital implementation. Note that the designed H_∞

controller in this study has 11 dynamical states in total. For more complicated applications when a large number of controller states may be expected, model reduction techniques can be used to simply the controller while retaining its performance characteristics.

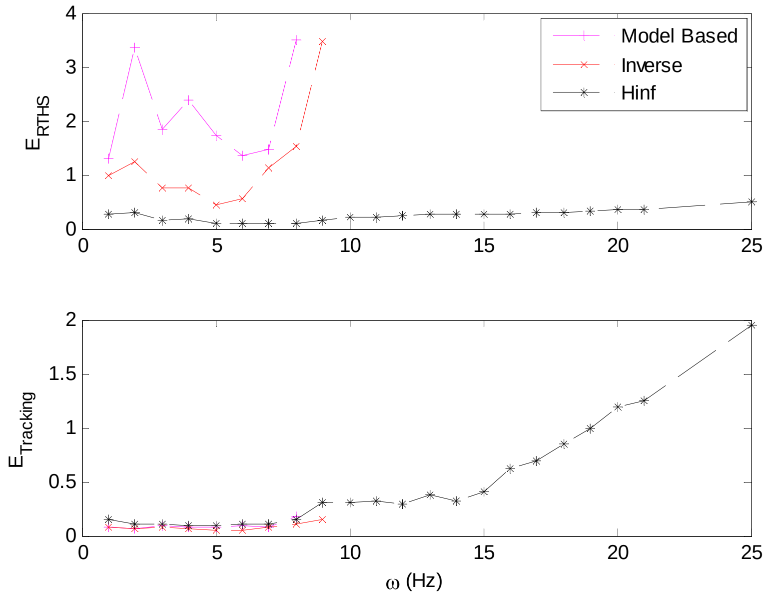

Figure 7.6 Normalized RTHS and Tracking Error

The normalized RMS values of the RTHS error (E_{RTHS}) and the actuator tracking error are calculated and shown in Figure 7.6, where errors are evaluated at each time step i of the whole response time histories using the expression in equation (6.15) and (7.2). Note that only the feed-forward portion of the model based compensator is evaluated. Basic linear inverse compensator is herein evaluated since the frequency domain analysis tools are not applicable when the adaptive mechanism is activated.

$$E_{RTHS} = \sqrt{\frac{\frac{1}{N}\sum_{i=1}^{N}(x_{ref,i} - x_{d,i})^2}{\frac{1}{N}\sum_{i=1}^{N}(x_{ref,i})^2}} \times 100\% \tag{7.2}$$

Several important observations are made:

1) The inner-loop PID control alone is not adequate to run a stable RTHS test, even at the low natural frequency of $\omega=1Hz$. This observation demonstrates that the selected experimental setup is indeed quite challenging, and therefore requires a high quality motion controller.
2) The proposed H_∞ controller can significantly extend the RTHS stability limit to $\omega=25Hz$.
3) In general, the proposed H_∞ controller achieves the smallest RTHS error of the cases considered. This conclusion is clear from both frequency domain analysis (Figure 7.5) and time domain experimental results (Figure 7.6).
4) Strong correlations are observed between the analysis and experimental results. Specifically the stability limit of 8-9Hz is successfully predicted for both the model based and the inverse controllers. In terms of accuracy, the inverse controller can achieve the smallest error at $\omega=6Hz$ as indicated by analysis. The relative large error with the model based controller is partly related to errors in the system identification process. This discrepancy is addressed in the next section.

The results from this study increase the creditability of performing offline simulation to investigate more complicated RTHS systems. Important issues can be investigated that may be difficult to study experimentally, such as parameter sensitivity, characterization of system, uncertainty bounds, etc. Controller stability and performance limits can be enhanced when more physical system information is available.

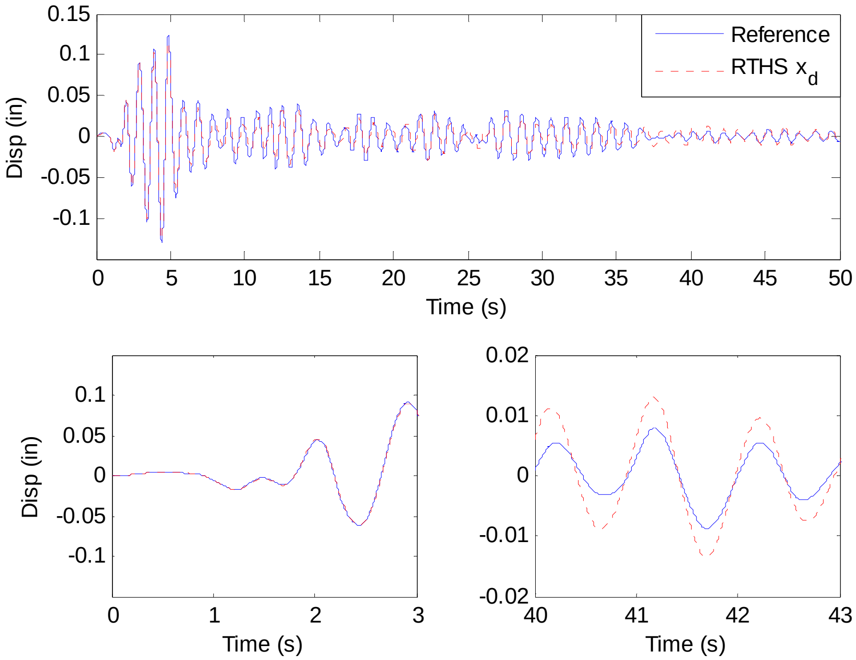
Reference
RTHS x_d
Disp (in)
Time (s)
0.15
0.1
0.05
0
-0.05
-0.1
0 5 10 15 20 25 30 35 40 45 50
0 1 2 3
0.02
0.01
-0.01
-0.02
40 41 42 43

(a)

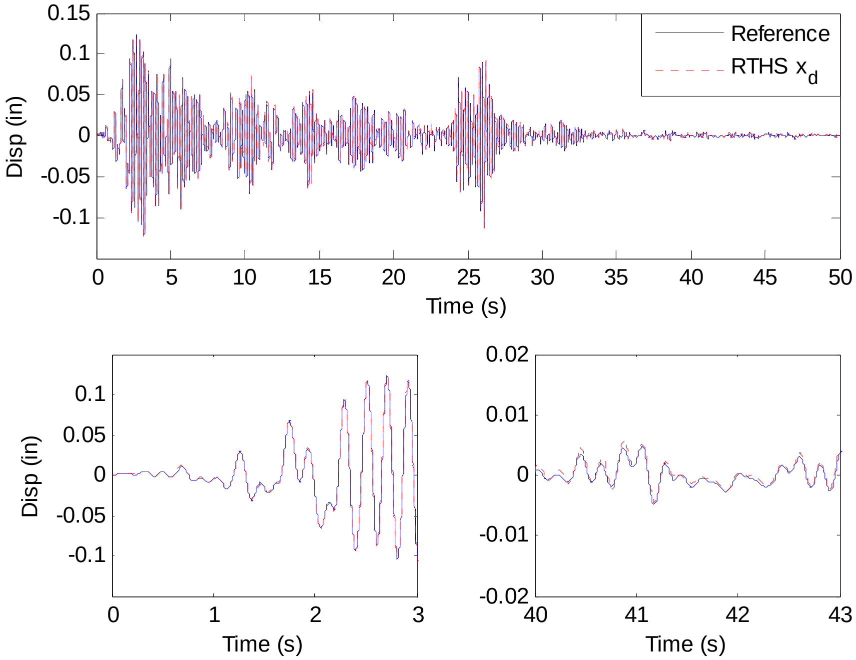
Reference
RTHS x_d
Disp (in)
Time (s)
0.15
0.1
0.05
0
-0.05
-0.1
0 5 10 15 20 25 30 35 40 45 50
0 1 2 3
0.02
0.01
-0.01
-0.02
40 41 42 43

(b)

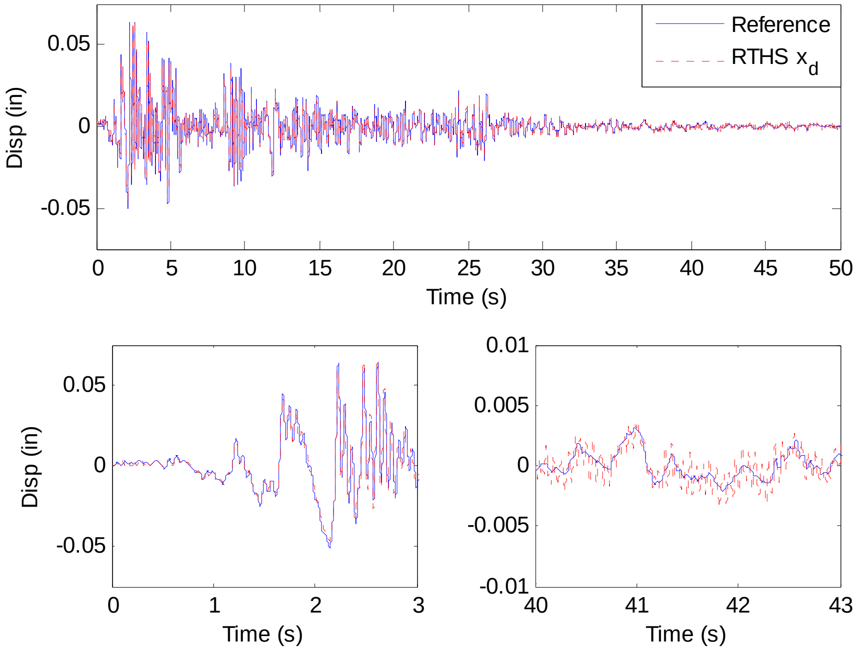

(c)

Figure 7.7 RTHS Error Assessment
(a): *ω=1Hz;* (b): *ω=5Hz;* (c): *ω=15Hz*

Figure 7.7 provides time histories of the RTHS responses using the H_∞ controller. They are compared with the time histories of the reference structural responses at *ω=1Hz* (a), 5Hz (b) and 15Hz (c), respectively. Good comparisons are observed in all cases, demonstrating the effectiveness of the proposed control strategy. The comparison of responses with *ω=5Hz* shows better match than at 1Hz, which appears to be counterintuitive. However, the proposed system analysis procedure is able to predict this successfully, as shown in Figure 7.5.

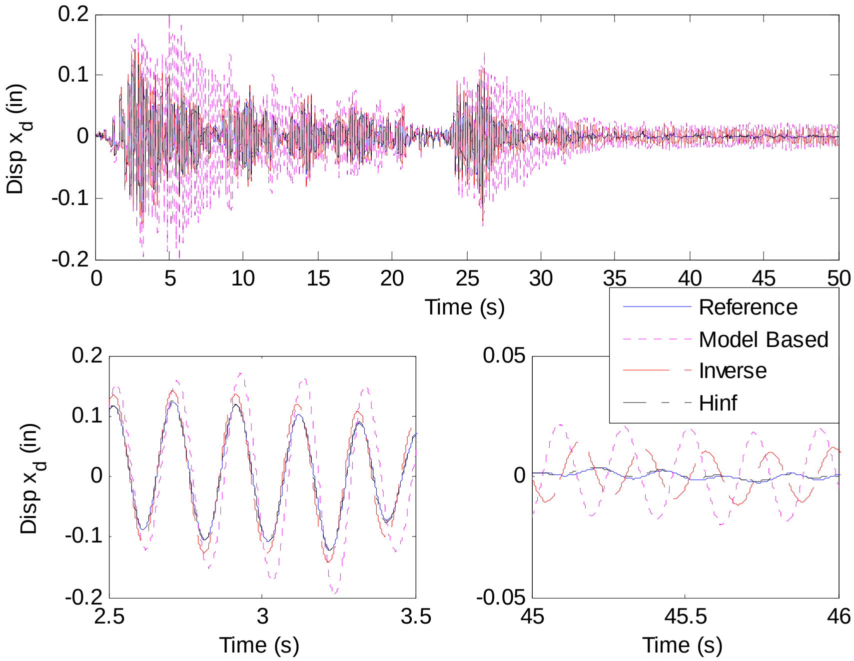

Figure 7.8 RTHS Results Using Various Controllers

Additional challenges exist when the earthquake magnitude is small, such as near the end of the used El-Centro record. The comparison is not as good here due to the presence of a large noise to signal ratio. For instance, focusing on the region between 40-43 seconds (lower right subplot in Figure 7.7), high frequency oscillations occur because the 2nd mode of the H_∞ RTHS system is excited by the measurement noise. This effect is more pronounced with higher system frequencies (e.g., when $\omega=15Hz$), as the test dynamics are approaching the 2nd mode of RTHS system of 37Hz in this case, as shown in Figure 7.4. This type of oscillation is a common observation in RTHS community and is reported by other researchers in [(Bonnet, et al., 2007), (Shing & Mahin, 1987)]. Representative time domain comparisons are also made for the various control strategies in Figure 7.8 when experiments are conducted at $\omega=5Hz$. The results demonstrate the superior performance of the proposed H_∞ controller.

Another interesting observation considers the apparent contradiction between the hybrid simulation error and the tracking error in Figure 7.6. Although the H_∞ controller does achieve the smallest global RTHS error in general, the RMS tracking error using this method is relatively large among the three controllers evaluated. The experimental tracking error time histories at $\omega=5Hz$ are compared in Figure 7.9. It can be observed that the tracking error with the H_∞ controller is largely due to the presence of the 2nd artificial mode, as shown in Figure 7.4, being excited by the system noise. No other significant frequency content therefore is present in the signal. Significant RMS error is introduced by this local high frequency oscillation. Although this effect is not ideal, the good match in the RTHS results shown in Figure 7.4 and Figure 7.7 demonstrate that the global dynamics are maximally preserved using the proposed H_∞ controller. The tracking error evaluated using equation (6.15) is normalized with respect to x_d. This term in the denominator can become quite large due to the RTHS system negative damping so that the normalized error appears small. The tracking errors using other two controllers in Figure 7.9 show strong patterns that indicate uncompensated dynamics within the closed-loop system. The selected worst-case test matrix considers the most challenging test configuration, and thus is very sensitive to the propagation of this small tracking error that eventually results in very large RTHS error. Improved hardware with a small noise level is essential for high quality RTHS implementation. One way to minimize the effects of noise is to use larger input earthquake intensity. This observation also leads to the conclusion that the tracking error RMS value alone may not be sufficient to fully characterize a controller's performance in terms of RTHS accuracy. The dynamic pattern of the error time history needs to be evaluated too.

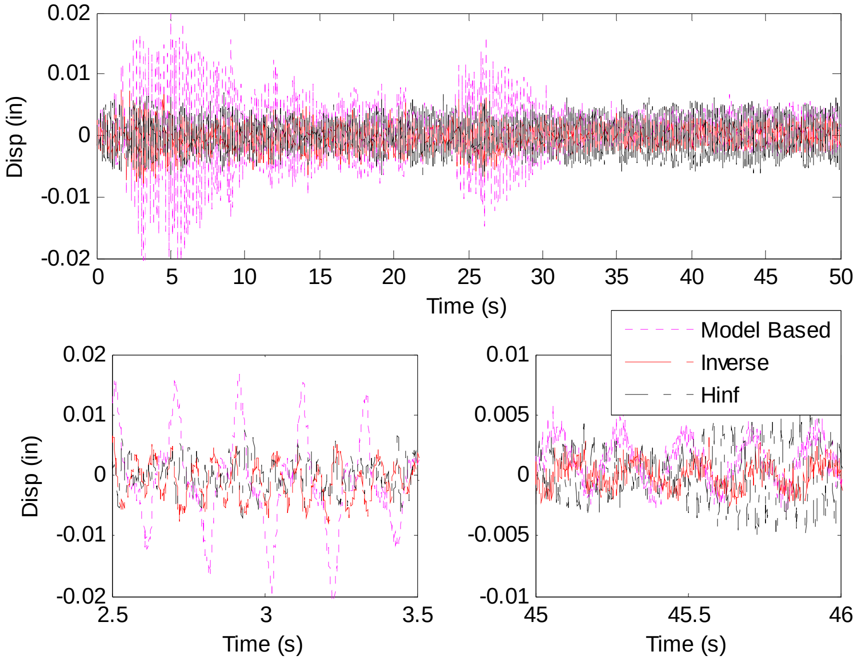

Figure 7.9 Actuator Tracking Error Using Various Controllers

7.4 Robustness and RTHS Experimental Error Analysis

Much of the attention so far has been emphasized on the nominal performance of the motion controller. Although analysis based on linear time invariant systems are good enough to capture the essential dynamics, parameter uncertainty and unmodeled dynamics are inevitable in the physical system. A relevant example in the structural engineering community is the nonlinear stiffness that can arise during the test of a frame specimen. Actuator electrical and mechanical parts also have their own nonlinearities that are not considered in the control design, moreover there is strong interaction between the actuator and the structure when the frame stiffness is high. Having a robust controller is highly desirable for the ultimate RTHS goal of testing complex systems that may not have a reliable model. High quality parametric identification in these cases may be very challenging to perform, or perhaps impossible.

Here we evaluate the robustness of the controller design by introducing uncertainty in a controlled manner. The inner-loop controller proportional (P) gain is changed from the nominal value of 3.0 to both 2.5 and 3.5. Then the tests at $\omega=6Hz$ are repeated without identification or redesign (i.e. the original controller is applied). The various actuator control strategies are tested on the new systems for robustness and the results are shown in Table 7.2. Clearly the H_∞ controller has quite consistent performance. But the feed-forward controllers are not as effective, especially when the proportional gain is reduced. The experimental errors in these tests become too large.

Table 7.2 Controller Robustness Assessment Using RTHS Error (%)

	Model Based	Inverse	H_∞
P gain=2.5	1261.1	585.4	22.8
P gain=3 (nominal)	134.4	55.64	9.56
P gain=3.5	56.61	50.27	24.96

Another demonstration for the H_∞ controller robustness is to consider the identification error. A relative sharp magnitude slope change is observed at a low frequency in the plant experimental transfer function, from the actuator command to output measured displacement. The assumed form of the plant in equation (6.17) has four poles and no zeros, which cannot capture this magnitude drop as shown in Figure 7.10. The DC gain of the plant model is therefore less than unity which may partially explain why the performance of model based strategy is not as good as one might expect. Note that the apparent large delay at very low frequencies is simply due to the noise in the experimental transfer function. Despite this modeling imperfection and identification error, the proposed H_∞ controller behaves very well. The robustness feature herein reduces the dependence of controller performance on the prior identification accuracy.

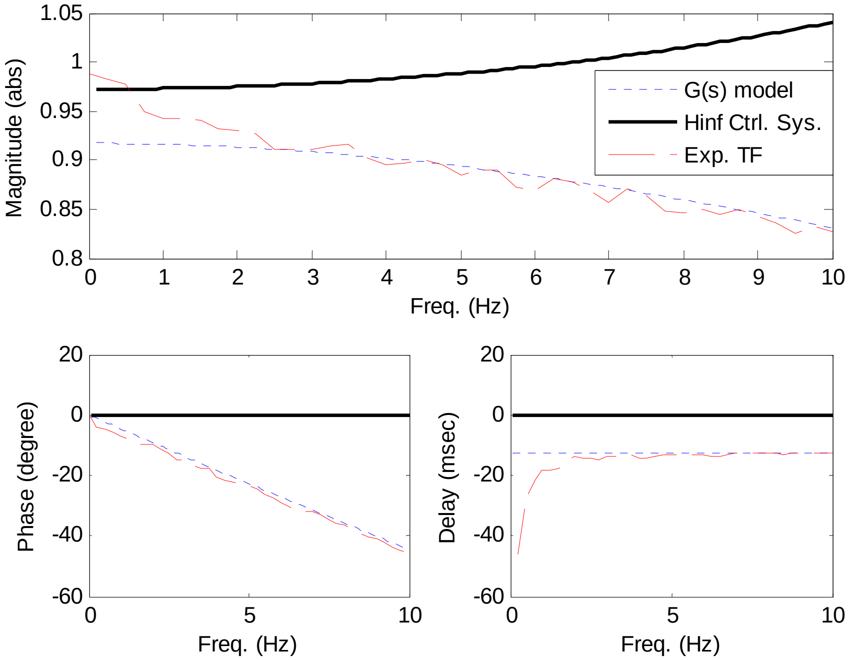

Figure 7.10 Identification Error and Control Design

One of the key reasons one might choose to perform real-time testing is to preserve the rate dependent characteristics of experimental substructure. Although small in scale, the structure used in this study represents a typical moment resistant frame that is commonly used in civil engineering practice. The frame carries significant stiffness but comparably very small self weight and damping, which would normally be ignored, for instance, in slow speed pseudo-dynamic testing. This assumption is justifiable when ω is small but will cause error at higher ω because the velocity and acceleration terms play a more significant role. The test matrix selected herein provides a good demonstration to justify the need for performing these tests in real-time and to preserve these higher order dynamics.

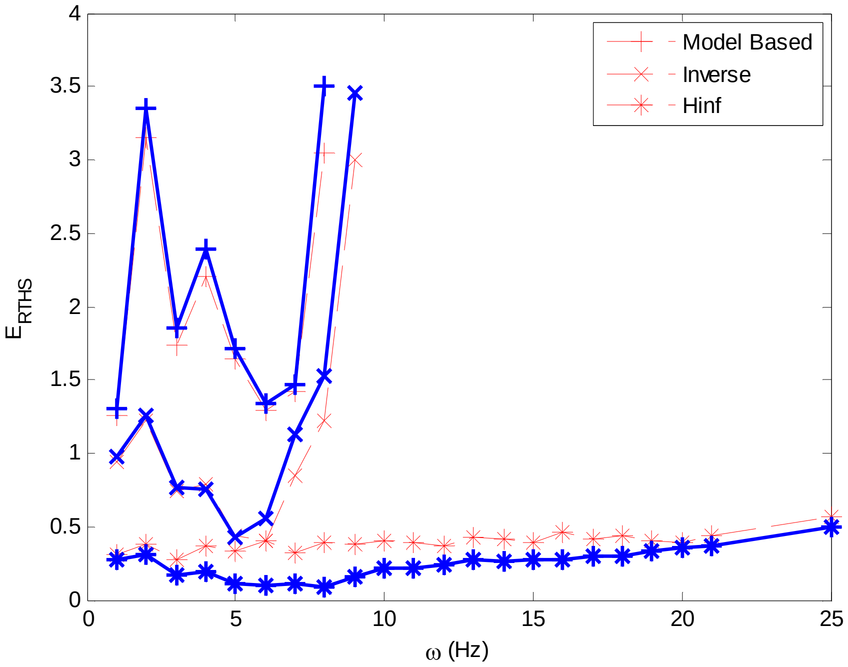

Figure 7.11 Effects of Experimental Mass and Damping

The light dashed curves in Figure 7.11 assume $M_n=K_t/\omega^2$ and $C_n=2 \text{ x } 0.02 \text{ x } (M_t \text{ x } K_t)^{1/2}$ directly in the numerical substructure. The dark solid curves are obtained using a correction to account for the presence of the physical mass and damping. They are obtained by subtracting the identified M_e and C_e from the numerical substructure, yielding a true representation of the proposed test matrix in Table 7.1. Therefore the solids curves maintain the same global properties (the summation of numerical and experimental substructures) as in the reference structure. But the dashed curves repeatedly assume experimental mass and damping. The H_∞ RTHS system can achieve significantly reduced errors after making this correction, but the other two controllers appear to yield even larger errors. Note that this may explain why the approach of adding significant numerical damping often works during a RTHS to balance the negative damping caused by inappropriately compensated actuator delay.

This study furthermore demonstrates the importance of having a high precision motion tracking controller to achieve good RTHS accuracy. The damping in a continuum frame structure may be quite complex, and even nonlinear, especially when the hydraulic actuator is connected and interacts with the frame. Although it is possible to further reduce RTHS error by adjusting damping value for each individual test, the optimal value of $C_e=5.42\ lb\text{-}s/in$ is assumed in all tests herein to be consistent. This assumption is equivalent to 10% proportional damping of the physical MRF substructure. Although it is high for a typical steel structure, the damping only represents a small portion of the total assumed reference structure damping. The heuristic damping assumption herein is intended to be an initial simplified procedure to consider the actuator contribution/interaction (Dyke, Spencer, Quast, & Sain, 1995) into the RTHS system. Further understanding is needed to model the dynamic coupling and interaction between actuator and specimen. Although the proposed H∞ strategy can already achieve excellent displacement tracking performance, a more refined force tracking mechanism may be another important RTHS component to further enhance the test accuracy.

7.5 Summary

The proposed H_∞ looping shape control strategy is characterized not only by its superb performance in terms of stability and accuracy, but also its strong robustness in terms of physical system uncertainties. It is demonstrated that the significance of RTHS error depends not only on the actuator motion tracking error, but also heavily on the partitioning of the structure between numerical and experimental components. The worst-case scenario is analyzed and validated experimentally. The proposed physical MRF specimen and assumption of computational model may be ideal as a benchmark problem to evaluate tracking controller performance. The self-weight and damping of a typical MRF is demonstrated to contribute considerably to the hybrid testing accuracy, using the proposed test matrix. This observation emphasizes the importance of real-time testing to preserve higher order dynamics even for conventional structural members, not to mention more advanced vibration mitigation devices that are highly rate-dependent.

CHAPTER 8
MULTIPLE FLOORS MRF EXPERIMENT

The next validation experiment utilizes a two floors MRF specimen shown in Figure 8.1. One actuator is attached at each floor to apply the corresponding motion boundary conditions. This experimental setup represents a more generalized RTHS configuration because multiple actuators are now dynamically coupled through the steel frame.

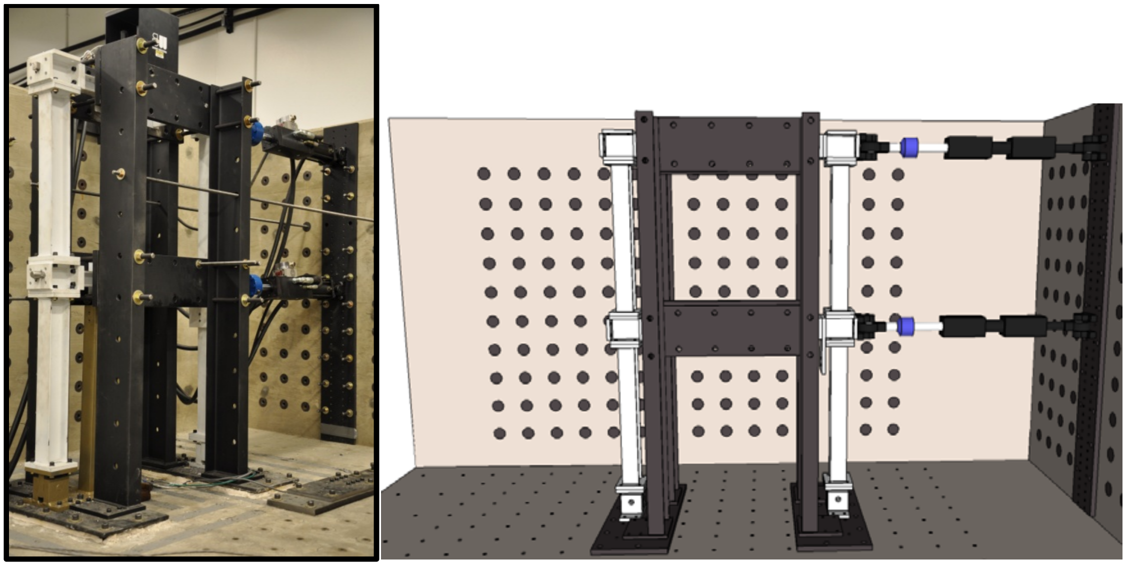

Figure 8.1 Multiple Floors MRF Experimental Setup

Few publications so far within the RTHS community have reported testing on a continuous physical frame structure that involves multiple coupled actuators. There are applications [(Christensen, Lin, Emmons, & Bass, 2008), (Chen, Ricles, Karavasilis, Chae, & Sause, 2012)] in which multiple specimens are virtually coupled between nodes on the numerical substructure. However, each physical substructure component is tested separately. Therefore, the boundary condition can be applied through individual actuator using any developed SISO motion control strategy. (Bonnet, et al., 2007) successfully performed RTHS in which multiple physical lumped mass and spring components are tested using multiple actuators. However, each actuator is treated as a separate SISO plant to design the outer-loop controllers, instead of modeling the entire plant as a MIMO system. (Phillips & Spencer, submitted) expanded the model based control strategy into a multivariable formulation, but only simulation results are reported with moderate coupling assumed. Conceptually the appearance of dynamic physical coupling raises control challenges dramatically, especially when the actuators loading capacity are not significantly greater than the specimen resistance. Herein the intuitive approach of compensating the dynamics of each individual actuator may not be very effective, when the physical coupling is not taken into consideration properly. A control algorithm for MIMO plant is therefore necessary for a generalized RTHS implementation, when two or more actuators are needed to accommodate more sophisticated experimental setup.

The H_∞ loop shaping strategy for multivariable control design is introduced first in this chapter. The identified MIMO plant model shows strong coupling that is also frequency dependent. The outer-loop control system is demonstrated both analytically and experimentally to be able to achieve decoupled displacement responses. A reduced order MRF stiffness matrix is identified to construct the analytical reference system. Finally, the RTHS validation experiments are conducted under several configurations, when the assumed numerical seismic mass are varied for each configuration.

8.1 Multivariable H_∞ Control Design

The proposed H_∞ strategy in Chapter 6 can naturally be extended into a multivariable formulation. Given the vector inputs *U(s)* and outputs *Y(s)* governed by the dynamic plant *G(s)*.

$$Y(s) = G(s)U(s) \tag{8.1}$$

where the input/output is represented by its associated Euclidean norm (Goodwin, Graebe, & Salgado, 2000) as

$$\begin{aligned} \|u\| &= \sqrt{|u_1|^2 + |u_2|^2 + \ldots + |u_n|^2} = \sqrt{u^* u} \\ \|y\| &= \sqrt{|y_1|^2 + |y_2|^2 + \ldots + |y_n|^2} = \sqrt{y^* y} \end{aligned} \tag{8.2}$$

The input output gain relationship can thus be defined as the infinity norm (i.e. maximum singular value) of the plant transfer function matrix as follows:

$$\|G\|_\infty = \sup_{\|u\|\neq 0} \frac{\|Y\|}{\|U\|} = \sup_{\|u\|\neq 0} \frac{\|GU\|}{\|U\|} = \sup_{\|u\|\neq 0} \frac{\sqrt{U^* G^* G U}}{\sqrt{U^* U}} = \sqrt{\lambda_{\max}\{G^* G\}} \tag{8.3}$$

The design strategy in Chapter 6 can now be applied to shape the infinity norm (loop gain) of the open-loop system for a chosen frequency range. The plant experimental transfer functions are obtained from the input commands to the output measured displacements, as shown in Figure 8.2.

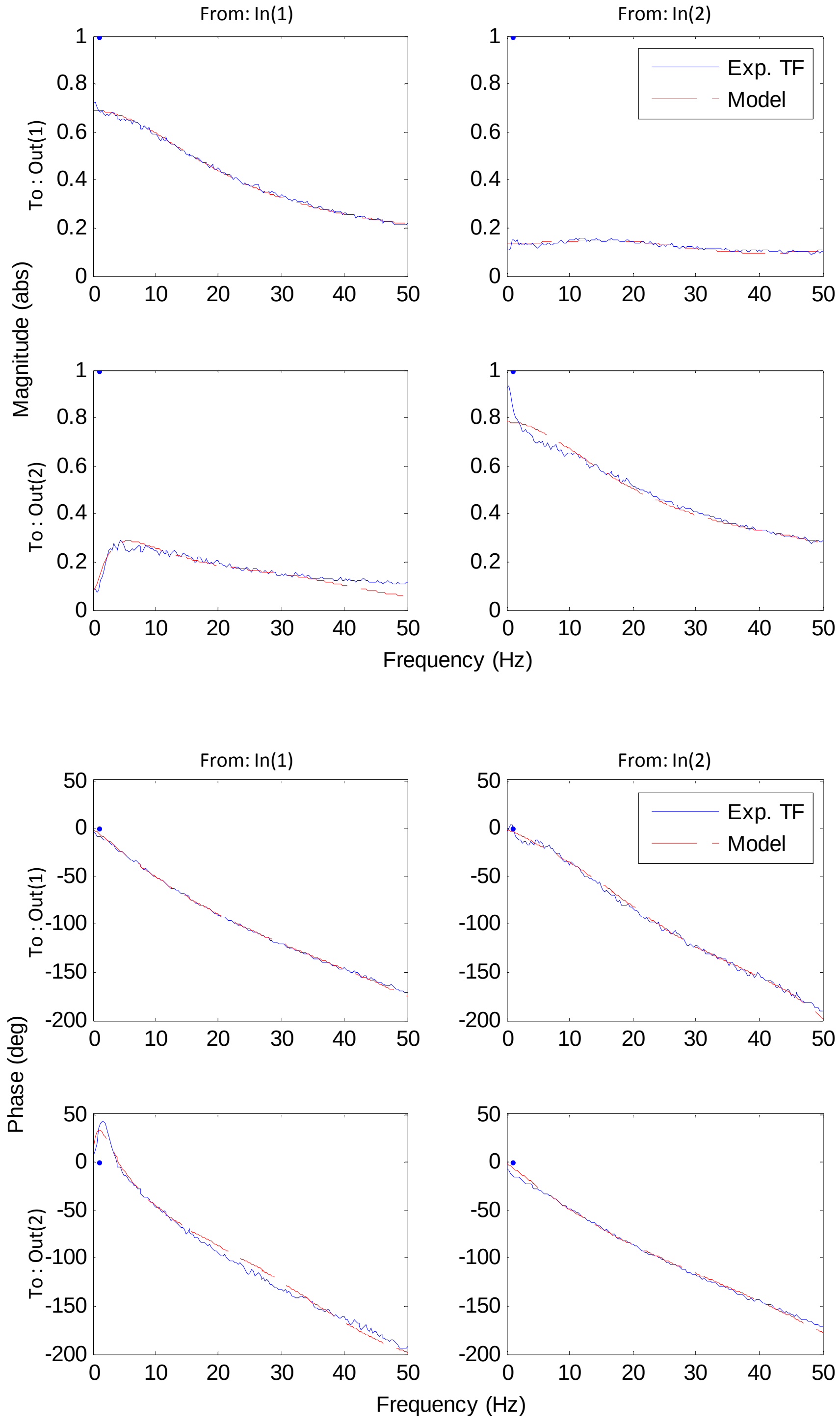

Figure 8.2 Displacement Transfer Functions with Two Floors MRF Specimen

The 1^{st} column of the transfer matrix is obtained when zero displacement is sent to the top floor actuator, while the bottom floor actuator is commanded by a white noise of 0.02" RMS amplitude and a bandwidth of 0-100Hz. Similarly, the 2^{nd} column is obtained by commanding the same white noise displacement to the top actuator but zero to the bottom actuator. Clearly the off-diagonal transfer function magnitude terms are not zero which indicates the existence of coupling. The MRF used in this study is very stiff compared to the relatively small actuators force capacity. Therefore, the coupling is observed to be very significant (about 15-25% in average) and appears to be frequency dependent. The plant model given in equation (8.4) is identified by curve-fitting each of the individual experimental transfer functions. Four poles are assumed for the plant that appears to be sufficient to capture the essential system dynamics. No zeros is assumed for all transfer functions except one that is needed for the $G_{21}(s)$ entry, to capture the magnitude ramp-up and phase lead between 0-10Hz. Note that the transfer function matrix is not symmetric, which is a violation of the actuator model assumed in Chapter 4. Therefore, a generalized control design procedure is needed for a high fidelity RTHS implementation, even when a minimum knowledge about the plant physics is available. Excellent comparison is observation between the experimental data and the plant model in Figure 8.2. The identified plant equation (8.4) is thus used to design the H_∞ controller.

$$G(s) = \begin{bmatrix} G_{11}(s) & G_{12}(s) \\ G_{21}(s) & G_{22}(s) \end{bmatrix} \tag{8.4}$$

where

$$G_{11}(s)=\frac{2.83e9}{s^4+5.77e2s^3+2.73e5s^2+6.05e7s+4.1e9}$$
$$G_{12}(s)=\frac{3.55e8}{s^4+2.75e2s^3+1.57e5s^2+2.37e7s+2.6e9}$$
$$G_{21}(s)=\frac{1.33e6s+5.35e6}{s^4+2.77e2s^3+7.7e4s^2+4.95e6s+7.15e7}$$
$$G_{22}(s)=\frac{3.55e9}{s^4+6.57e2s^3+2.73e5s^2+6.62e7s+4.54e9}$$

One of the main control design objectives in this chapter is to decouple the outer-loop system to its maximum extent. Therefore, the off-diagonal terms in the target open-loop shape are set to zero in equation (8.5). The diagonal terms are chosen as a trade-off between tracking requirements, i.e. high gains are designed over the desired performance bandwidth, and the robust stability requirement, i.e. low gains are designed where larger uncertainties may appear in the physical plant. The target loop shape for this specific experimental setup is chosen to be

$$G_d(s)=\begin{bmatrix}\frac{2.37e5}{s^2+628.3s+3948} & 0\\ 0 & \frac{2.37e5}{s^2+628.3s+3948}\end{bmatrix} \tag{8.5}$$

The designed controller *H(s)* is fairly complex with a total of 31 dynamical states. Most states are only mathematically traceable that do not have physical meaning. A pole-zero map of the designed controller is shown in Figure 8.3. Some of the poles are far beyond the system Nyquist frequency when digitally implementing the controller at 1024 Hz. The controller is thus converted into the discrete-time form using bilinear transformation.

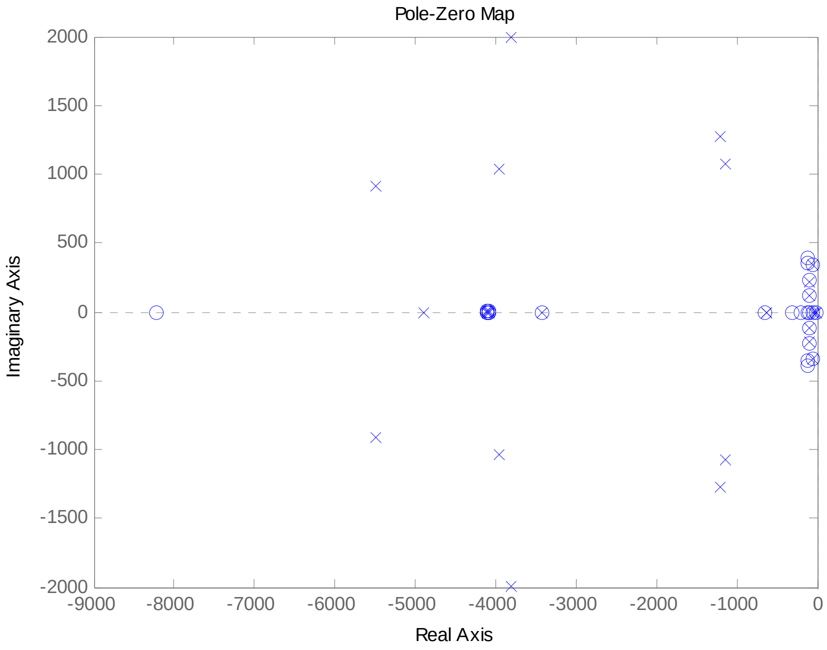

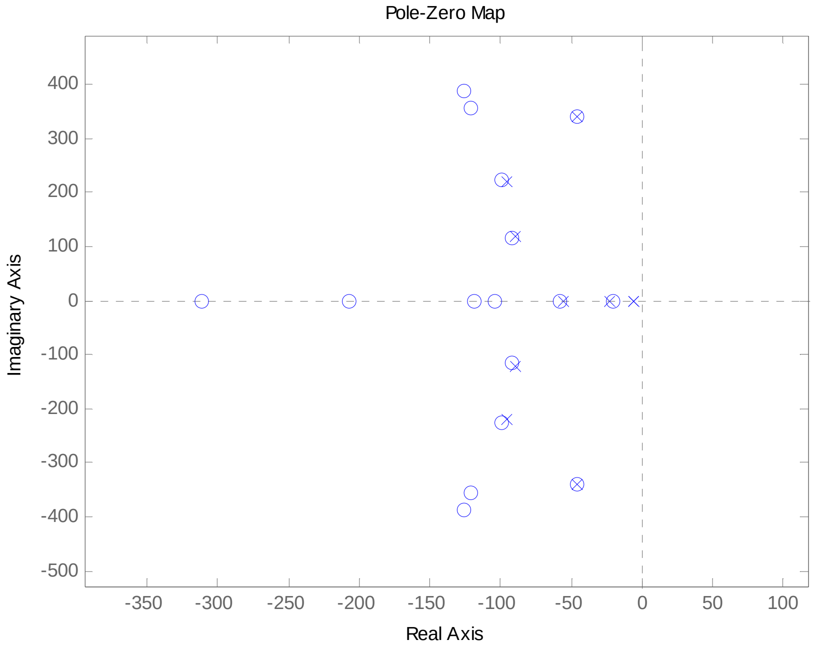

Figure 8.3 Pole-Zero Map of the H_∞ Controller

A 2nd order Butterworth low-pass filter $F_s(s)$ with a cutoff frequency of 50Hz is applied in this design for both floors measured displacements. Similarly as discussed in Chapter 6, this filter design is first to filter out the high frequency measurement noise to facilitate practical implementation; and to further enhance the phase tracking performance. The outer-loop system displacement transfer function matrix is shown as solid lines in Figure 8.4, after the H_∞ controller is applied. The plant model (dotted line) is included too for comparison purposes. It is clear from the magnitude plot that the outer-loop system off-diagonal coupling terms are minimized to nearly zero within 0-20Hz. The diagonal DC gains are also brought much closer to unity, as desired. The magnitude slightly deteriorates as the frequency increases due to the artificial mode introduced by the control design that is discussed thoroughly in Chapter 6. The influence of this artificial mode (at around 35Hz) on the closed-loop RTHS system will be discussed later in Figure 8.10 and Figure 8.11. The phase diagonal plots show that the outer-loop system lag is significantly reduced to nearly zero for both actuators. The influence of the relatively large off-diagonal phase lead terms is not a major concern here because their corresponding magnitude responses are minimal.

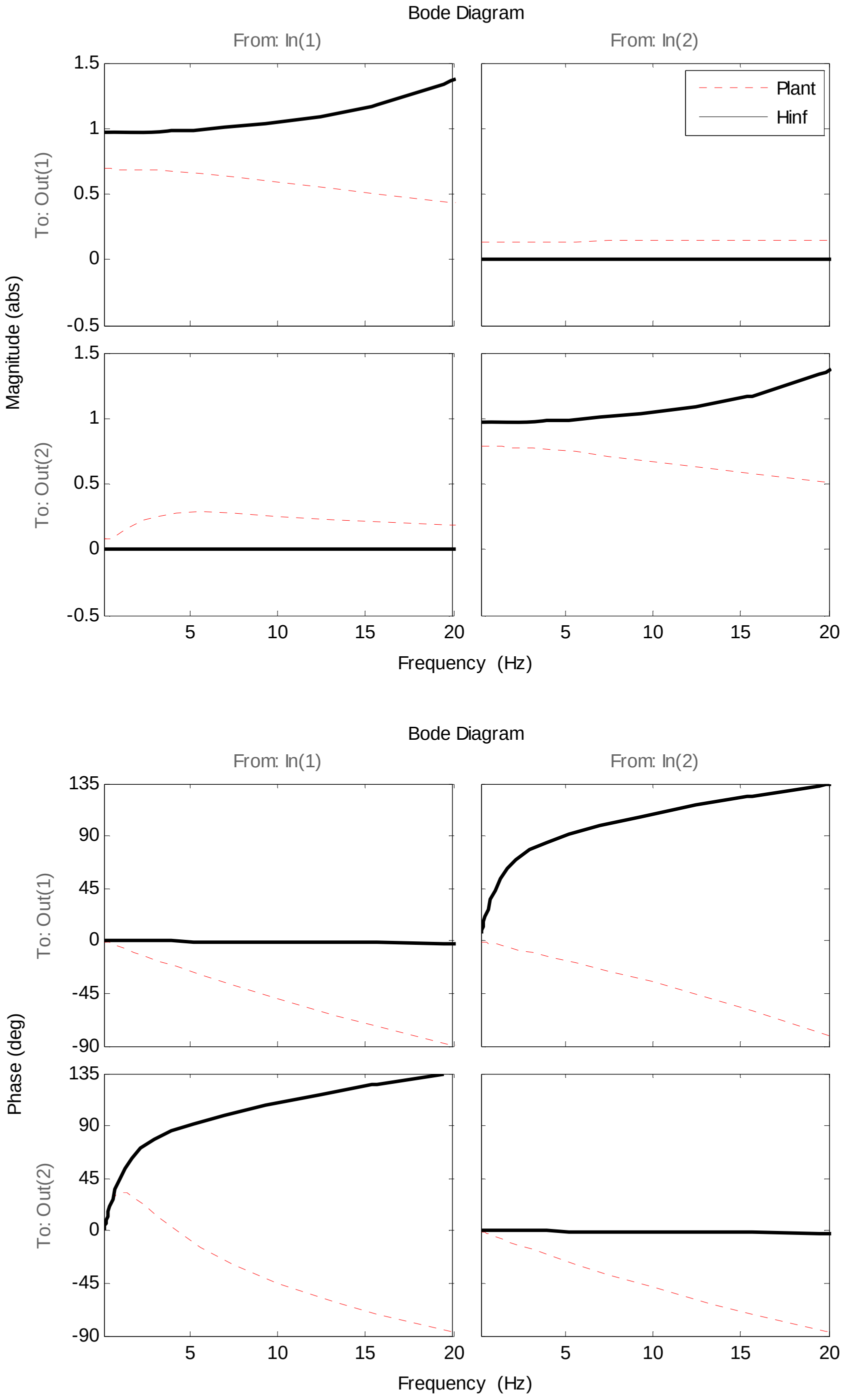

Figure 8.4 H_∞ Control System Displacement Transfer Functions with Two Floors MRF Specimen

Time domain experimental results are evaluated next to verify the designed controller tracking performance. Two chirp signals that span 0.1-10Hz are commanded to the actuators with an amplitude of 0.03” at floor 1 and 0.06” at floor 2. It can be observed in Figure 8.5 that the H_∞ controller does significantly improve the tracking performance compared to the PID control, in terms of amplitude and phase on both floors.

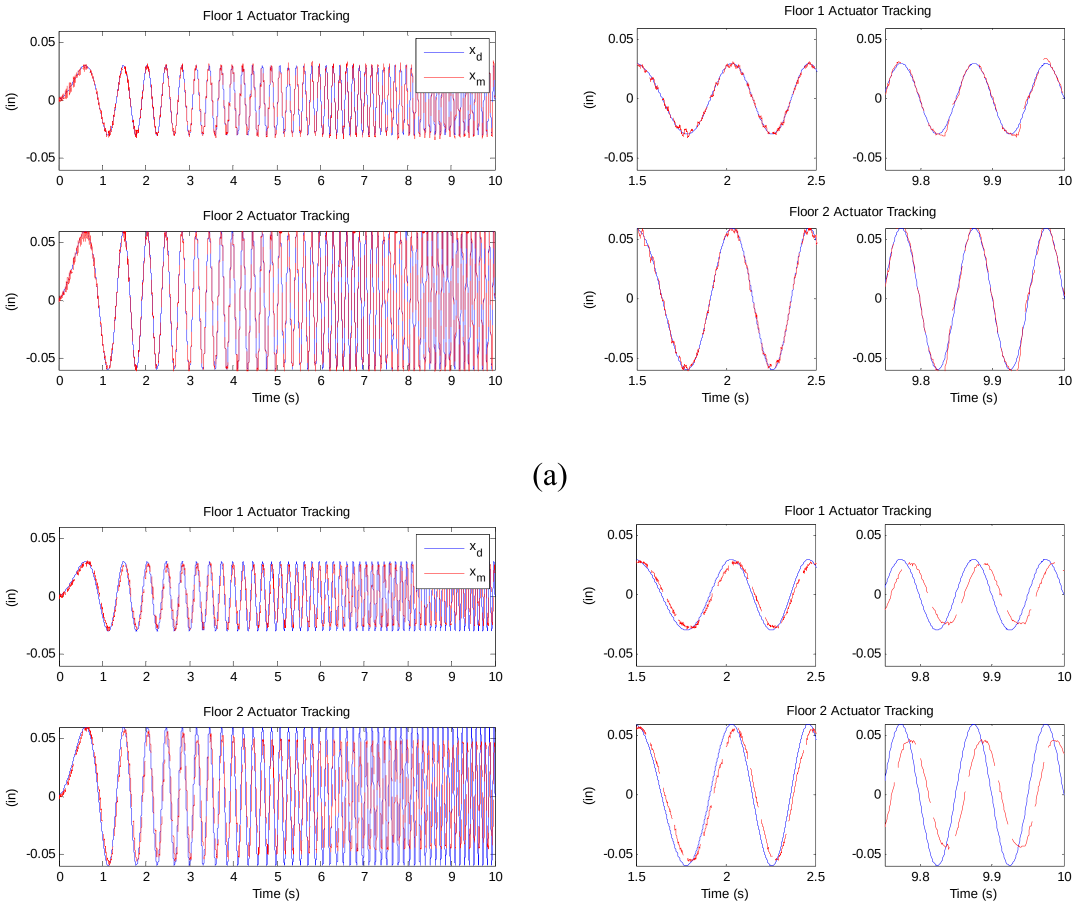

(a)

(b)

Figure 8.5 Actuator Tracking Experiment with Two Floors MRF Specimen
(a): H_∞ control; (b): PID control

The normalized RMS tracking error on both floors are evaluated by equation (4.9) that are listed in Table 8.1. Tracking errors are reduced by nearly one order of magnitude using the H_∞ controller as compared to the results with only the PID controller, which demonstrates the effective of the proposed control design strategy.

Table 8.1 Actuator Tracking Error with Two Floors MRF Specimen

	H_∞ controller	PID controller
E_T (Floor 1)	7.41	45.9
E_T (Floor 2)	5.99	49.43

8.2 MRF Stiffness Matrix Identification

The stiffness of the MRF specimen is identified in this section to interpret the RTHS results. Identification of the stiffness matrix uses acceleration outputs, one on each floor. Two types of dynamic identification procedures are conducted by applying a force input at the top floor of the frame. The 1st procedure uses a hammer test on the top floor to acquire the transient responses of the frame, when no actuator is attached on either floor. The Fourier transform of the acceleration responses are shown in Figure 8.6. The 2nd procedure attaches only the top floor actuator and commands a white noise of 0.01” RMS amplitude and a bandwidth of 0-500 Hz. The bottom floor actuator is removed from the frame. Transfer functions from the input force to output accelerations are shown in Figure 8.7. It is observed that the first two dominant modes of the MRF are captured by both identification procedures.

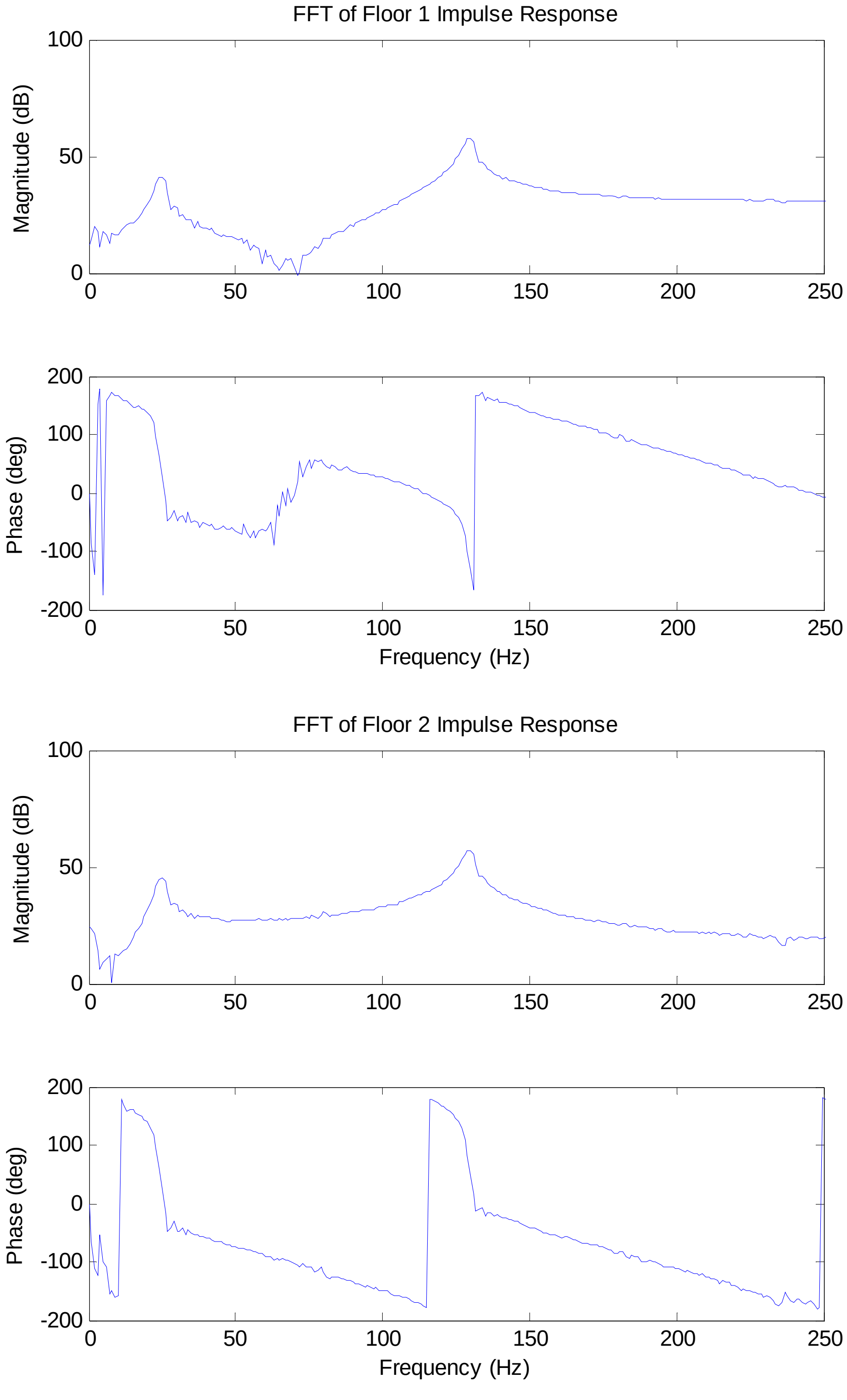

Figure 8.6 Transfer Function from the Top Floor Impulse Force to Both Floors Acceleration

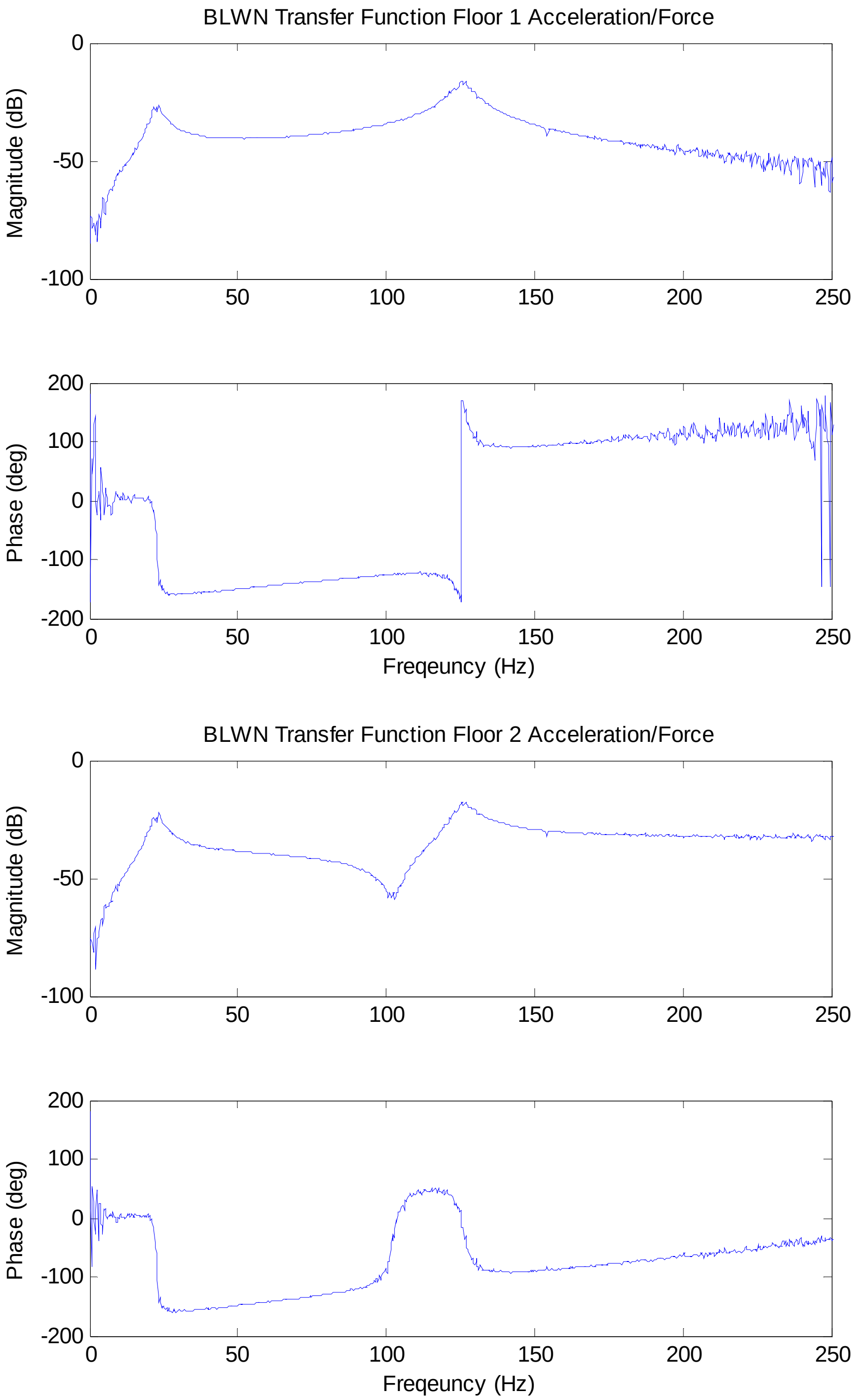

Figure 8.7 Transfer Function from the Top Floor BLWN Force
to Both Floors Acceleration

The eigensystem realization algorithm [(Juang & Pappa, 1985), (Juang, 1994), (Giraldo, Yoshida, Dyke, & Giacosa, 2004)] is subsequently used to construct a dynamic realization of the MRF specimen. The identified modal parameters from the ERA include the first two dominant natural frequencies and their associated mode shapes, which are shown in Table 8.2. Slightly decreased natural frequencies are observed in the BLWN test due to the contribution of additional actuator mass on the top floor.

Table 8.2 ERA Identified MRF Modal Parameters

	Natural Frequency (Hz)	1st mode shape	2nd mode shape
Impulse Test	24.68	0.42	1
	129.03	1	-0.94
BLWN Test	22.58	0.67	1
	126.02	1	-0.85

The ERA procedure described above yields a mathematical realization of the system that does not necessarily have physically meaningful state variables. A constrained nonlinear optimization algorithm is then used to update the numerical stiffness by minimizing the objective function (Zhang, Sim, & Spencer, 2008).

$$\min_k \left(\sum_i \left\| f_i(k) \right\| \right) \tag{8.6}$$

where

$$f_i(k) = \alpha\left(1 - MAC(\Phi_{id,i}, \Phi_{num,i}(k))\right) + \beta \left\| \frac{\omega_{id,i} - \omega_{num,i}(k)}{\omega_{id,i}} \right\|$$

$$MAC = \frac{\left(\Phi_{id,i}^T \Phi_{num,i}\right)^2}{\left(\Phi_{id,i}^T \Phi_{id,i}\right)\left(\Phi_{num,i}^T \Phi_{num,i}\right)}$$

here *k* is the vector of parameters to be updated e.g. the reduced order 2x2 MRF stiffness matrix; α and β are weighting constants for the mode shapes (Φ) and the natural frequencies (ω); MAC is the modal assurance criteria between the identified *i*-th mode shape ($\Phi_{id,i}$) from the ERA procedure and the *i*-th mode shape of the numerical model ($\Phi_{num,i}$). The updated MRF dynamic stiffness matrix is:

$$K_d = \begin{bmatrix} k_{d,1} & k_{d,2} \\ k_{d,2} & k_{d,3} \end{bmatrix} = \begin{bmatrix} 80.73 & -49.23 \\ -49.23 & 35.10 \end{bmatrix} (kip/in) \qquad (8.7)$$

A quasi-static push-over tests is conducted as a 3rd identification/verification procedure. The experimental observations indicate that it is advisable to attach only one actuator at a time while keeping the other removed from the MRF specimen. This procedure is essential to keep the MRF boundary conditions simple and to remove the physical force coupling between multiple actuators. The force coupling phenomenon is not clearly understood so far, based on the existing mathematical models found in the literature. A predefined quasi-static displacement trajectory in Figure 8.8 is applied on each floor at a time. The experimental identified condensed stiffness are K_1=10.64 kip/in for the 1st floor, and K_2=4.75 kip/in for the 2nd floor, as shown in Figure 8.9.

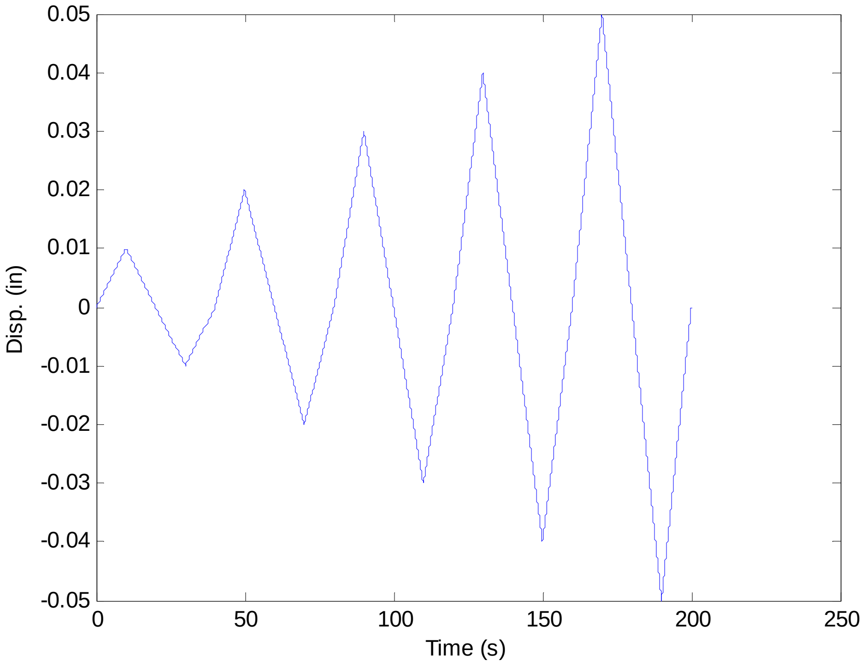

Figure 8.8 Quasi-Static Test Displacement Trajectory

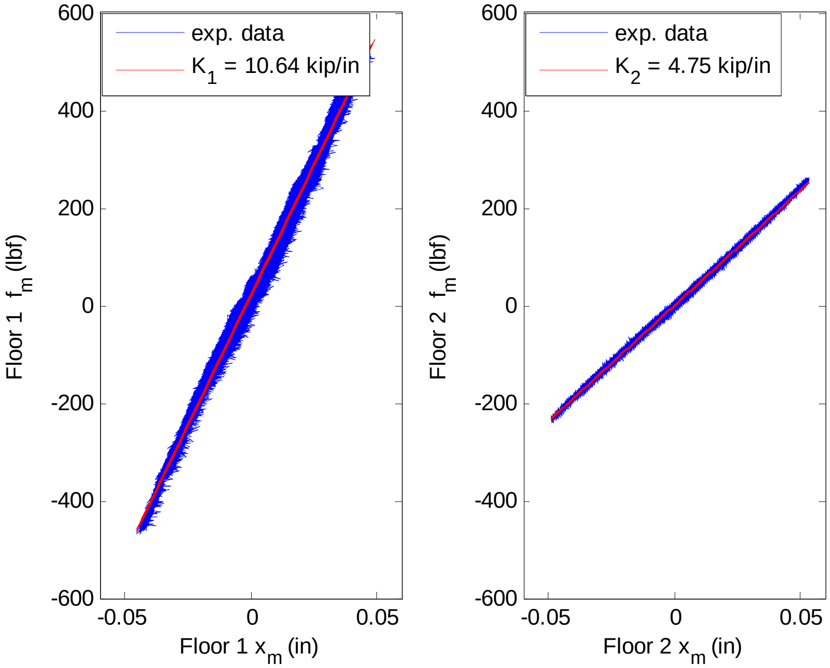

Figure 8.9 Identified Condensed MRF Stiffness

To solve for all three unknowns in the condensed stiffness matrix, one more constraint is added to enforce the static stiffness matrix Frobenius norm to be the same as the one identified from the dynamic procedures in equation (8.7).

$$\begin{aligned} k_{s,1} - k_{s,2}^2 / k_{s,3} &= K_1 \\ k_{s,3} - k_{s,2}^2 / k_{s,1} &= K_2 \\ k_{s,1}^2 + k_{s,2}^2 + k_{s,3}^2 &= k_{d,1}^2 + k_{d,2}^2 + k_{d,3}^2 \end{aligned} \tag{8.8}$$

The identified static stiffness matrix is thus obtained by solving equation (8.8) to be

$$K_s = \begin{bmatrix} k_{s,1} & k_{s,2} \\ k_{s,2} & k_{s,3} \end{bmatrix} = \begin{bmatrix} 79.9 & -49.7 \\ -49.7 & 35.7 \end{bmatrix} (kip/in) \tag{8.9}$$

8.3 RTHS Validation Experiments

The experimental validation procedure in this section focus on the worst-case RTHS scenario discussed in Chapter 3, where the mass is primarily assumed computationally but the stiffness is largely included physically. In practice 1% of K_s is assumed in the numerical substructure to avoid the mathematical singularity issue. A series of validation tests are configured by varying the computational mass on both floors, as shown in Table 8.3. The input El-Centro earthquake intensity is scaled for each configuration, to accommodate the response magnitude that is limited by the actuator force and displacement constraints. The reference structure assumes Rayleigh damping of 2% for the first two modes in each configuration. Note that the reference system natural frequencies in Table 8.4 increase as the mass reduce. Configuration 4 poses more experimental challenges because: 1) it demands the actuator to track a higher frequency response signal; 2) the physical substructure represents a larger portion that is primarily the source of the RTHS error. The 2nd mode progressively approaches the RTHS system stability limit, as the mass reduce. The physical MRF specimen mass are 0.18 lb-s^2/in (31.5 kg) on the 1st floor and 0.16 lb-s^2/in (24.7 kg) on the 2nd floor, which are negligible compared to the assumed numerical mass. The Rayleigh damping ratios of the MRF specimen are assumed to be 7.5% and 1% for the 1st and 2nd mode, respectively. Note this damping assumption is an approximation for the continuum frame, which is a tentative approach to partially account for the damping contribution from the hydraulic actuators. The physical MRF mass and damping are subtracted from the numerical substructure to maintain the same amount of total structural properties between the reference and RTHS system, in a similar way as discussed in Chapter 7.

Table 8.3 Validation Experiments Mass Configuration

	Config. 1	Config. 2	Config. 3	Config. 4
m_1(kg)	8000	4000	4000	2000
m_2(kg)	8000	4000	2000	2000
Eq. Intensity	0.07	0.1	0.15	0.15

Table 8.4 Validation Experiments Reference Structural Modes

	Config. 1	Config. 2	Config. 3	Config. 4
1st mode (Hz)	1.38	1.95	2.41	2.75
2nd mode (Hz)	7.92	11.21	12.79	15.85

The closed-loop RTHS system transfer functions, from the input earthquake acceleration to output desired displacements, are compared with that of the reference system in Figure 8.10 and Figure 8.11. This frequency domain analysis procedure can help understand the RTHS system stability and accuracy before conducting an online test.

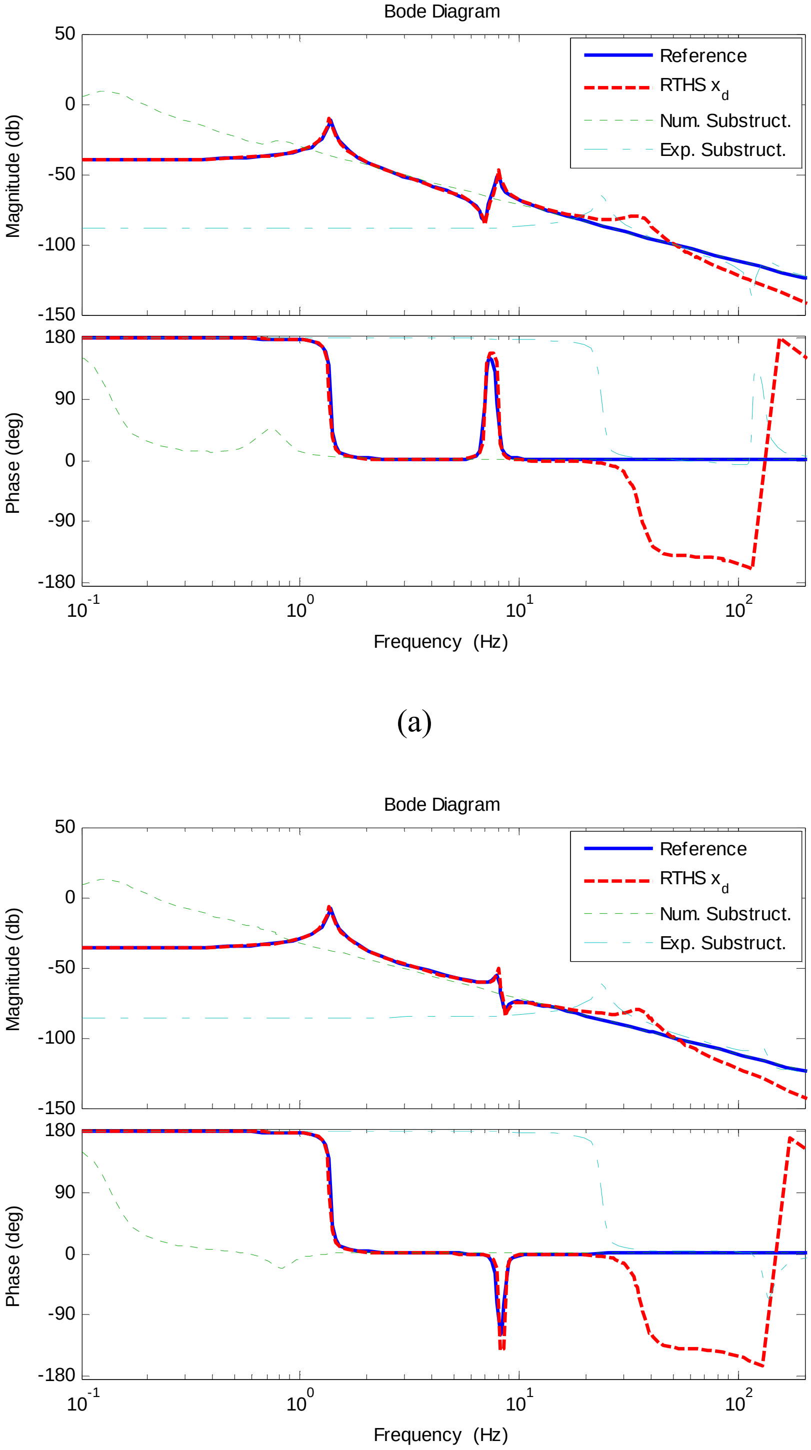

(a)

(b)

Figure 8.10 RTHS System Transfer Functions from Input Earthquake to Floor Displacements (Config. 1) (a): Floor 1; (b): Floor 2

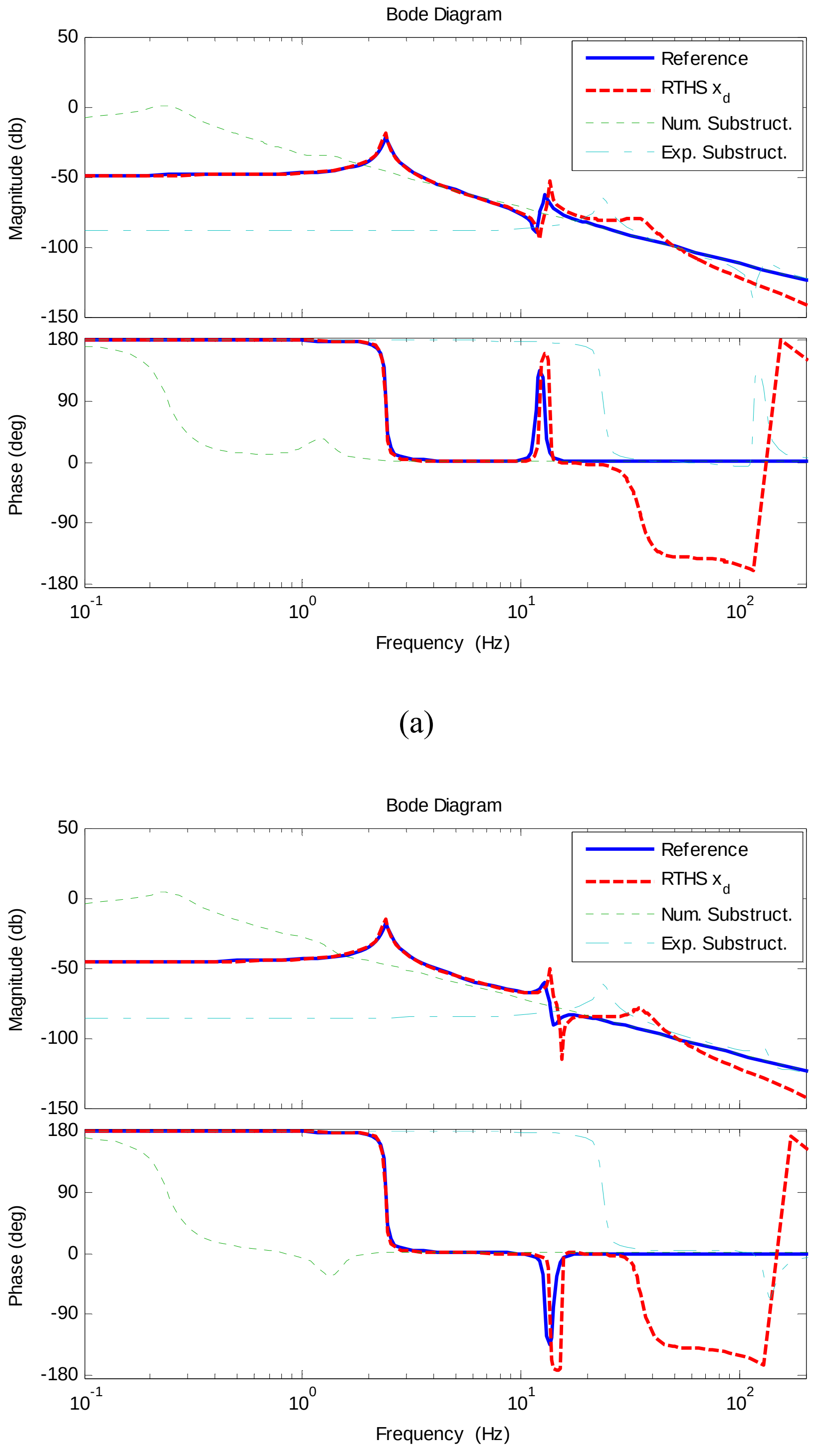

(a)

(b)

Figure 8.11 RTHS System Transfer Functions from Input Earthquake to Floor Displacements (Config. 3) (a): Floor 1; (b): Floor 2

It is observed in Figure 8.10 (configuration 1) that the RTHS system agrees very well with the reference system until about 20Hz, which includes both structural modes. An artificial mode appears in the RTHS system at around 35Hz that is caused by the low-pass filter design in the H_∞ motion controller design. The numerical and experimental substructure transfer functions are shown in the same graph too, to gain a better insight about the proposed worst-case substructure partition. It is obvious that the numerical substructure is very flexible with a significant seismic response due to the large mass and small stiffness assumption. Oppositely, the physical MRF has a large stiffness but a small mass. The experimental substructure modes appear at quite high frequencies, without considering the tributary mass as in a standard structural configuration. Its transfer function magnitude is therefore very small. The deviation between the reference and the RTHS system becomes large at frequencies above 20Hz. The designed performance bandwidth of the H_∞ motion controller for this experimental setup is about 20 Hz, above which test instability is likely to occur.

Figure 8.11 shows the transfer function comparisons for configuration 3. The reference system modes are higher than the ones in configuration 1 due to the reduced mass assumption. Note that the slightly deteriorated actuator tracking performance between 10-20 Hz, shown in Figure 8.4, causes a significantly magnified RTHS system error. This system error is especially obvious near the 2nd mode of the reference system (at 12.79 Hz). This observation demonstrates again that the selected sub-structuring scheme is very sensitive to the actuator tracking error. A high quality motion controller is thus necessary for this type of RTHS implementation. The RTHS system instability occurs as the computational mass reduces even further, when the 2^{nd} mode of the reference system is higher than 20 Hz.

The proposed test matrix in Table 8.3 is validated experimentally and the displacement responses on both floors are evaluated. All tests are conducted in real-time with a sampling rate of 1024 Hz. The H_∞ controller is transformed into a discrete form using a bilinear transformation. Note that the reference structure here is the updated full finite element model that comprises of beam, column and panel zone elements. Additional rotational springs are assumed between element interfaces to characterize the flexibility introduced by various joints and connection bolts. Extensive numerical validation procedures have been conducted to demonstrate the modeling accuracy of RT-Frame2D (Castaneda, 2012). The full model responses herein are also compared with the ones obtained from the reduced order model in equation (8.9), both of which yield closely converged results. The numerical integration of the EOM is evaluated using the CR integrator for all tests. Figure 8.12 to Figure 8.15 show the comparison of the reference structural responses with the RTHS results. The RTHS desired displacements from the numerical substructure is used to evaluate the RTHS error. The actuator tracking performance is presented in the bottom-right subplot for all tests, where the desired displacement is compared against the measured displacement.

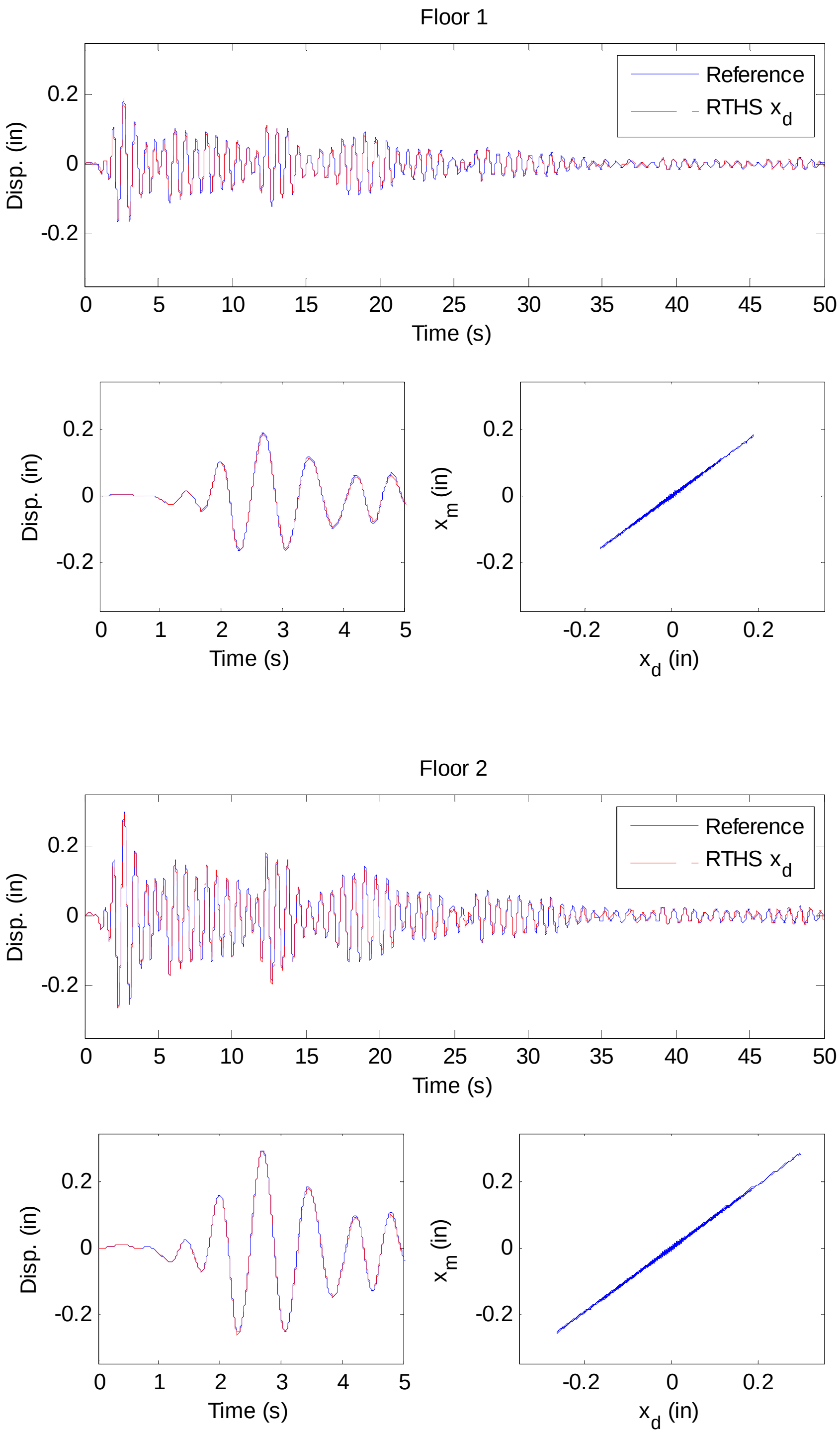

Figure 8.12 RTHS Experiment with Two Floors MRF Specimen (Config. 1)

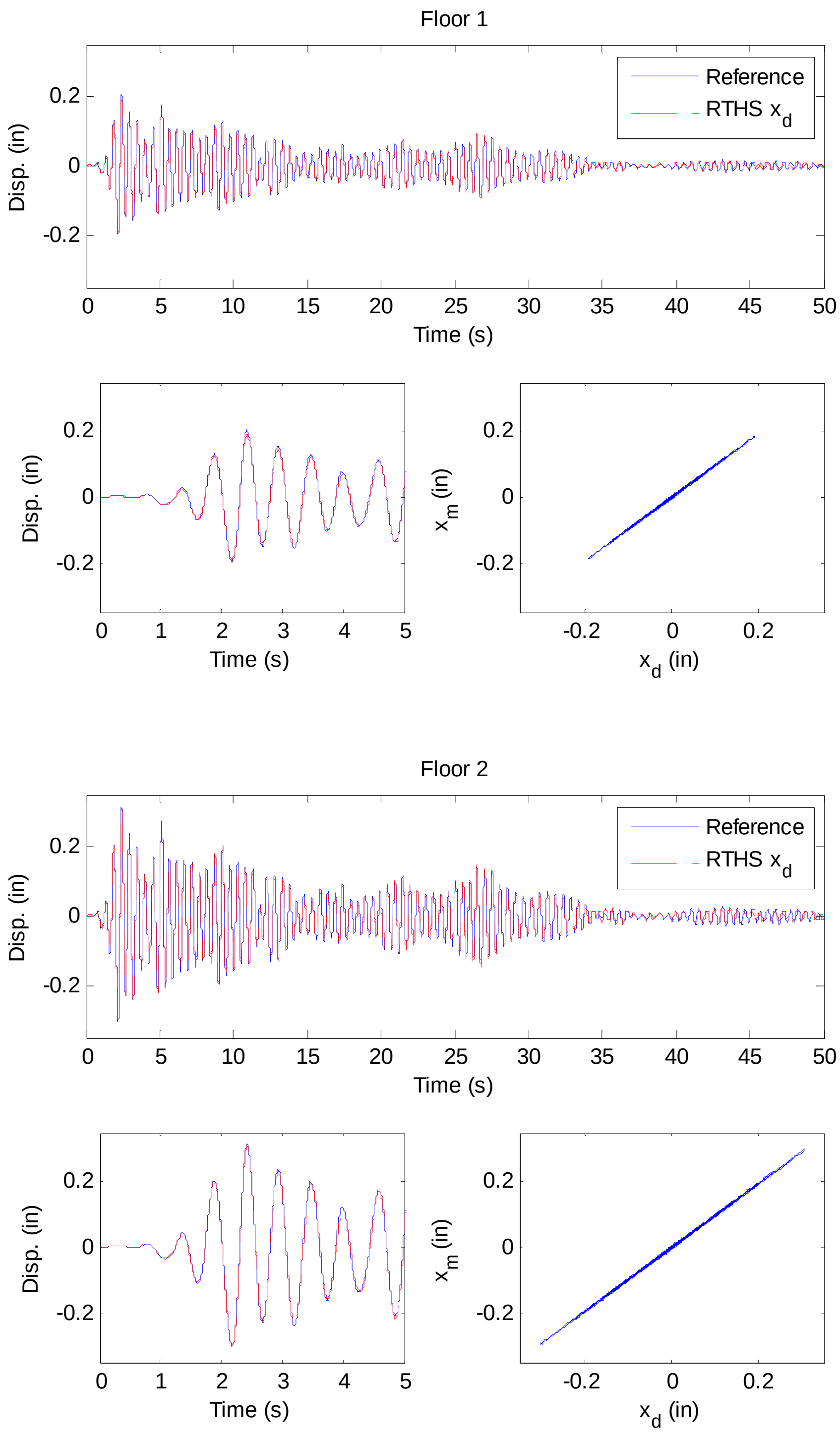

Figure 8.13 RTHS Experiment with Two Floors MRF Specimen (Config. 2)

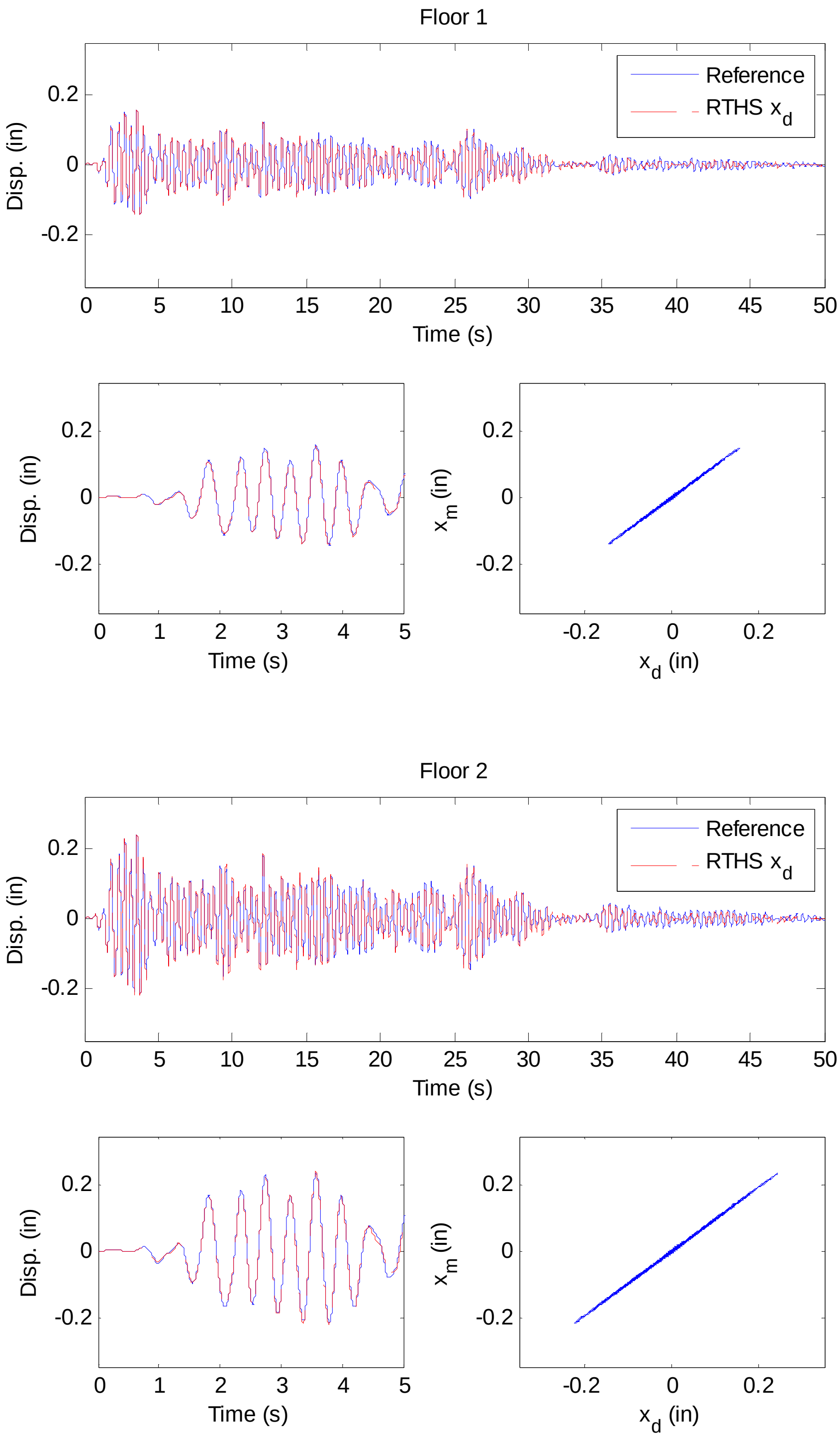

Figure 8.14 RTHS Experiment with Two Floors MRF Specimen (Config. 3)

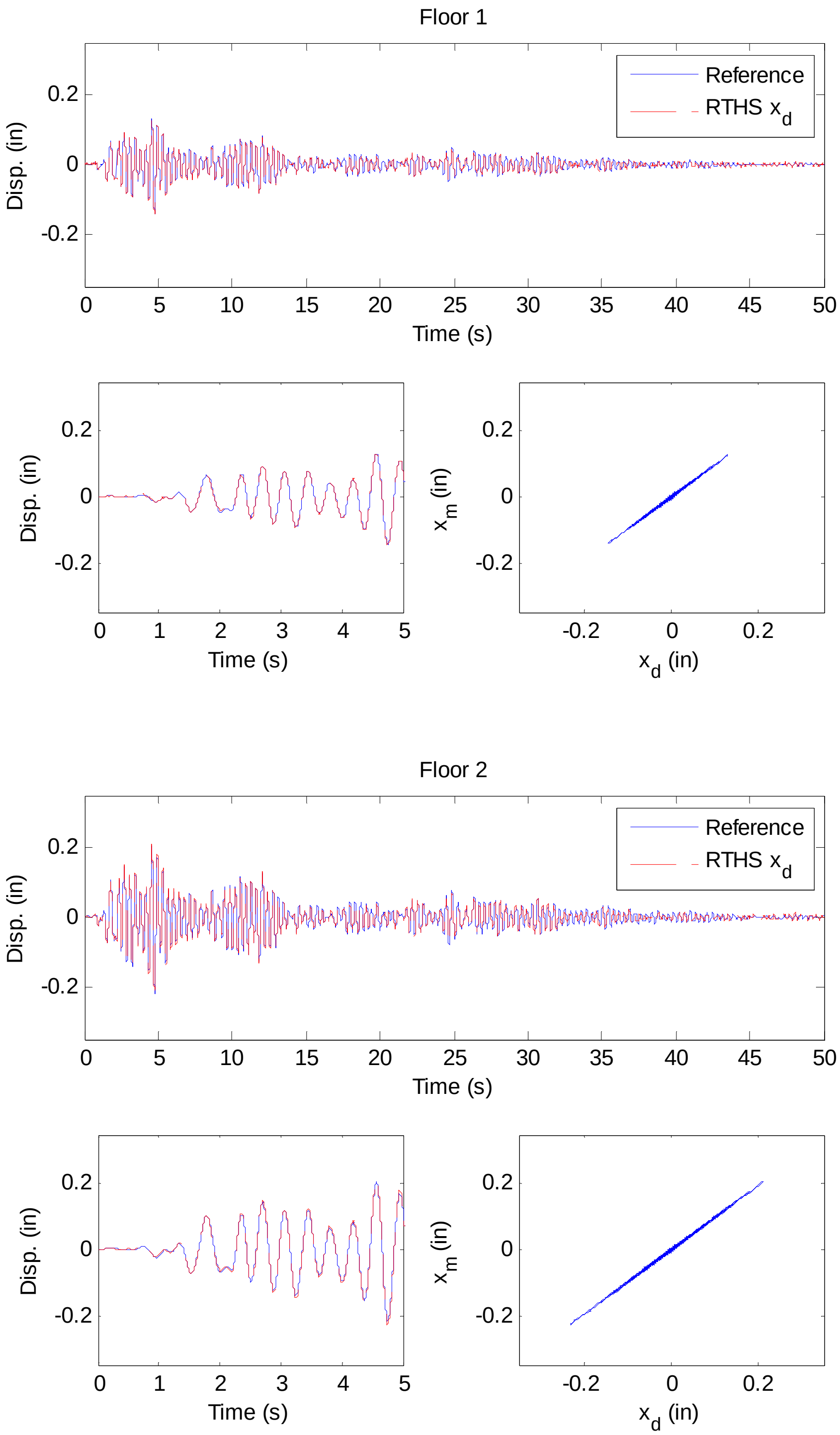

Figure 8.15 RTHS Experiment with Two Floors MRF Specimen (Config. 4)

It can be observed from Figure 8.12 to Figure 8.15 that all RTHS results compare very well to the reference structural responses on both floors, under all mass configurations. The bottom right subplot on each figure shows a nearly straight 45 degree line between the desired and the measured displacement, indicating good actuator tracking performance during the entire time history. The normalized RTHS error and actuator tracking error for all tests are summarized in Table 8.5. Consistent good performance is observed for all test configurations.

Table 8.5 Experimental Error with Two Floors MRF Specimen (%)

	Config. 1	Config. 2	Config. 3	Config. 4
E_{RTHS} (Floor 1)	12.88	12.04	19.03	17.74
E_{RTHS} (Floor 2)	11.82	11.15	18.98	17.25
$E_{Tracking}$ (Floor 1)	5.11	4.14	4.35	7.71
$E_{Tracking}$ (Floor 2)	4.03	3.25	3.28	4.98

A pure numerical simulation of the RTHS is conducted using the same assumption of numerical and physical substructures. Simulated RTHS include the plant model in equation (8.4) and the designed H_∞ controller. These simulated RTHS results are compared with the reference structural responses and the errors are shown in Table 8.6. A very similar level of accuracy is observed compared with the experimental results in Table 8.5, which demonstrate the successful modeling and identification results. Instability occurs in both simulation and experiment if the mass is further reduced to 1500 kg per floor, when the 2nd structural mode exceeds the designed stability limit. This successful prediction demonstrates again that we've achieved component level understanding of the RTHS system dynamics.

Table 8.6 Simulated RTHS Error (%)

	Config. 1	Config. 2	Config. 3	Config. 4
E_{SIM_RTHS} (Floor 1)	16.52	21.54	18.70	15.76
E_{SIM_RTHS} (Floor 2)	16.51	21.56	18.74	15.73

8.4 Summary

A generalized RTHS procedure is described and experimentally validated in this chapter, which involves the challenges of multiple actuators dynamic coupling. The proposed H_∞ loop shaping motion control strategy can be naturally expanded to a MIMO system. Thus, it is very promising for generalized structural testing when more actuators are needed to apply sophisticated dynamic boundary conditions. An identification procedure is presented to obtain the MRF stiffness matrix accurately. Both the frequency domain analysis and time domain experimental results compare well with the reference structural responses, which demonstrate the effectiveness of the proposed control strategy for complex setup with strong coupling.

CHAPTER 9
RTHS TEST OF MR DAMPER CONTROLLED MRF

The proposed RTHS framework is further validated in this chapter to evaluate the performance of controllable damping devices, and its effectiveness in structural vibration mitigation. An MR damper [(Dyke, 1996),(Dyke, Spencer, Sain, & Carlson, 1996), (Spencer, Dyke, Sain, & Carson, 1997)] is a kind of semi-active control device that requires much less energy consumption to operate when compared to active control devices. An MR damper's operation is based on controllable MR fluids. MR fluids have the ability to change from a free-flowing, linear, viscous fluid condition to a semi-solid condition when exposed to a magnetic field.

The MR damper specimen used in this study is a LORD RD-8041-1 model that is 9.76" (24.8cm) long in its extended position with an operational stroke of 2.91" (7.4cm). The main cylinder has 1.66" (4.21cm) in body diameter, contains the MR fluid, the magnetic circuit and the shaft diameter of 0.39" (1cm). The tensile strength of the device is 2000 lb (8896 N) maximum. Specified peak to peak damper force is greater than 550 lb (2447 N) when subjected to a velocity of 1.97 in/sec (5 cm/sec) at 1 A current input. The safety operating temperature is 71^{o}C maximum. Input current should be restricted to 1 A for a continuous operation of 30 seconds or more and 2A for intermittent usage. A LORD Wonder Box device provides closed-loop current control that operates as an interface device for PLC or digital control of the MR damper. The output current with the Wonder Box will be 0.0 A when the control input is approximately 0.4-0.6 V, and is linearly proportional to the input voltage above. The maximum output current is 2 A with an appropriate current source.

9.1 Bouc-Wen Model Identification

There are many existing mathematical models for characterizing MR dampers [(Spencer, Dyke, Sain, & Carson, 1997), (Gavin, 2001), (Yang, Spencer, Jung, & Carlson, 2004),(Ikhouane & Rodellar, 2007)]. In this study, a phenomenological Bouc-Wen model (schematically shown in Figure 9.1) is used to model the damper mechanical property.

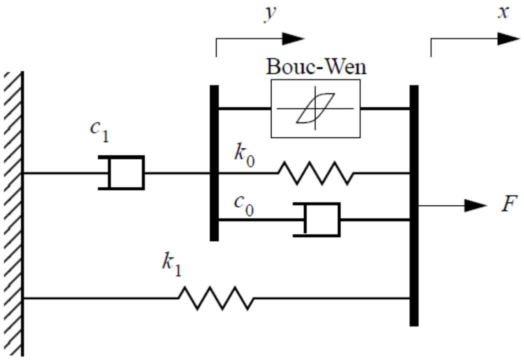

Figure 9.1 Phenomenological Bouc-Wen Model (after Dyke, 1996)

The force output of the MR damper is characterized by the following equation

$$F = \alpha(u)z + c_0(u)(\dot{x} - \dot{y}) + k_0(x - y) + k_1(x - x_0) \tag{9.1}$$

where the evolutionary variable *z* of the Bouc-Wen element is governed by:

$$\dot{z} = -\gamma|\dot{x} - \dot{y}|z|z|^{n-1} - \beta(\dot{x} - \dot{y})|z|^{n} + A(\dot{x} - \dot{y}) \tag{9.2}$$

The parameters β, γ, n and A control the shape of the hysteretic loop. In our particular application the damper switches only between two working conditions: either 0V or a maximum voltage of 3V is supplied by the current driver (effectively generating different strength magnetic fields on the damper fluid). The following simple linear functions are thus assumed to model the damper property variations with respect to this current change.

$$\alpha(u) = \alpha_{a} + \alpha_{b}u, c_{0}(u) = c_{0a} + c_{0b}u, c_{1}(u) = c_{1a} + c_{1b}u \tag{9.3}$$

The dynamics involved in the circuitry and MR fluid reaching rheological equilibrium are accounted for through a first order filter.

$$\dot{u} = -\eta(u - v) \tag{9.4}$$

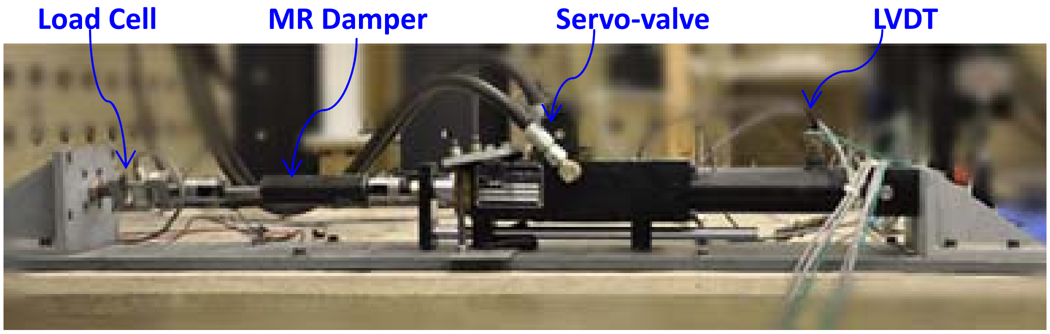

Figure 9.2 Experimental Setup for MR Damper Testing

A series of tests are conducted to measure the damper response under various loading conditions to identify the Bouc-Wen parameters. A 2.5 Hz sinusoidal displacement command with 0.2” amplitude is tested, when the damper is subjected to constant voltage of 0, 1, 2 and 3 V, respectively. Experimental setup for the MR damper testing is shown in Figure 9.2. Comparison between the experimentally measured responses (blue curves) and the identified Bouc-Wen model (colored curves) are presented in Figure 9.3, including the force time history, force-displacement and force-velocity hysteresis.

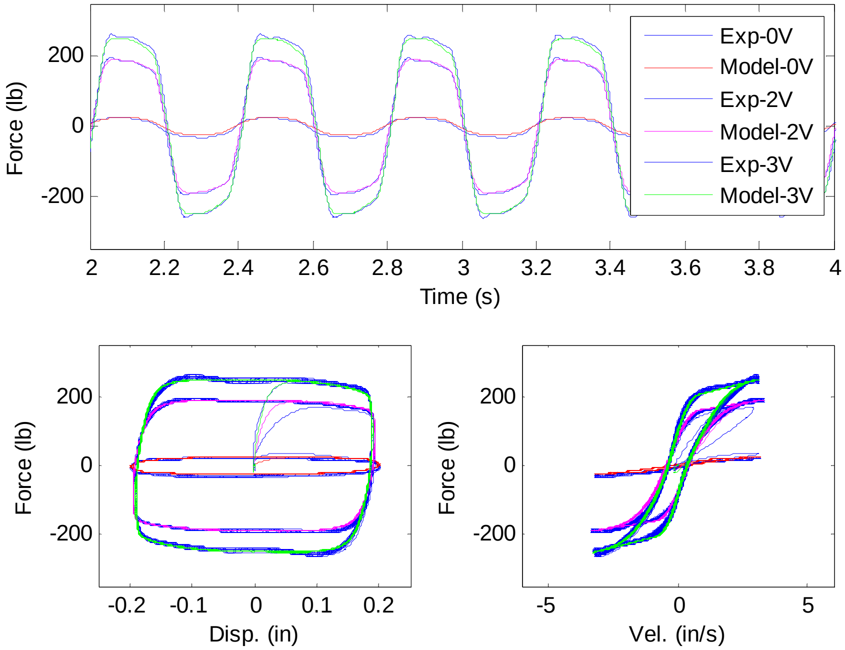

Figure 9.3 Bouc-Wen Model vs. Experimental Data

Table 9.1 Identified Bouc-Wen Model Parameters

Parameter	Value	Unit
α_a	10.97	lb/in
α_b	33.59	lb/in-V
c_{0a}	3.72	lb-s/in
c_{0b}	5.96	lb-s/in-V
c_{1a}	11.93	lb-s/in
c_{1b}	82.14	lb-s/in-V
k_0	11.08	lb/in
k_1	0.01	lb/in
γ	23.44	in^{-2}
β	23.44	in^{-2}
A	155.32	-
x_0	0.00	in
n	2	-
η	60.00	s^{-1}

It is observed that the damping device can provide a wide range of forces. Good comparison in Figure 9.3 at all voltages demonstrates that the Bouc-Wen model is very effective at capturing the damper's behavior. A nonlinear constrained optimization routine is then used to curve-fit experimental data to obtain the Bouc-Wen model parameters that are listed in Table 9.1.

The MR damper behavior changes dramatically when the device is subjected to different voltages. Transfer functions between the command and measured displacements are identified and listed in equation (9.5), when the damper voltage is set to be off (0 Volt) and on (3V) states, respectively.

$$\begin{aligned} G_{off}(s) &= \frac{2.81e9}{s^4 + 6.16e2s^3 + 2.67e5s^2 + 3{,}88e7s + 2.80e9} \\ G_{on}(s) &= \frac{1.74e9}{s^4 + 5.88e2s^3 + 2.58e5s^2 + 4.15e7s + 1.67e9} \end{aligned} \tag{9.5}$$

The H_∞ tracking controller herein is designed based on the plant $G_{off}(s)$. Otherwise if the design is based on $G_{on}(s)$, the shaped pre-compensator is more aggressive and the controller is likely to cause closed-loop system instability, when the voltage is turned off during run-time. Plant models along with the designed H_∞ outer-loop control systems are evaluated and shown in Figure 9.4, for both on and off states. The outer-loop system performance is excellent for the off state. Significantly improved performance is achieved for the on state as well, which demonstrates the outer-loop controller's robustness property. The plant dynamics at intermittent voltages are likely to fall into the bounds between on and off states. Therefore, the designed H_∞ controller is expected to be effective even when the MR damper is subjected to a continuous varying voltage.

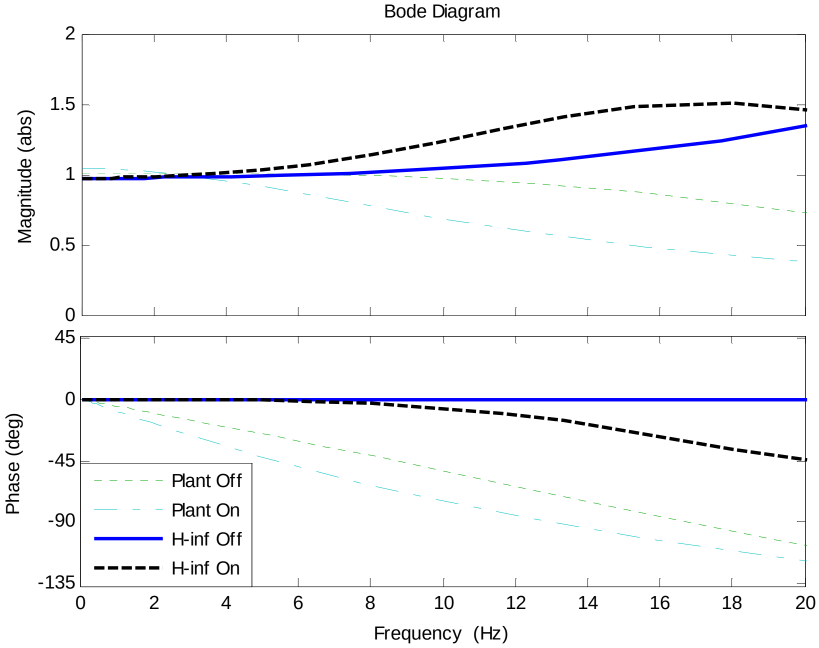

Figure 9.4 Displacement Transfer Function with MR Damper Specimen

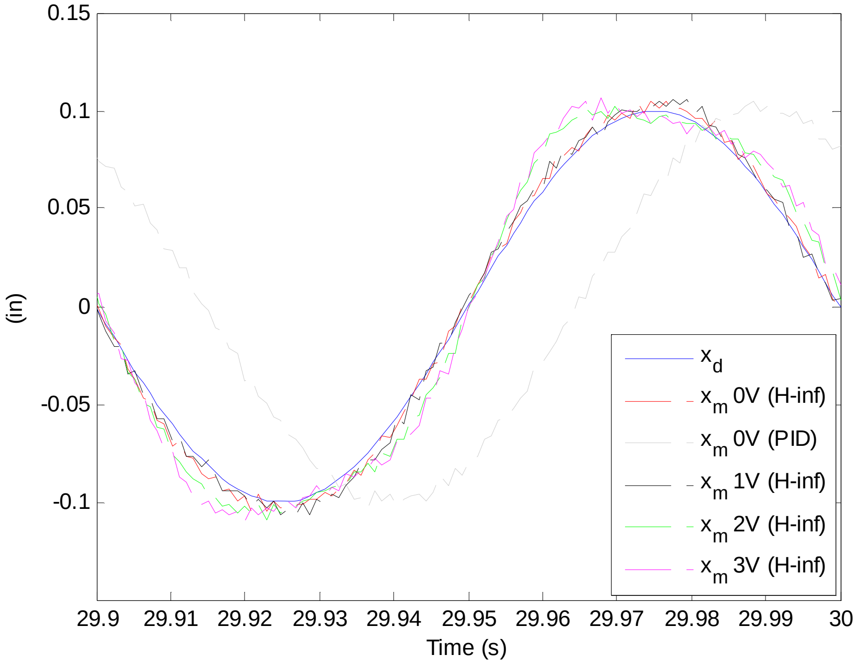

Figure 9.5 Actuator Tracking Experiment with MR Damper Specimen

Table 9.2 Actuator Tracking Error with the MR Damper Specimen

Voltage (V)	0	1	2	3
$E_{\_Tracking}$ (PID)	51.79	53.69	61.81	64.63
$E_{\_Tracking}$ (H_∞)	4.64	4.89	7.54	9.74

A chirp signal that spans 0.1-10 Hz at an amplitude of 0.1" is experimentally tested to evaluate the actuator tracking performance, when the MR damper is subjected to various input voltages. Time domain results at around 10 Hz are shown in Figure 9.5. It can be observed that the H_∞ controller performs reasonably well despite the significant plant dynamics change caused by the varying voltage. RMS tracking errors for the whole time history are summarized in Table 9.2. The H_∞ controller achieves dramatically improved tracking performance at all voltages, as compared with the results with PID control.

9.2 Clipped Optimal Structural Control Strategy

The H_2/LQG strategy is a disturbance rejection control design that has been successfully applied in the structural control community for vibration mitigation applications [(Dyke, 1996), (Jansen & Dyke, 2000), (Yi, Dyke, Caicedo, & Carlson, 2001), (Yoshida, Dyke, Giacosa, & Truman, 2003), (Ohtori, Christenson, Spencer, & Dyke, 2004)]. The dynamic equation of motion for a structure system subjected to ground motion can be expressed as

$$M_S\ddot{x} + C_S\dot{x} + K_S x = -M_S\Gamma\ddot{x}_g + \Lambda f \tag{9.6}$$

where M_s, C_s, and K_s are the mass, damping and linear stiffness of the structure respectively. Γ is a vector considering structure mass influence and Λ is the matrix considering control force interactions and is determined by the control device placement in the structure. State space expression of the system is then constructed in accordance with a standard LQG design formulation, as

$$\begin{aligned}\dot{z} &= Az + Bf + G\ddot{x}_g \\ y &= Cz + Df + H\ddot{x}_g + v\end{aligned} \tag{9.7}$$

where state variable vector z includes displacement and velocity on each discrete mass location. The output variable vector y can be any linear combination of states (e.g. accelerations for estimation of full states) and v is the measurement noise vector. The matrix coefficients are

$$\begin{aligned}A &= \begin{bmatrix} 0 & I \\ -M_s^{-1}K_s & -M_s^{-1}C_s \end{bmatrix}, B = \begin{bmatrix} 0 \\ M_s^{-1}\Lambda \end{bmatrix}, \mathrm{G} = \begin{bmatrix} 0 \\ -\Gamma \end{bmatrix} \\ C &= \begin{bmatrix} -M_s^{-1}K_s & -M_s^{-1}C_s \end{bmatrix}, D = \begin{bmatrix} M_s^{-1}\Lambda \end{bmatrix}, \mathrm{H} = \begin{bmatrix} -\Gamma \end{bmatrix}\end{aligned} \tag{9.8}$$

The control law f=-Kz is achieved by minimizing the quadratic cost functional

$$J = \int_0^\infty (y^T Qy + f^T Rf)dt \tag{9.9}$$

where Q and R are weighting matrices to define the tradeoff between regulated responses and control efforts. The optimal control gain $K=R^{-1}B^TP$ is obtained by solving the associated algebraic Riccati equation

$$A^T P + PA - PBR^{-1}B^T P + C^T QC = 0 \tag{9.10}$$

In practice it is not always feasible to measure all state variables directly, so Kalman state estimator $\hat{z}$ is then constructed to minimize the steady state error covariance

$$\lim_{t\to\infty} E(\{z-\hat{z}\}\{z-\hat{z}\}^T) \tag{9.11}$$

The nominal control force f_d determination typically needs measurements of absolute accelerations y_m and control forces f_m. This is represented by

$$\begin{aligned} \dot{\hat{z}} &= (A - LC)\hat{z} + Ly_m + (B - LD)f_m \\ f_d &= -K\hat{z} \end{aligned} \tag{9.12}$$

Assume the disturbance and measurement noise are independent zero mean white noise Gaussian processes with covariance matrices U and W, respectively. The optimal observer gain L is determined through

$$L = SC^T W^{-1} \tag{9.13}$$

where S is obtained by solving algebraic Riccati equation

$$SA^T + AS - SC^T W^{-1} CS + GUG^T = 0 \tag{9.14}$$

The nominal control force needs to be applied by physical MR damper devices which take the input voltage level as a control variable. (Dyke, 1996) proposed a clipped-optimal strategy as the secondary controller for acceleration feedback control of an MR damper. The voltage applied to each MR damper v_i is determined by the comparison of nominal desired control force f_{di} and measured force f_{mi}.

$$v_i = V_{\max} H\{(f_{di} - f_{mi}) f_{mi}\} \tag{9.15}$$

where V_{max} is the voltage to the current driver associated with saturation of the magnetic field in the MR damper, and $H\{\cdot\}$ is the Heaviside step function.

9.3 Three Phase RTHS Validation Experiments

Three phases of validation experiments are conducted in this section to examine the effectiveness of the MR damper to mitigate structural vibration. The MRF specimen with numerical mass configurations assumed in Table 8.3 are used here for validation experiments, plus the MR damper device described in section 9.1 that is placed between the reaction and the 1st floor of the steel frame. A schematic description of the test setup is shown in Figure 9.6.

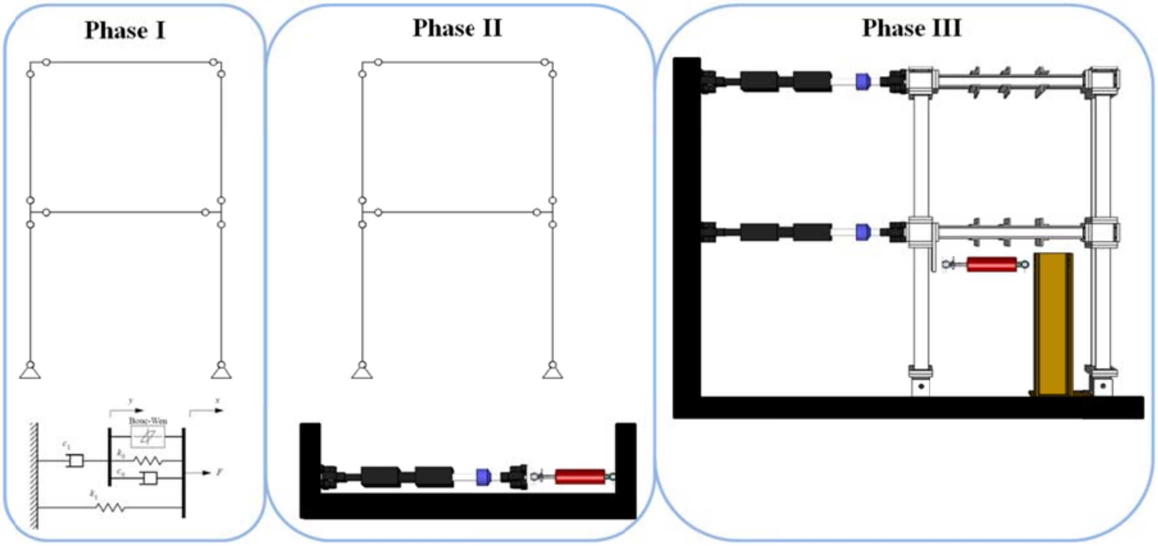

Figure 9.6 Three Phase Validation Experimental Setup

Phase I (pure numerical simulation) is chosen as the reference that comprises of a full structure model plus a simulated Bouc-Wen damper model. Phase II models the full structure as the numerical component, but only the damper as the physical substructure. Phase III integrates the damper device into the MRF specimen that are both tested physically. Additional seismic mass are assumed computationally for all three phases, and 1% of MRF stiffness is assumed numerically in phase III, using similar approach as in Chapter 8. Clipped optimal LQG controller is designed to determine the voltage that is applying on the MR damper. Calculated accelerations in the numerical substructure on both floors are used as the LQG inputs, along with the measured damper force.

Comparisons of the displacements for all three phases are shown in Figure 9.7 to Figure 9.10. Overall excellent agreement is observed for all four configurations.

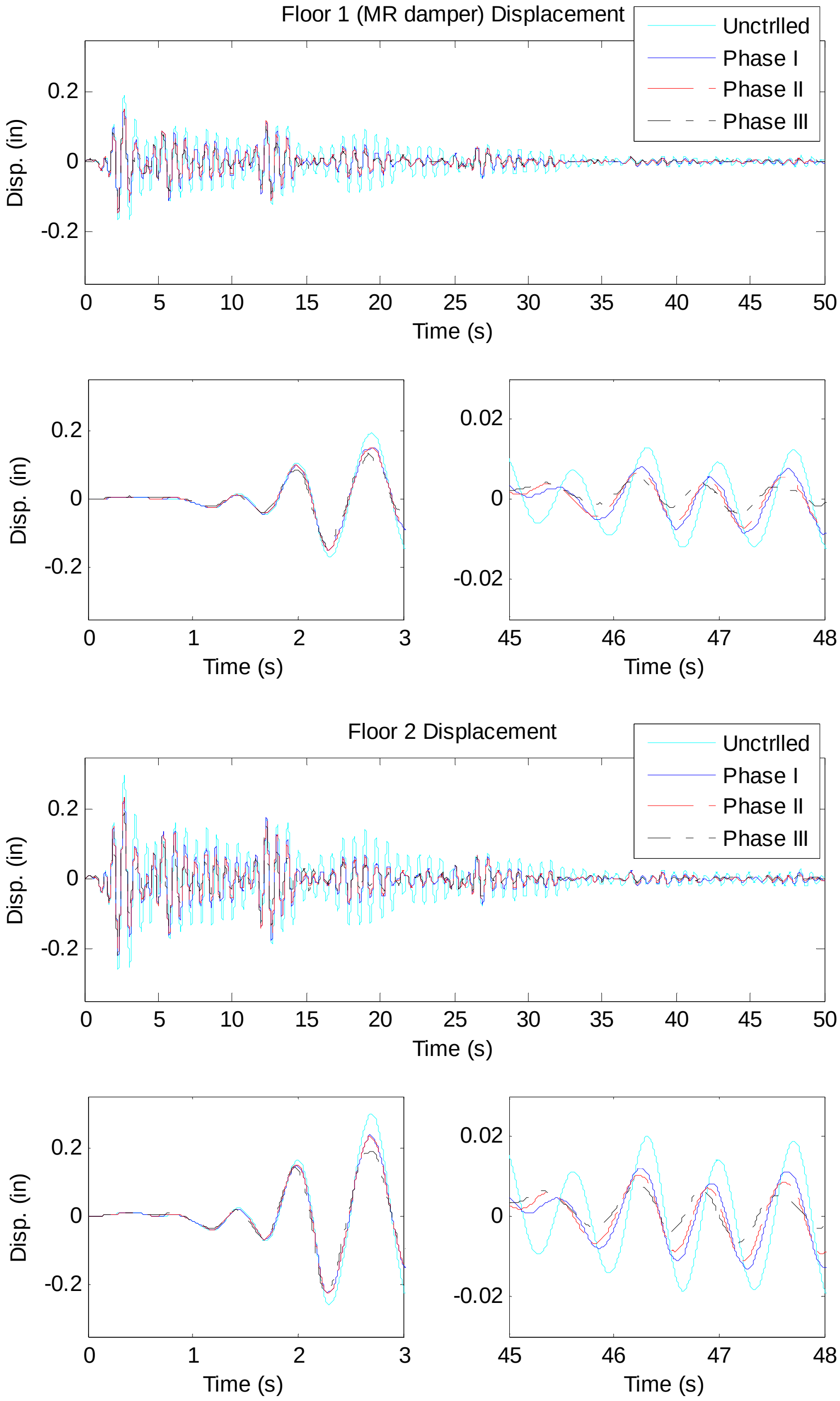

Figure 9.7 RTHS Experiment with MR Damper Controlled MRF (Config. 1)

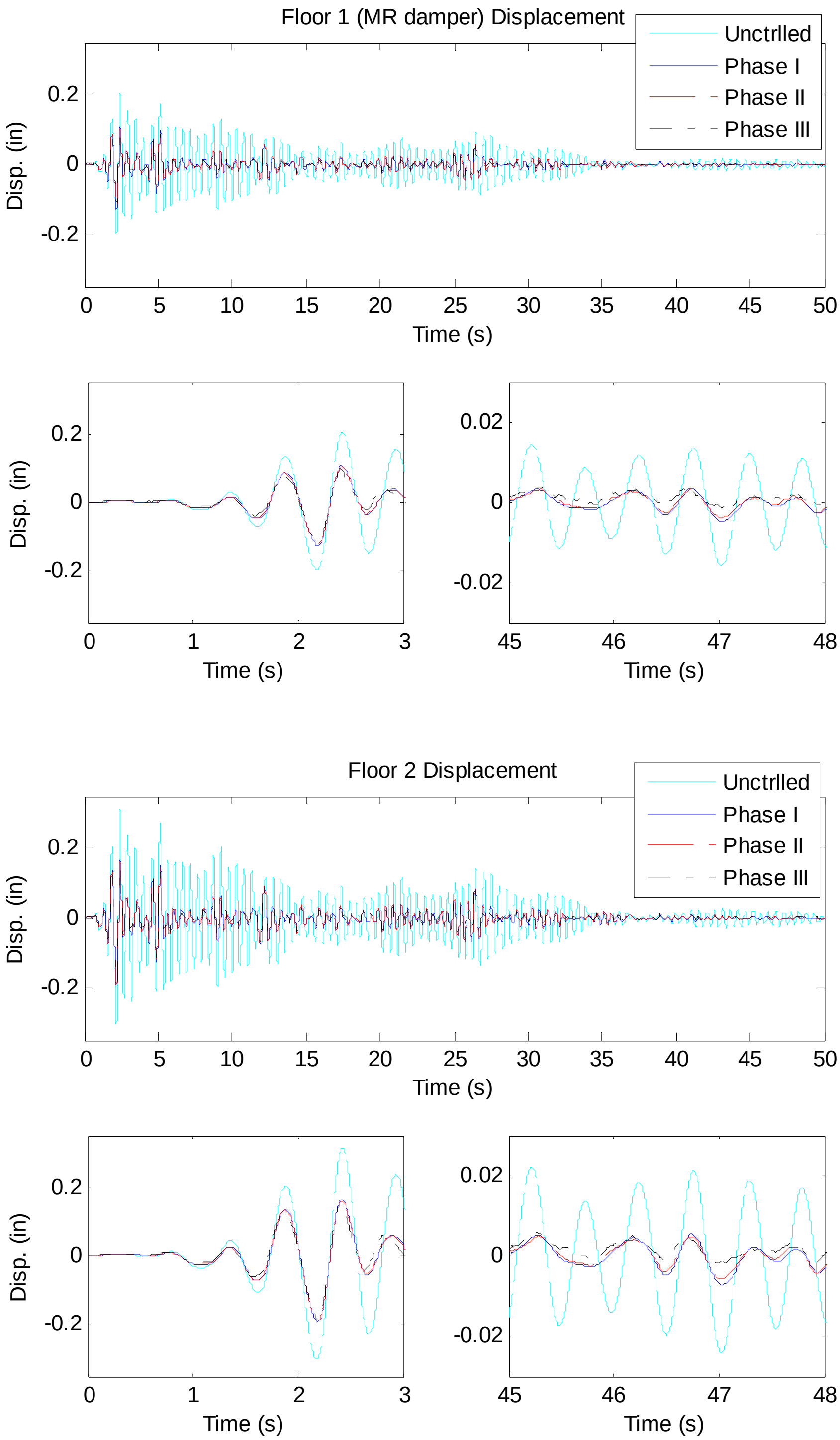

Figure 9.8 RTHS Experiment with MR Damper Controlled MRF (Config. 2)

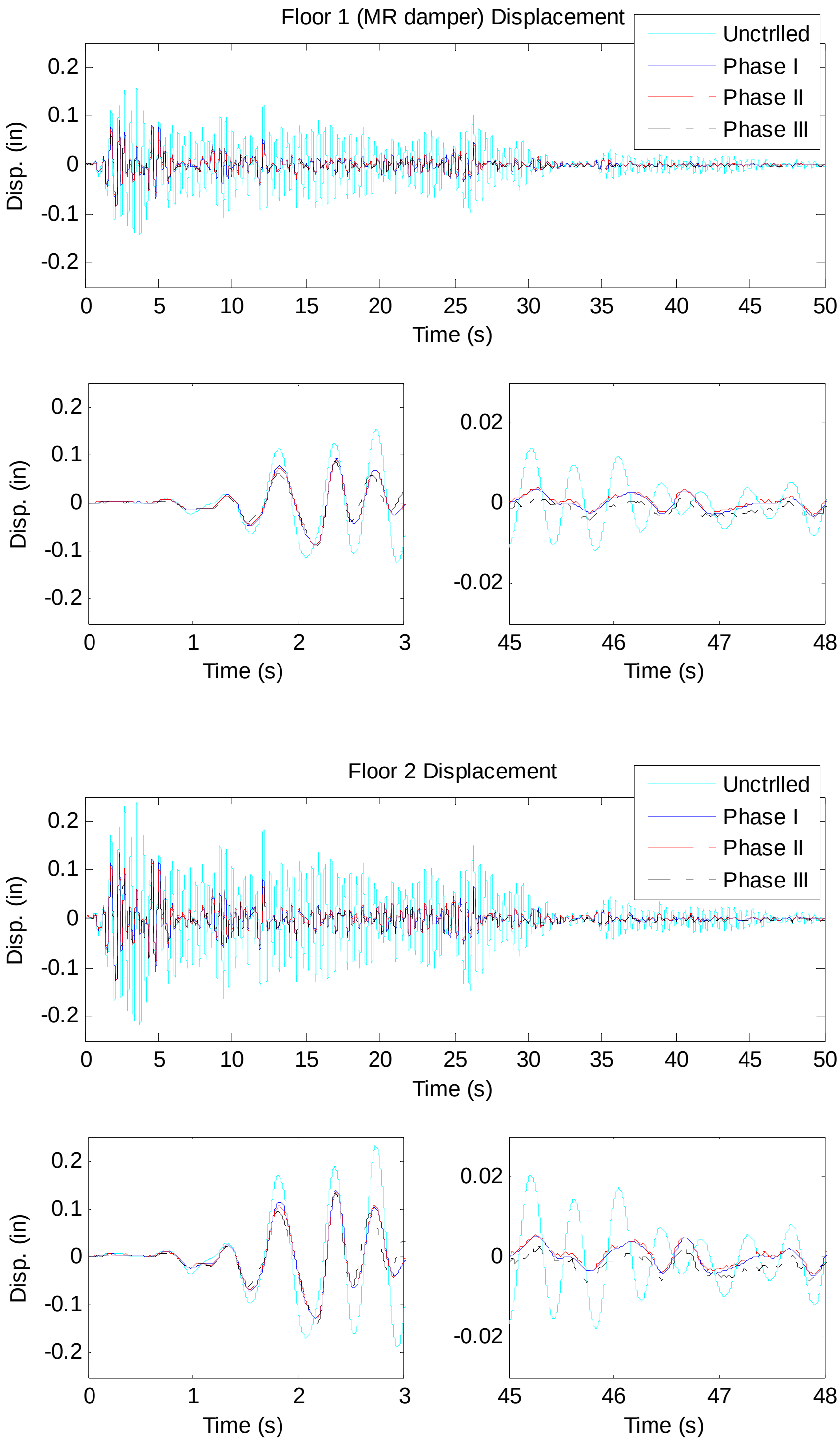

Figure 9.9 RTHS Experiment with MR Damper Controlled MRF (Config. 3)

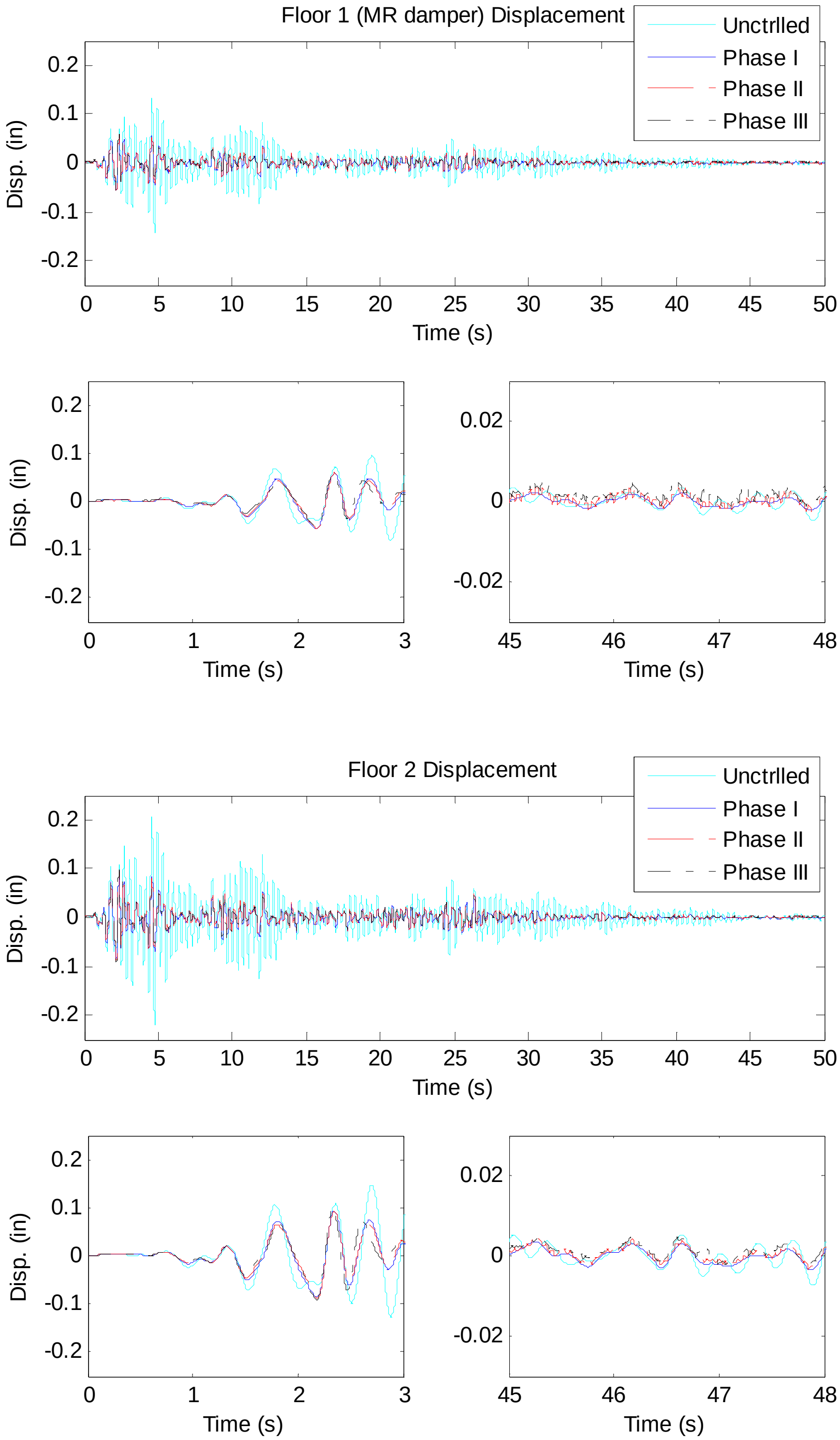

Figure 9.10 RTHS Experiment with MR Damper Controlled MRF (Config. 4)

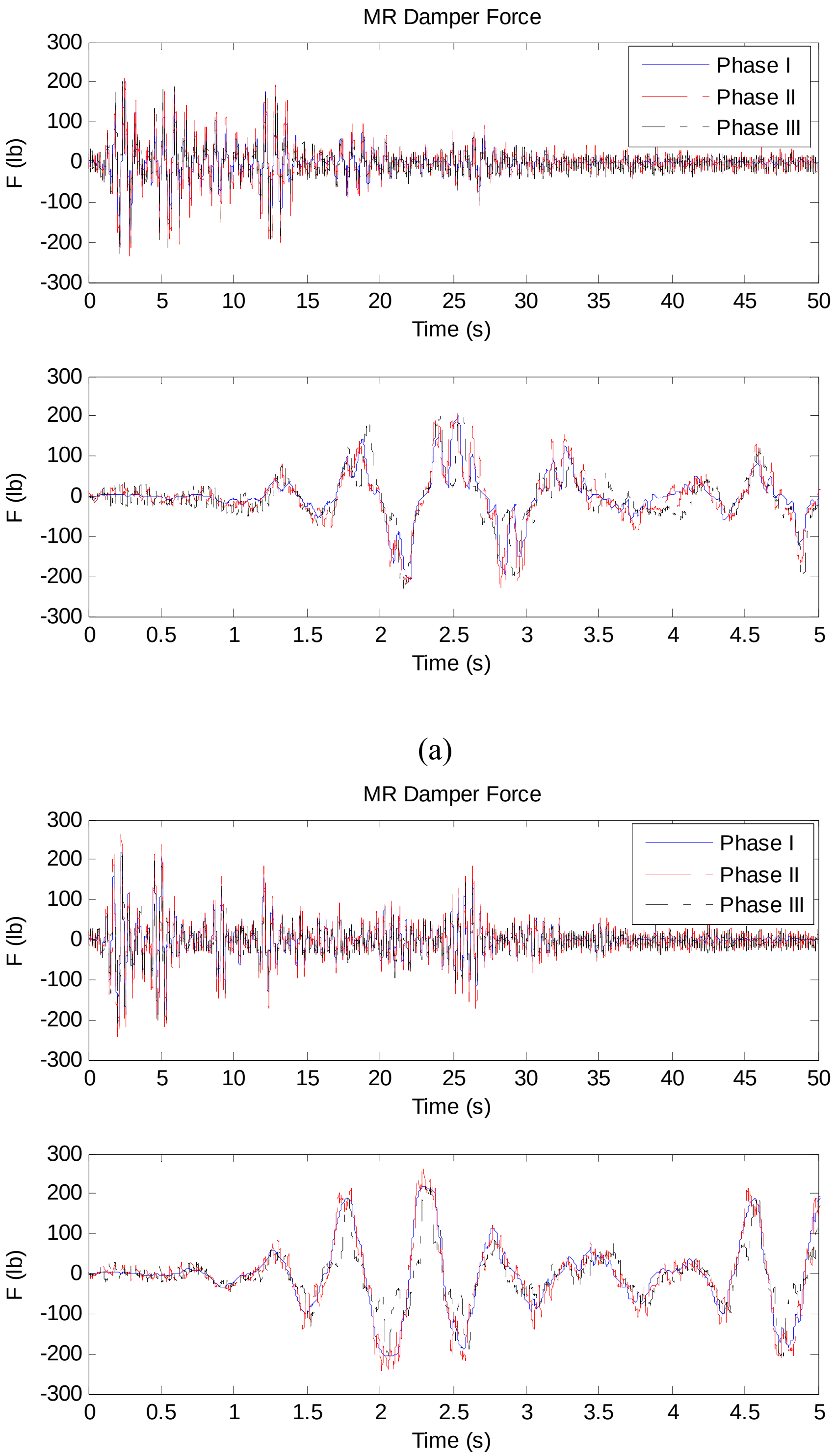

(a)

(b)

Figure 9.11 RTHS MR Damper Force Comparison
(a): Config. 1; (b): Config. 2

Table 9.3 Experimental Error with MR Damper Controlled MRF (%)

	Config. 1	Config. 2	Config. 3	Config. 4
Phase II E_{RTHS} (Floor 1)	11.33	9.35	11.85	15.93
Phase II E_{RTHS} (Floor 2)	10.49	9.09	11.76	14.68
Phase II $E_{Tracking}$ (Damper)	6.32	9.42	11.93	19.93
Phase III E_{RTHS} (Floor 1)	43.28	32.59	35.95	38.57
Phase III E_{RTHS} (Floor 2)	42.05	31.63	36.51	39.01
Phase III $E_{Tracking}$ (Floor 1)	5.90	7.83	8.99	21.02
Phase III $E_{Tracking}$ (Floor 2)	5.04	6.91	7.46	14.20

A summary of the test matrix results are shown in Table 9.3 where both normalized RTHS error and tracking error are listed. Phase I displacement responses are herein used as the reference to evaluate the RTHS errors. Consistent good performance is observed for all tests. The relatively larger phase III RTHS error can be explained partially by the MR damper force error, as shown in Figure 9.11. More challenges exist in phase III as the experimental setup becomes more complex. The setup may yield a small relative deformation between the damper and the floor of the MRF specimen, instead of the perfect rigid connection assumption. This experimental setup error is less significant for phase II, because the Bouc-Wen model in phase I is identified using the same setup (Figure 9.2). Therefore, the setup imperfection is likely to be absorbed by the identification procedure. Another consideration is that the RTHS error in phase III is more sensitive to the actuator tracking error, because the physical substructure comprises a much larger portion of the overall RTHS system. The force interactions between the physical damper and the MRF specimen also need to be investigated in the future, to interpret the RTHS results and to improve the test accuracy.

Another objective in this study is to assess the mitigation of the structural vibration by comparing the responses with the uncontrolled cases, when the damper is not installed in the structure. Reference structural displacements in Chapter 8 are included in Figure 9.7 to Figure 9.10 as the uncontrolled responses. It is obvious that vibration is significantly reduced for all configurations when the damper is present and the semi-active control strategy is activated. Table 9.4 lists floor peak and RMS displacements for all tests. Each numeric value in the table is calculated as the percentage of the controlled response over the corresponding uncontrolled response. For each specific configuration, it is observed that the evaluation index compare well for all three phases. The MR damper is very effective to reduce the response when the seismic mass is moderate, e.g. more than 60% RMS and 40% peak response reduction in configuration 2-4. The damper maximum force capacity is relatively small compared to the demand control force in configuration 1 when the seismic mass is large. Therefore, the vibration mitigation is not as effective as other configurations. Another interesting observation is that the phase III responses are consistently smaller compared to Phase I and II.

Table 9.4 Structural Vibration Mitigation (%)

		Peak Floor 1	Peak Floor 2	RMS Floor1	RMS Floor 2
Config. 1	Phase I	78.38	79.03	69.90	69.87
	Phase II	77.90	78.28	65.74	67.19
	Phase III	72.56	71.64	50.76	53.07
Config. 2	Phase I	60.97	60.84	38.33	38.42
	Phase II	61.39	59.78	37.30	37.92
	Phase III	51.47	57.45	30.76	32.42
Config. 3	Phase I	56.88	57.64	38.30	38.39
	Phase II	58.48	57.00	36.78	37.10
	Phase III	54.80	57.24	31.24	32.57
Config. 4	Phase I	41.95	42.48	39.16	39.37
	Phase II	43.24	42.64	38.30	38.19
	Phase III	40.93	44.79	32.84	35.09

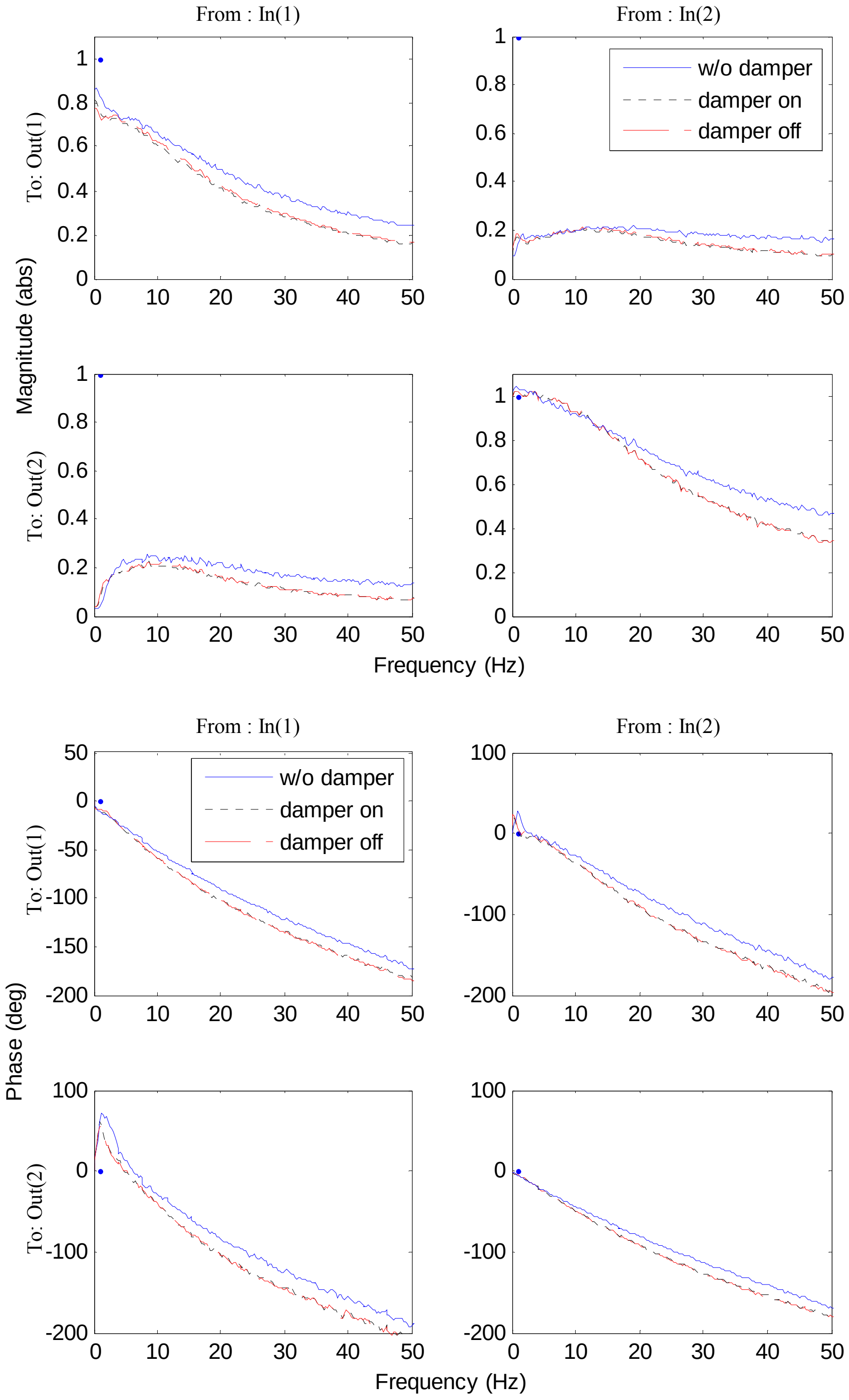

Figure 9.12 Displacement Transfer Functions with MR Damper Controlled MRF

The transfer function matrix for phase III setup, between the command and measured displacements, are compared in Figure 9.12. Note first the experimental transfer matrix without the damper is different from the one in Figure 8.2, although the mechanical system setup is identical. The reason is that the servo- hydraulic controller board used in Chapter 8 is replaced with another one for the experiments conducted in this chapter. Although the PID gains are kept the same after the hardware is replaced, the changed electrical components do have a major influence on the plant dynamics. In Figure 9.12, plant dynamics change significantly before and after the damper device is installed. However, the plant is rather insensitive to the voltage that is applied to the damper.

Another test matrix is conducted to demonstrate the robustness feature of the H_∞ control strategy. An H_∞ controller is designed using the plant transfer matrix without the damper. Phase III tests are then repeated to mimic the situation when the H_∞ controller is not aware of the sudden plant change. RTHS errors are summarized in Table 9.5. Very similar experimental results are achieved for configuration 1-3, when compare with the corresponding results in Table 9.3. The strong robustness property of the proposed H_∞ design is therefore demonstrated again. Instability occurs for configuration 4, because the plant variation at higher frequency range exceeds the tolerance level of the H_∞ controller. Many more challenges arise when the reference structural modes increase, which demands extended tracking performance bandwidth. The uncertainty modeling and analysis tools introduced in Chapter 4 can be considered to characterize the physical plant uncertainty bounds; to facilitate the controller design for maximum performance limit.

Table 9.5 Robustness Evaluation with MR Damper Controlled MRF (%)

	Config. 1	Config. 2	Config. 3	Config. 4
Phase III E_{RTHS} (Floor 1)	43.30	33.44	38.41	N.A.
Phase III E_{RTHS} (Floor 2)	41.89	32.40	38.99	N.A.

The last validation procedure involves nonlinear beam elements in the RT-Frame2D model. Only phase I and II of RTHS are conducted in this test matrix. The beam moment-curvature relationships are characterized by three different models that are linear, bilinear and tri-linear kinematic hardening rules, respectively. The post yielding ratio is assumed to be 0.02 for the bilinear model and 0.5/0.02 for the tri-linear model. Columns are modeled to be linear elastic and the beam column joints are characterized by the linear panel zone model. The mass and damping assumption follows configuration 3 described in Chapter 8. The El-Centro earthquake is scaled to be 0.7 times the original intensity. Comparison of RTHS results are shown in Figure 9.13 to Figure 9.15 where excellent match are observed in all tests. The MR damper is demonstrated to be effective in energy dissipation and protecting the structural members from damage, e.g. significant less beam end hysteresis and permanent floor drift are developed when the damper is present in the structural system. Table 9.6 evaluates both normalized RTHS and actuator tracking errors for all three tests. The errors herein, including the ones with nonlinear models, are much smaller than the counterparts in Table 9.3. The reason is that the earthquake intensity used in this test matrix is much larger, which results in larger structural responses. A large displacement magnitude enables better H_∞ controller tracking performance, because the noise to signal ratio is less. Therefore, this result demonstrates that the noise effect within the closed-loop RTHS system is very important.

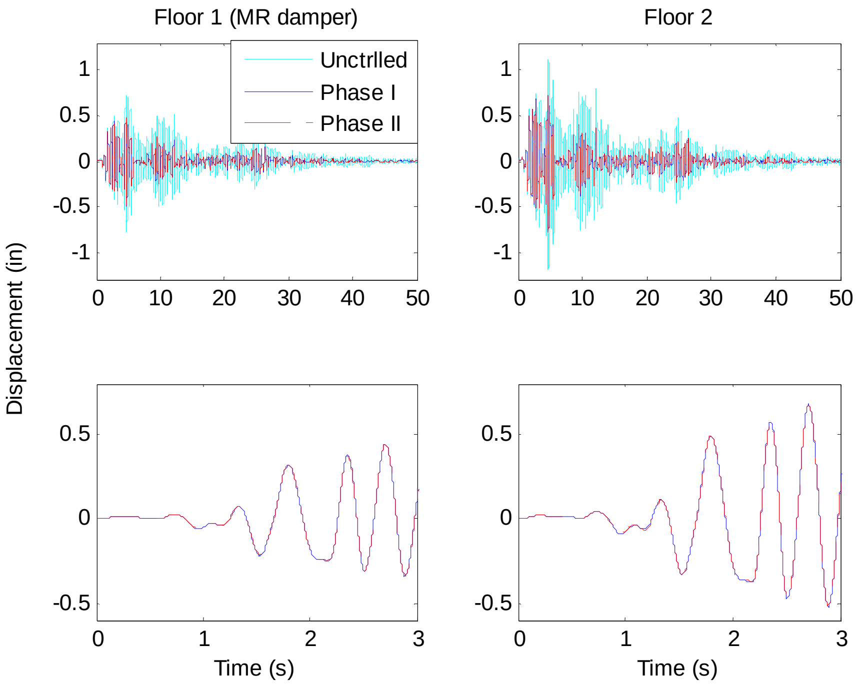

(a)

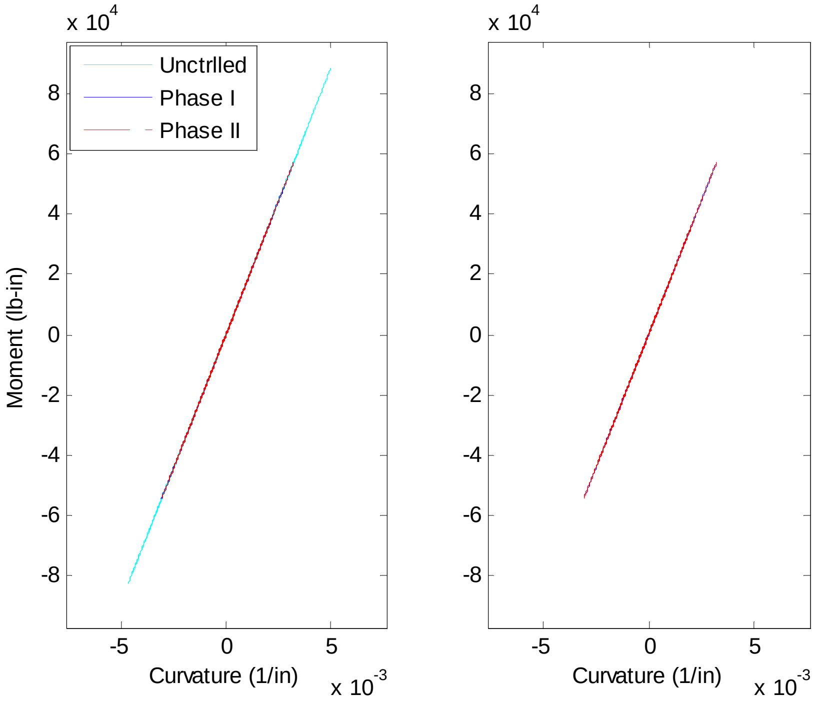

(b)

Figure 9.13 RTHS Results with Linear Beam Assumption
(a): Floor Displacements; (b): Beam End Hysteresis

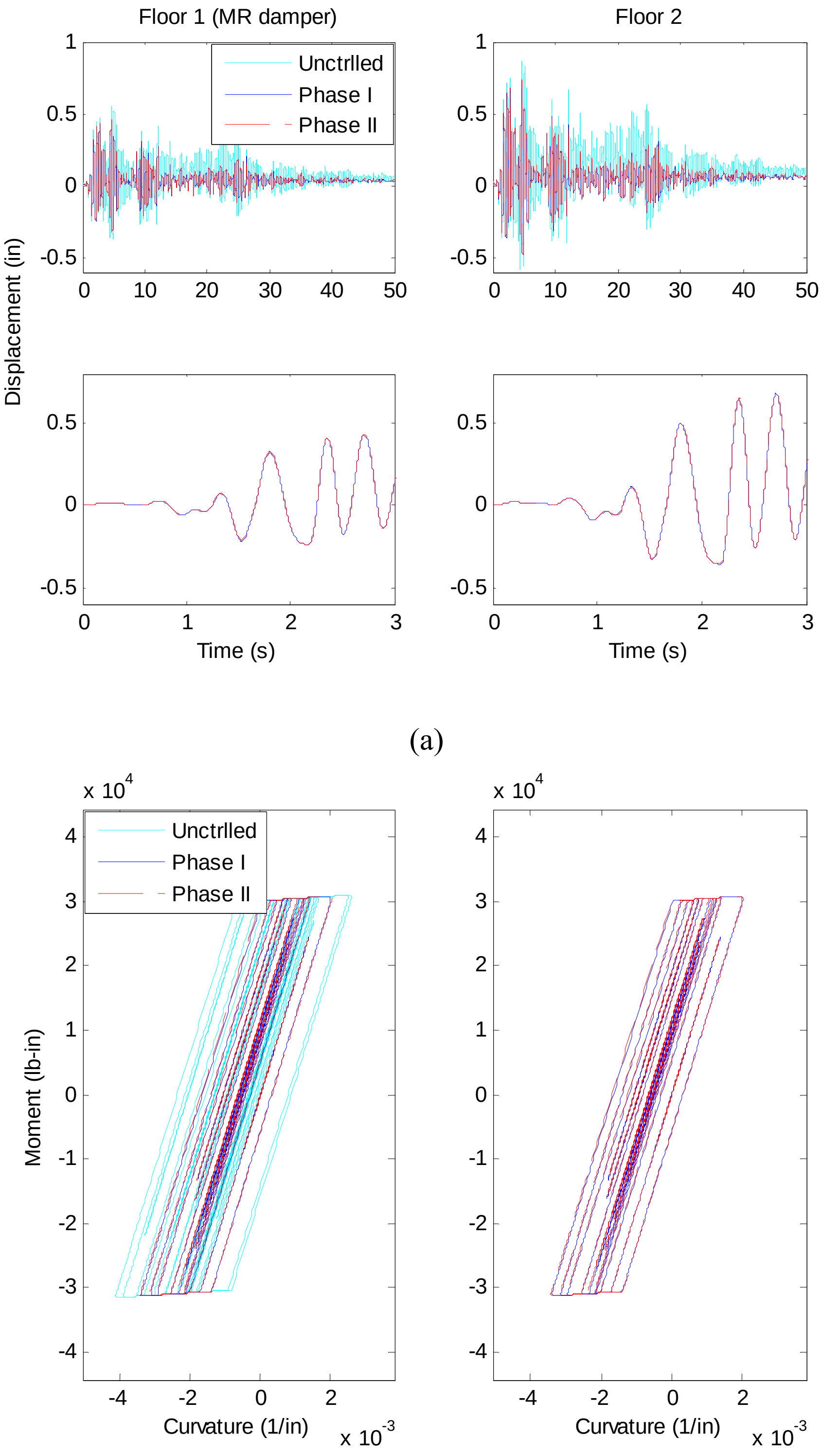

(a)

(b)

Figure 9.14 RTHS Results with Bilinear Beam Assumption
(a): Floor Displacements; (b): Beam End Hysteresis

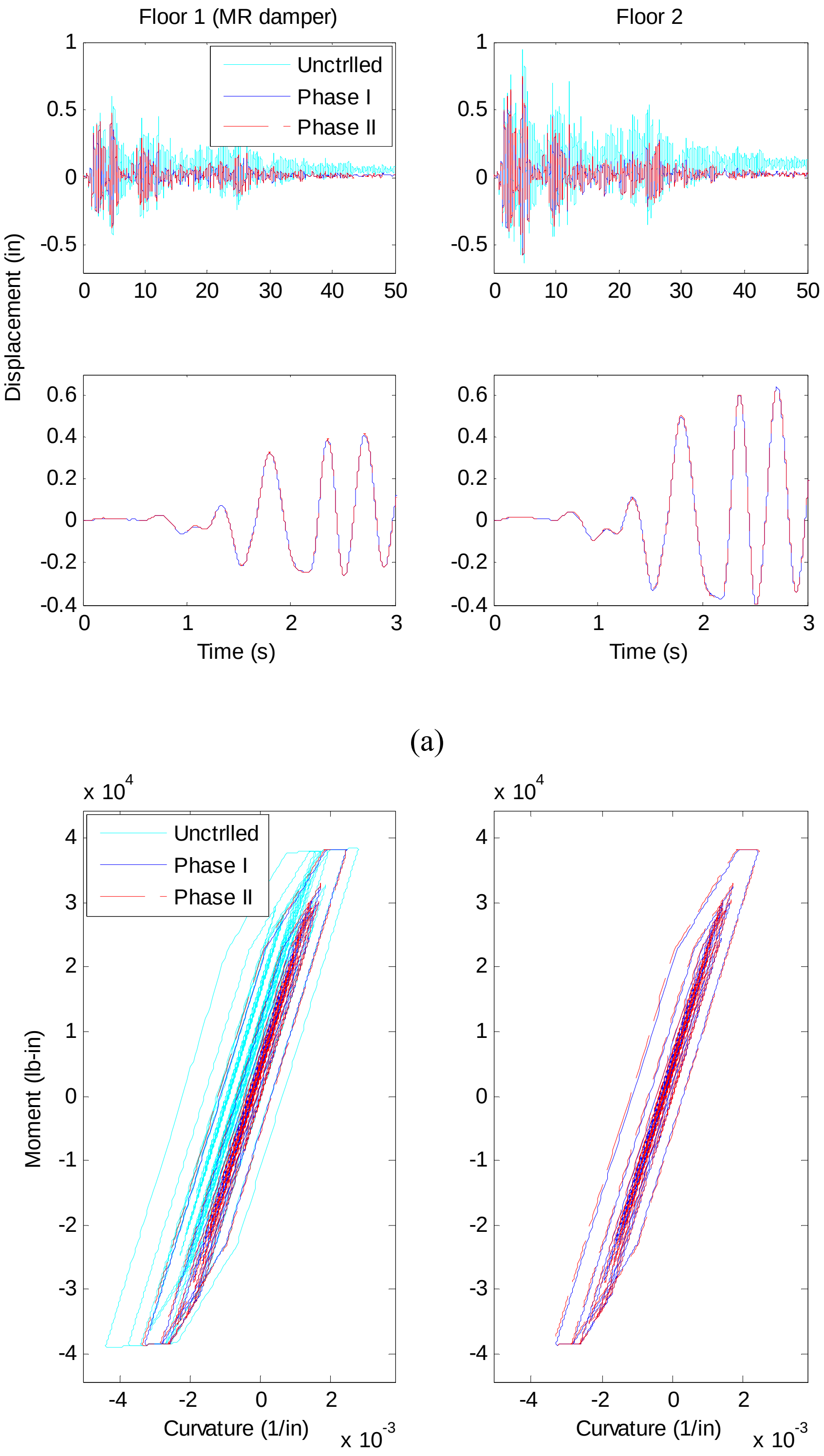

(a)

(b)

Figure 9.15 RTHS Results with Tri-linear Beam Assumption
(a): Floor Displacements; (b): Beam End Hysteresis

Table 9.6 Experimental Error with Controlled Nonlinear MRF (%)

	Linear	Bi-linear	Tri-linear
Phase II $E_{\_RTHS}$ (Floor 1)	3.14	3.32	4.21
Phase II $E_{\_RTHS}$ (Floor 2)	3.12	3.35	4.27
Phase II $E_{\_Tracking}$ (Damper)	3.26	3.4	3.3

9.4 Summary

The developed RTHS framework is used in this chapter to evaluate the MR damper and its effectiveness in terms of structural vibration mitigation. Optimal voltage to the MR damper is determined using the LQG control algorithm. A three phase validation procedure is performed experimentally when the MRF response is restricted to be linear. All results compare well, which demonstrates the capacity of the developed framework in testing highly rate dependent and nonlinear physical components. Phase I and II tests are then conducted successfully when nonlinear MRF beam is assumed. Robustness of the proposed H_∞ controller is evaluated too in this chapter, using both phase II and III experimental setup. The controller is demonstrated capable of tolerating significant plant variation, as well as the initial plant modeling error.

CHAPTER 10
CONCLUSIONS AND FUTURE WORK

A novel robust framework is developed in this dissertation for real-time hybrid simulation. The study is primarily motivated by the cost effectiveness nature of the RTHS methodology. The developed framework is intended for general structural analysis purposes, and moreover is especially suitable for dynamic testing of advanced structural vibration mitigation control strategies. Extensive validation experiments are conducted to demonstrate the superior performance of the framework. Some of the important research findings and potential future work are summarized in this chapter.

10.1 Summary of Conclusions

The very basic concept of hybrid simulation is to combine the numerical analysis with physical testing. This concept therefore defines two limits, i.e. a pure digital domain when the entire structure is numerically analyzed, vs. a pure analog domain when the whole structure is physically tested. Unique challenges arise when a test plan falls between the two limits, especially the ability to achieve a synchronization of motion boundary conditions between the two domains. The sensitivity of the RTHS error to this de-synchronization error is studied in Chapter 3. A worst case scenario is identified when the structural stiffness is 100% assumed physically, which is demonstrated to be a mathematically singular problem.

Most of this dissertation focuses on this (semi) worst case RTHS setup by physically testing the majority of the structural stiffness, but assume the majority of the seismic mass numerically. This setup in reality is also very representative to take advantage of the hybrid testing technique. Because the structural stiffness is normally unknown that needs to be experimentally investigated, but the mass can be conveniently assumed numerically to avoid the associated prohibitive cost. Actuator motion control therefore becomes a very important component of a RTHS framework. Given a specific experimental plan, this study also establishes a quick way to estimate the test stability limit.

A highly effective control design normally requires the extensive knowledge of the plant itself. Normally the more information is available from the plant, the better control action can be taken. However, this requirement is somewhat contradictory to the objective of hybrid testing when limited information is available from the unknown experimental substructure (part of the plant). Therefore, the motivation to develop adaptive and/or robust control strategies in this dissertation, which can deal with plant uncertainties, is particularly attractive for RTHS applications.

A RTHS system is basically a control system in which different components have their own dynamics that also interact with each other through feedback/feedforward links. Established control system analysis tools can thus be used to understand the inputs/outputs, the systems or the subsystems. A frequency domain modeling approach is presented in this study that can add both parametric and non-parametric uncertainties into a system, so that important system properties (e.g. the stability limit) can be analyzed.

Parameter study indicates that the servo-hydraulic inner-loop control system is very sensitive to the proportional gain and the tested mass, but less sensitive to the specimen stiffness.

The proposed robust H_∞ loop shaping control strategy is extensively validated. Both superior tracking performance and strong robustness properties are demonstrated through several experimental setup. Moreover, the original H_∞ control theory was formulated for multivariable control applications, which can minimize the dynamic coupling between multiple inputs and outputs. Therefore, it is an ideal candidate for a generalized RTHS framework that can be expanded to more complicated setup in the future.

10.2 Recommended Future Work

The RTHS error caused by the actuator displacement tracking error is studied extensively in this dissertation. Advanced modern control techniques are proposed to reduce these de-synchronization errors. The motion controller designs in this dissertation are all based on displacement feedback control. However, the quality of force synchronization is still to be determined that is another major consideration to achieve accurate RTHS results.

A series of tests is conducted to evaluate the actuator force tracking performance, using the two floors MRF specimen setup described in Chapter 8. Two very slow (low frequency) chirp displacement input signals are used to drive the two actuators, respectively. The amplitude of the chirp signals are described in Table 10.1. Note that a different amplitude combination is used for each test, but the two actuators are always commanded to move at the same frequency.

Table 10.1 Displacement Inputs to Examine Actuators Force Coupling

	Input 1	Input 2	Input 3	Input 4
Amplitude floor 1 (in)	0.184	0.181	0.177	0.172
Amplitude floor 2 (in)	0.269	0.274	0.280	0.288

The desired (x_d) and the measured (x_m) displacements are presented in the upper plots of Figure 10.1 to Figure 10.4. The desired (F_d) and the measured (F_m) forces are presented in the lower plot of each corresponding figure. Here the desired forces are calculated by multiplying the identified MRF stiffness in equation (8.9) with x_d. It is obvious that the displacement controls for all tests are very effective, which is straightforward to achieve, especially for such slow motion trajectories. However, the observation of forces is quite interesting. The measured forces are more or less close to the desired values in Figure 10.1. However, the measured forces start to lose track of the predicted forces as the command displacement to the 1st floor actuator decreases while the command to the 2nd floor actuator increases. The observed force prediction errors clearly indicate a strong force coupling between the two actuators, even though the desired displacements are already applied successfully. This nonlinear force coupling appears to be a function of the applied displacement amplitudes. In the most severely coupled test result in Figure 10.4, the 1st floor actuator measured force shows even opposite sign compared to the desired force. The force coupling is very strong in an order-of-magnitude of several hundred pounds, when the displacement varies only a few thousandths of an inch.

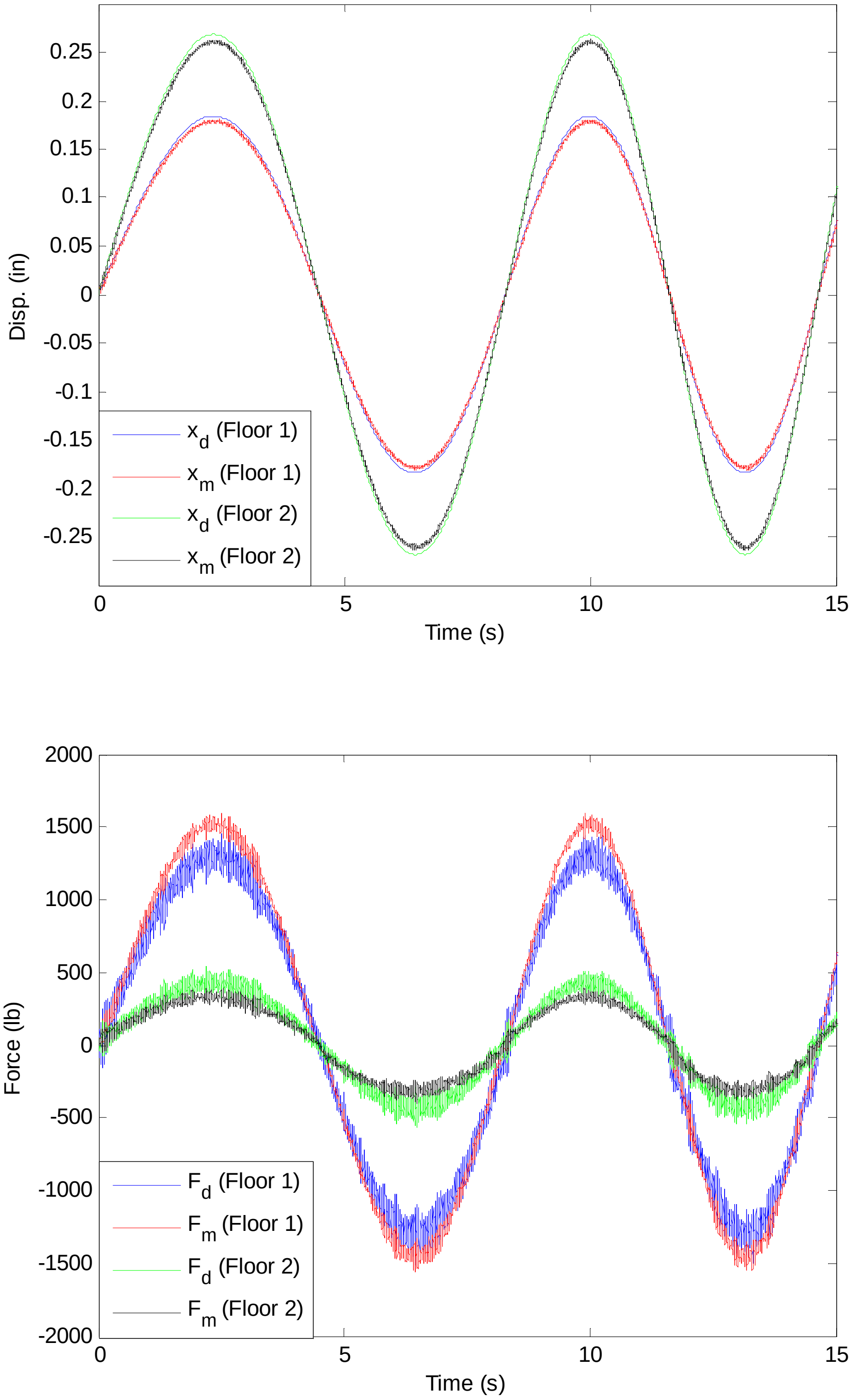

Figure 10.1 Force Coupling Between Multiple Actuators (Input 1)

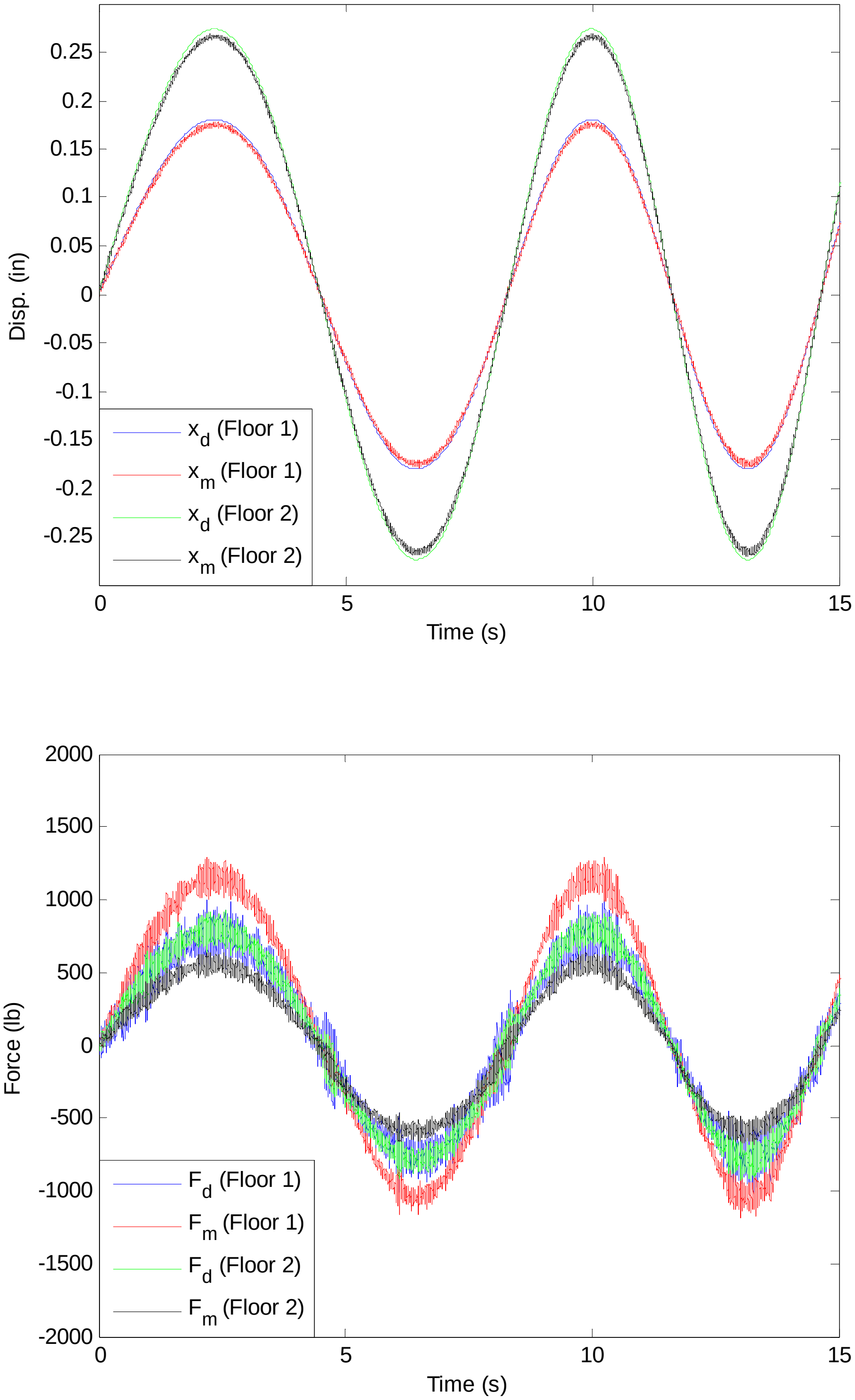

Figure 10.2 Force Coupling Between Multiple Actuators (Input 2)

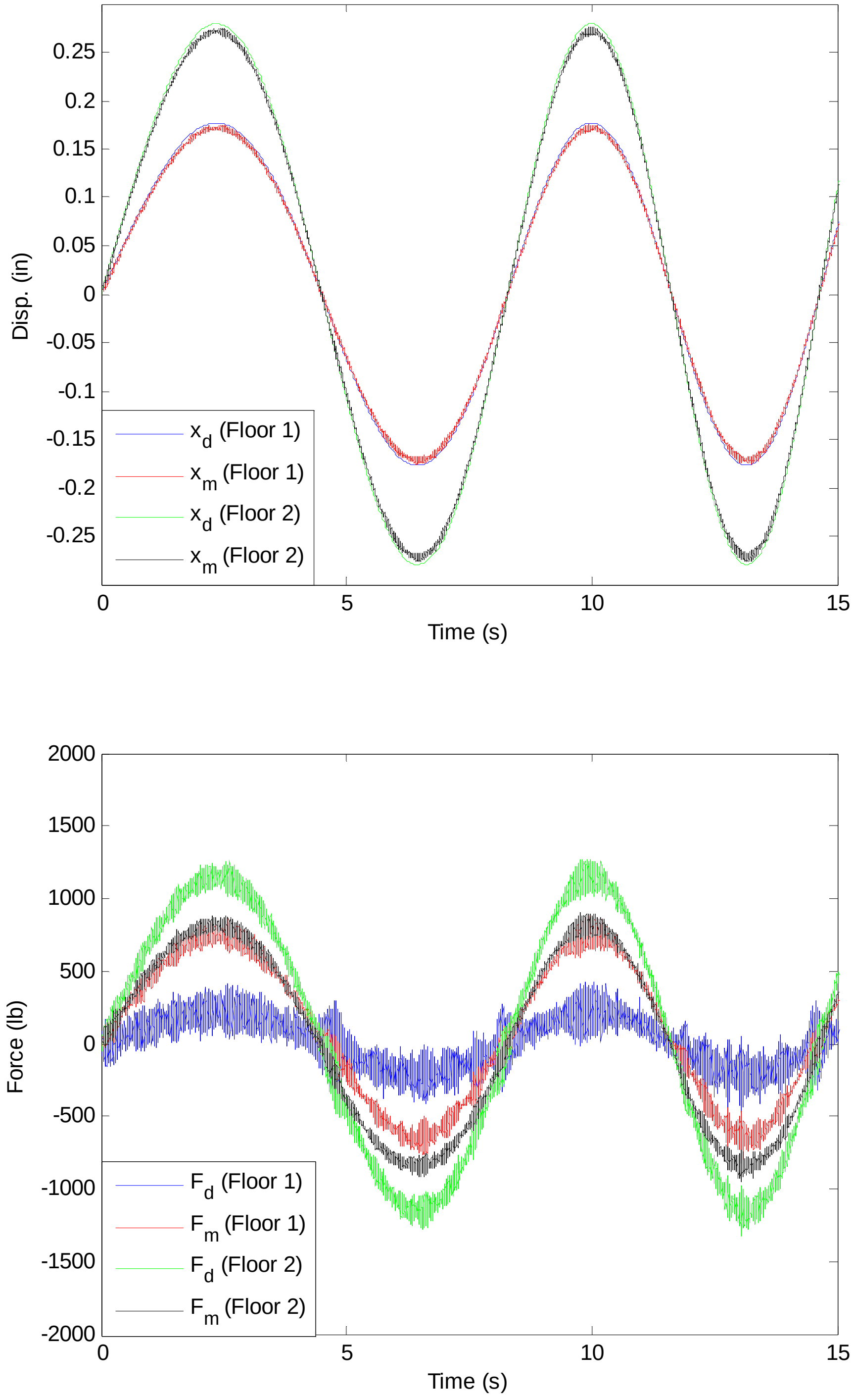

Figure 10.3 Force Coupling Between Multiple Actuators (Input 3)

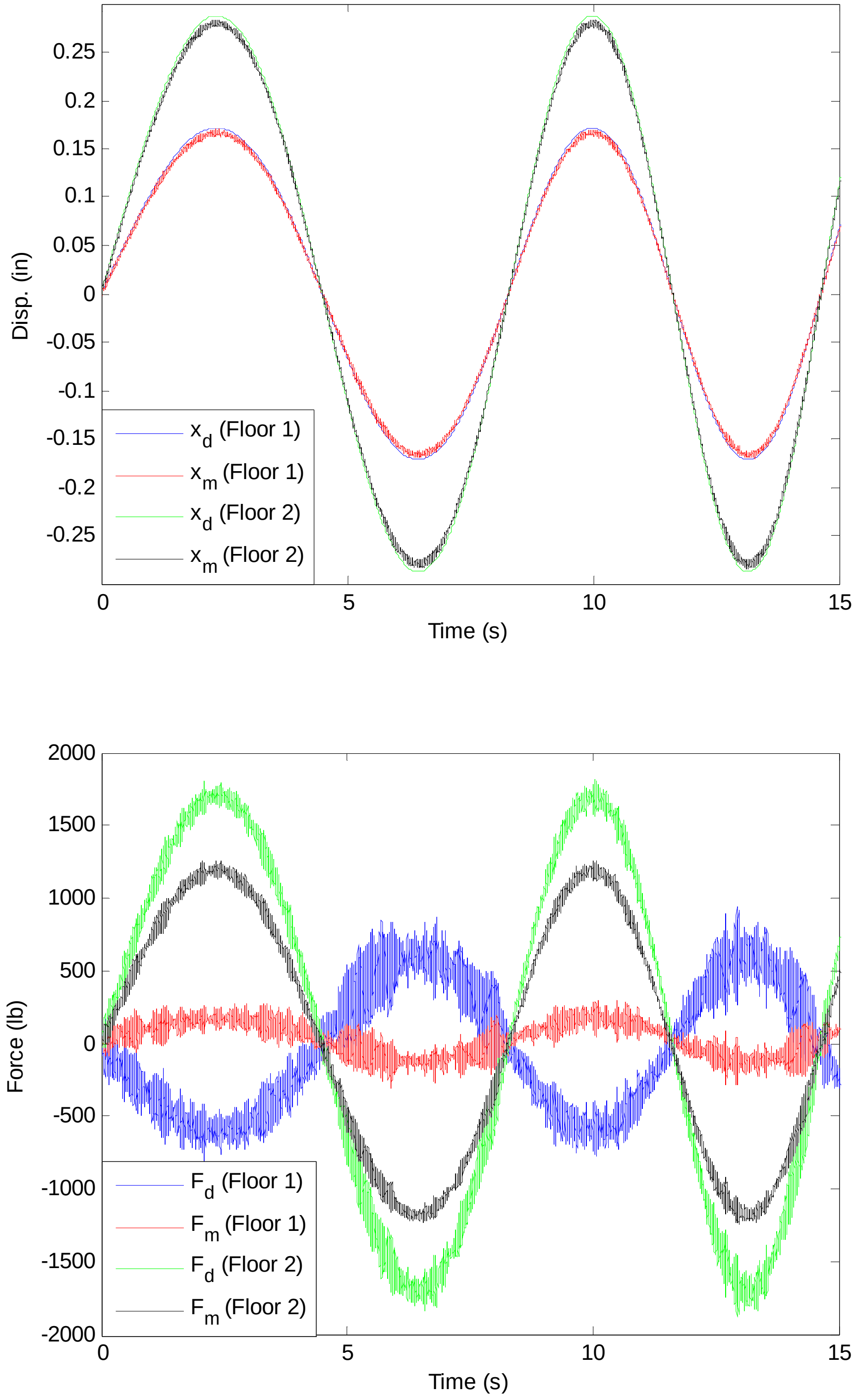

Figure 10.4 Force Coupling Between Multiple Actuators (Input 4)

It is very important for future studies to understand the mechanisms behind this force coupling phenomenon. Preferably a physics based modeling approach can be developed to capture the behavior. The coupling appears to exist even when the test is conducted in a quasi-static manner, so that a simple static model may be worth trying initially to tackle this effort. Each actuator itself can be treated as a nonlinear spring with finite stiffness, which can be characterized as a function of all inputs amplitude. A dynamical model may later be considered as the next step to model the coupling, after more refined field data are available to support the assumptions. It is a different perspective when trying to achieve the control of force tracking, which inevitably requires decoupling the forces. The challenges are that simultaneous high performance displacement tracking cannot be compromised, in the context of a complete RTHS implementation. The RTHS outer-loop controller development efforts to date are based on either displacement or force control, but not both. Future controller development may, however, need to be a combination of mixed displacement and force control.

The potential development of high performance mixed control scheme is also important in future RTHS applications when important structural components are to be tested. Therefore the motion boundary conditions are not only restricted to the linear directions, but may also need to include rotational DOFs. A three dimensional RTHS physical substructure testing may be a logical expansion of the current framework development. Similarly it is expected to pose more challenges to control the motion of multi-directional coupled actuators.

Finally, high quality hardware is critical to improve the RTHS performance. Especially it is desirable to have a control system with low measurement noise, to avoid the propagation of undesired signal frequency components.

LIST OF REFERENCES

LIST OF REFERENCES

Ahmadizadeh, A., Mosqueda, G., & Reinhorn, A. M. (2008). Compensation of Actuator Dynamics for Real-time Hybrid Simulation. *Earthquake Engineering and Structural Dynamics, 37*(1), 21-42.

Blakeborough, A., Williams, M. S., Darby, A. P., & Williams, D. M. (2001). The Development of Real-time Substructure Testing. *Philosophical Transactions of Royal Society, 359*(1786), 1869-1891.

Bonnet, P. A. (2006). *The Development of Multi-axis Real-time Substructure Testing.* Oxford, UK: University of Oxford.

Bonnet, P. A., Lim, C. N., William, M. S., Blakeborough, A., Neild, S. A., Stoten, D. P., & Taylor, C. A. (2007). Real-Time Hybrid Experiments with Newmark Integration, MCSmd Outer-Loop Control and Multi-Tasking Strategies. *Earthquake Engineering and Structural Dynamics, 36*(1), 119-141.

Carrion, J. E., & Spencer, B. F. (2007). *Model-based Strategies for Real-time Hybrid Testing.* Urbana, IL: University of Illinois at Urbana-Champaign.

Carrion, J. E., Spencer, B. F., & Phillips, B. M. (2009). Real-Time Hybrid Simulation for Structural Control Performance Assessment. *Earthquake Engineering and Engineering Vibration, 8*(4), 481-492.

Castaneda, N. (2012). *Development and Validation of a Real-time Computational Framework for the Hybrid Simulation of Dynamically-Excited Steel Frame Structures.* West Lafayette, IN: School of Civil Engineering, Purdue University.

Chen, C. (2007). *Development and Numerical Simulation of Hybrid Effective Force Testing Method.* Bethlehem, PA.: Dept. of Civil and Environmental Engineering, Lehigh Univ.

Chen, C., & Ricles, J. M. (2008). Development of Direct Integration Algorithms for Structural Dynamics using Discrete Control Theory. *Journal of Engineering Mechanics, 134*(8), 676-683.

Chen, C., & Ricles, J. M. (2010). Tracking Error-based Servohydraulic Actuator Adaptive Compensation for Real-time Hybrid Simulation. *Journal of Structural Engineering, 136*(4), 432-440.

Chen, C., Ricles, J. M., Karavasilis, T. L., Chae, Y., & Sause, R. (2012). Evaluation of a Real-Time Hybrid Simulation System for Performance Evaluation of Structures with Rate Dependent Devices Subjected to Seismic Loading. *Engineering Structures, 35*, 71-82.

Christensen, R. E., Lin, Y., Emmons, A., & Bass, B. (2008). Large-Scale Experimental Verification of Semi-Active Control Through Real-Time Hybrid Simulation. *Journal of Structural Engineering, 134*(4), 522-534.

Darby, A. P., Blakeborough, A., & Williams, M. S. (2001). Improved Control Algorithm for Real-time Substructure Testing. *Earthquake Engineering and Structural Dynamics, 30*(3), 431–448.

Darby, A. P., Williams, M. S., & Blakeborough, A. (2002). Stability and Delay Compensation for Real-Time Substructure Testing. *Journal of Engineering Mechanics, 128*(12), 1276-1284.

Doyle, J., Francis, B., & Tannenbaum, A. (1990). *Feedback Control Theory.* New York: Macmillan Publishing Co.

Dyke, S. J. (1996). *Acceleration Feedback Control Strategies for Active and Semi-active Control Systems: Modeling, Algorithm Development, and Experimental Verification.* Notre Dame, IN: University of Notre Dame.

Dyke, S. J., Spencer, B. F., Quast, P., & Sain, M. K. (1995). The Role of Control-Structure Interaction in Protective System Design. *ASCE Journal of Engineering Mechanics, 121*(2), 322-338.

Dyke, S. J., Spencer, B. F., Sain, M. K., & Carlson, J. D. (1996). Modeling and Control of Magnetorheological Dampers for Seismic Response Reduction. *Smart Materials and Structures, 5*(5), 565-575.

Franklin, G., Powell, D., & Emami-Naeini, A. (2002). *Feedback control of Dynamic Systems.* New Jersey: Prentice Hall.

Gao, X., Castaneda, N., & Dyke, S. (Accepted). Real-time Hybrid Simulation: from Dynamic System, Motion Control to Experimental Error. *Earthquake Engineering and Structural Dynamics*.

Gavin, H. P. (2001). Multi-duct ER Dampers. *Journal of Intelligent Material Systems and Structures, 12*(5), 353-366.

Giraldo, D., Yoshida, O., Dyke, S. J., & Giacosa, L. (2004). Control-oriented System Identification Using ERA. *Structural Control and Health Monitoring, 11*, 311–326.

Glover, K., & McFarlane, D. (1989). Robust Stabilization of Normalized Coprime Factor Plant Descriptions with H∞-bounded Uncertainty. *IEEE Transactions on Automatic Control, 34*(8), 821-830.

Goodwin, G., Graebe, S., & Salgado, M. (2000). *Control System Design.* New Jersey: Prentice Hall.

Hassoun, N., & Al-Manaseer, A. (2005). *Structural Concrete: Theory and Design.* New Jersey: Wiley.

Hjelmstad, K. D., & Haikal, G. (2006). Analysis of Steel Moment Frames with Deformable Panel Zones. *Steel Structures*, 129-140.

Horiuchi, T., & Konno, T. (2001). A New Method for Compensating Actuator Delay in Real-Time Hybrid Experiments. *Philosophical Transaction of the Royal Society: Theme Issue on Dynamic Testing of Structures, A359*, 1893-1909.

Horiuchi, T., Inoue, M., Konno, T., & Namita, Y. (1999). Real-Time Hybrid Experimental System with Actuator Delay Compensation and its Application to a Piping System with Energy Absorber. *Earthquake Engineering and Structural Dynamics, 28*(10), 1121-1141.

Huang, H. M., Gao, X., Tidwell, T., Gill, C., Lu, C., & Dyke, S. (2010). Cyber-Physical Systems for Real-Time Hybrid Structural Testing: A Case Study. *ACM/IEEE International Conference on Cyber-Physical Systems (ICCPS'10).*

Ikhouane, F., & Rodellar, J. (2007). *Systems with Hysteresis: Analysis, Identification and Control Using the Bouc-Wen Model.* Wiley-Interscience.

Ioannou, P., & Sun, J. (1996). *Robust Adaptive Control.* New Jersey: Prentice Hall.

Jansen, L. M., & Dyke, S. J. (2000). Semi-Active Control Strategies for the MR Damper: A Comparative Study. *Journal of Engineering Mechanics, 126*(8), 795–803.

Juang, J. N. (1994). *Applied System Identification.* New Jersey: Prentice Hall.

Juang, J. N., & Pappa, R. S. (1985). An Eigensystem Realization Algorithm for Modal Parameter Identification and Model Reduction. *Journal of Guidance, Control, and Dynamics, 8*, 620-627.

Jung, R. Y., & Shing, P. B. (2006). Performance Evaluation of a Real-Time Pseudodynamic Test System. *Earthquake Engineering and Structural Dynamics, 35*(7), 789-810.

Kwon, O., Elnashai, A. S., Spencer, B. F., & Park, K. (2007). UI-SIMCOR: A Global Platform for Hybrid Distributed Simulation. *Ninth Canadian Conference on Earthquake Engineering.* Ottawa, Ontario, Canada.

Landau, Y. (1979). *Adaptive Control: the Model Reference Approach.* New York: Dekker.

Li, G., Stoten, D. P., & Tu, J.-Y. (2010). Model Predictive Control of Dynamically Substructured Systems with Application to a Servohydraulically-Actuated Mechanical Plant. *IET Control Theory & Applications, 4*, 253-264.

Lim, C. N., Neild, S. A., Stoten, D. P., Drury, D., & Taylor, C. A. (2007). Adaptive Control Strategy for Dynamic Substructuring Tests. *Journal of Engineering Mechanics, 113*(8), 864-873.

Magonette, G. (2001). Development and Application of Large-scale Continuous Pseudodynamic Testing Techniques. *Philosophical Transactions of Royal Society, 359*, 1771-1799.

McFarlane, D., & Glover, K. (1990). *Robust Controller Design Using Normalized Coprime Factor Plant Descriptions – Lecture Notes in Control and Information Sciences.* Berlin: Springer-Verlag.

McFarlane, D., & Glover, K. (1992). A Loop Shaping Design Procedure Using H∞ Synthesis. *IEEE Transactions on Automatic Control, 37*(6), 759-769.

Mercan, O. (2007). *Analytical and Experimental Studies on Large Scale, Real-time Pseudodynamic Testing.* Bethlaham, PA: Dept. of Civil and Environmental Engineering, Lehigh Univeristy.

Merritt, H. E. (1967). *Hydraulic Control Systems.* New York: Wiley.

Nakashima, M., & Masaoka, N. (1999). Real-Time Online Test for MDOF Systems. *Earthquake Engineering and Structural Dynamics, 28*(4), 393-420.

Narendra, K., & Annaswamy, A. (1989). *Stable Adaptive Systems.* New Jersey: Prentice Hall.

National Instruments. (2011). NI Product Manuals. Austin, TX, USA.

Newmark, N. M. (1959). A Method of Computation for Structural Dynamics. *Journal of Engineering Mechanics Division, 85*, 67–94.

Ohtori, Y., Christenson, R. E., Spencer, B. F., & Dyke, S. J. (2004). Nonlinear Benchmark Control Problem for Seismically Excited Buildings. *Journal of Engineering Mechanics, 130*(4), 366-385.

Phillips, B. M., & Spencer, B. F. (2011). *Model-based Servo-hydraulic Control for Real-time Hybrid Simulation.* Urbana, IL: Newmark Structural Engineering Laboratory Report Series, University of Illinois at Urbana-Champaign.

Phillips, B. M., & Spencer, B. F. (submitted). Model-Based Multi-Actuator Control for Real-time Hybrid Simulation. *Journal of Engineering Mechanics*.

Reinhorn, A., Sivaselvan, M., Liang, Z., & Shao, X. (2004). Real-time Dynamic Hybrid Testing of Structural Systems. *13th World Conference on Earthquake Engineering.* Vancouver, B.C., Canada.

Shing, P. B., & Mahin, S. A. (1987). Cumulative Experimental Errors in Pseudodynamic Tests. *Earthquake Engineering and Structural Dynamics, 15*, 409–424.

Shing, P., Wei, Z., Jung, R., & Stauffer, E. (2004). NEES Fast Hybrid Test System at The University of Colorado. *13th World Conference on Earthquake Engineering.* Vancouver, B.C., Canada.

Shore Western Manufacturing. (2011). SC6000 Hardware Configuration Manual. Monrovia, CA, USA.

Slotine, J., & Li, W. (1991). *Applied Nonlinear Control.* New Jersey: Prentice Hall.

Speedgoat GmbH. (2011). Speedgoat Hardware Manual. Liebefeld, Switzerland.

Spencer, B. F., Dyke, S. J., Sain, M. K., & Carson, J. D. (1997). Phenomenological model for magnetorheological dampers. *Journal of Engineering Mechanics, 123*(3), 230-238.

Stoten, D. P., & Benchoubane, H. (1993). The Minimal Control Synthesis Identification Algorithm. *International Journal of Control, 58*(3), 685-696.

Takahashi, Y., & Fenves, G. L. (2006). Software Framework for Distributed Experimental-Computational Simulation of Structural Systems. *Earthquake Engineering and Structural Dynamics, 35*, 267-291.

The Mathworks Inc. (2011a). MATLAB User's Guide. Natick, MA, USA.

Vidyasagar, M. (1988). Normalized Coprime Factorizations for Non-Strictly Proper Systems. *IEEE Transactions on Automatic Control, 33*(3), 300-301.

Wang, Q. (2007). *Real-time Substructure Testing Method and its Application (In Chinese).* Harbin, China: Harbin Institute of Technology.

Wei, Z. (2005). *Fast Hybrid Test System for Substructure Evaluation. Ph.D. dissertation.* Boulder, CO: Dept. of Civil, Environmental and Architectural Engineering, Univ. of Colorado Boulder.

Wu, B., Wang, Q., Shing, P. B., & Ou, J. (2007). Equivalent Force Control Method for Generalized Real-time Substructure Testing. *Earthquake Engineering and Structural Dynamics, 36*, 1127-1149.

Yang, G., Spencer, B. F., Jung, H., & Carlson, D. J. (2004). Dynamic Modeling of Large-Scale Magnetorheological Damper Systems for Civil Engineering Applications. *Journal of Engineering Mechanics, 130*(9), 1107-1114.

Yao, B., Bu, F., & Chiu, G. T. (2001). Nonlinear Adaptive Robust Control of Electro-hydraulic Systems Driven by Double-rod Actuators. *International Journal of Control, 74*(8), 761-775.

Yi, F., Dyke, S. J., Caicedo, J. M., & Carlson, J. (2001). Experimental Verification of Multi-Input Seismic Control Strategies for Smart Dampers. *Journal of Engineering Mechanics, 127*(11), 1152-1164.

Yoshida, O., Dyke, S. J., Giacosa, L. M., & Truman, K. Z. (2003). Experimental Verification of Torsional Response Control of Asymmetric Buildings Using MR Dampers. *Earthquake Engineering & Structural Dynamics, 32*(13), 2085–2105.

Zhang, Y., Sim, S., & Spencer, B. F. (2008). Finite Element Model Updating of a Truss Model Using Incomplete Modal Data. *Proc. World Forum on Smart Materials and Smart Structures Technology.*

Zhao, J. (2003). *Development of EFT for Nonlinear SDOF Systems, Ph.D. Dissertation.* Minnesota, MN: University of Minnesota.

Zhou, K., & Doyle, J. (1998). *Essentials of Robust Control.* New Jersey: Prentice Hall.

VITA

VITA

Xiuyu Gao received his B.E. in Civil Engineering from Tongji University in China and his M.Sc. in Computational Mechanics from Technical University of Munich in Germany. He receives his Ph.D. degree in Structural Engineering from Purdue University.